Final Report

Development of a Failure Theory for Concrete

Contract Number BDK83 977-02

FSU Project ID: 025141 / 025142

Submitted to:

Florida Department of Transportation
Research Center
605 Suwannee Street
Tallahassee, Florida 32399-0450

William A. Potter, P.E.
Project Manager
FDOT Structures Design Office

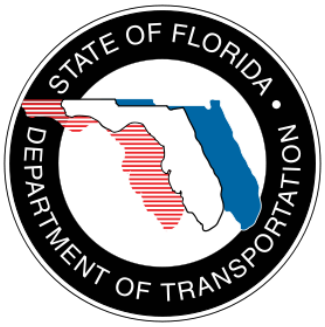

Prepared by:

Raphael Kampmann
Graduate Research Assistant
Michelle Rambo-Roddenberry, Ph.D., P.E.
Principal Investigator
Wei-Chou Virgil Ping, Ph.D., P.E.
Co-Principal Investigator

FAMU-FSU College of Engineering
Department of Civil and Environmental Engineering
2525 Pottsdamer Street
Tallahassee, FL 32310

August–2012

DISCLAIMER

The opinions, findings, and conclusions expressed in this publication are those of the authors, who are responsible for the facts and accuracy of the data presented herein. The contents do not necessarily reflect the views or policies of the Florida Department of Transportation or the Research and Special Programs Administration. This report does not constitute a standard, specification, or regulation.

The report is prepared in cooperation with the State of Florida Department of Transportation and the U.S. Department of Transportation.

Approximate conversion to SI units

Symbol	When you know	Multiply by	To find	Symbol
		Length		
in.	inches	25.4	millimeters	mm
ft	feet	0.305	meters	m
yd	yards	0.914	meters	m
mi	miles	1.61	kilometers	km
		Area		
in^2	square inches	645.2	square millimeters	mm^2
ft^2	square feet	0.093	square meters	m^2
yd^2	square yard	0.836	square meters	m^2
ac	acres	0.405	hectares	ha
mi^2	square miles	2.59	square kilometers	km^2
		Volume		
fl oz	fluid ounces	29.57	milliliters	mL
gal	gallons	3.785	liters	L
ft^3	cubic feet	0.028	cubic meters	m^3
yd^3	cubic yards	0.765	cubic meters	m^3
		Mass		
oz	ounces	28.35	grams	g
lb	pounds	0.454	kilograms	kg
T	short tons (2000 lb)	0.907	megagrams	Mg
		Temperature		
°F	Fahrenheit	$\frac{5}{9}(F - 32)$	Celsius	°C
		Illumination		
fc	foot-candles	10.76	lux	lx
fl	foot-Lamberts	3.426	$\frac{candela}{m^2}$	$\frac{cd}{m^2}$
		Stress/Pressure		
lbf	poundforce	4.45	newtons	N
$\frac{lbf}{in^2}$ (or psi)	$\frac{poundforce}{square\ inch}$	6.89	kilopascals	kPa

Approximate conversion to imperial units

Symbol	When you know	Multiply by	To find	Symbol
		Length		
mm	millimeters	0.039	inches	in.
m	meters	3.28	feet	ft
m	meters	1.09	yards	yd
km	kilometers	0.621	miles	mi
		Area		
mm^2	square millimeters	0.0016	square inches	in^2
m^2	square meters	10.764	square feet	ft^2
m^2	square meters	1.195	square yards	yd^2
ha	hectares	2.47	acres	ac
km^2	square kilometers	0.386	square miles	mi^2
		Volume		
mL	milliliters	0.034	fluid ounces	fl oz
L	liters	0.264	gallons	gal
m^3	cubic meters	35.314	cubic feet	ft^3
m^3	cubic meters	1.307	cubic yards	yd^3
		Mass		
g	grams	0.035	ounces	oz
kg	kilograms	2.202	pounds	lb
Mg	megagrams	1.103	short tons (2000 lb)	T
		Temperature		
°C	Celsius	$\frac{9}{5}C + 32$	Fahrenheit	°F
		Illumination		
lx	lux	0.0929	foot-candles	fc
$\frac{cd}{m^2}$	$\frac{\text{candela}}{\text{m}^2}$	0.2919	foot-Lamberts	fl
		Stress/Pressure		
N	newtons	0.225	poundforce	lbf
kPa	kilopascals	0.145	$\frac{\text{poundforce}}{\text{square inch}}$	$\frac{\text{lbf}}{\text{in}^2}$ (or psi)

Technical Report Documentation Page

1. Report No.	2. Government Accession No.	3. Recipient's Catalog No.
BDK83 977-02		

4. Title and Subtitle	5. Report Date
Development of a Failure Theory for Concrete	8/31/2012
	6. Performing Organization Code

7. Author(s)	8. Performing Organization Report No.
Raphael Kampmann Michelle Roddenberry, Ph.D., P.E. Wei-Chou Virgil Ping, Ph.D., P.E.	

9. Performing Organization Name and Address	10. Work Unit No. (TRAIS)
FAMU-FSU College of Engineering 2525 Pottsdamer Street Tallahassee, FL 32310	11. Contract or Grant No.

12. Sponsoring Agency Name and Address	13. Type of Report and Period Covered
Florida Department of Transportation Research Center 605 Suwannee Street Tallahassee, Florida 32399-0450	Final Report 09/22/2008 – 08/31/2012
	14. Sponsoring Agency Code

15. Supplementary Notes

16. Abstract

The failure behavior of concrete materials is not completely understood because conventional test methods fail to assess the material response independent of the sample size and shape.
To study the influence of strength affecting test conditions, four typical concrete sample types were experimentally evaluated in uniaxial compression and analyzed for strength, crack initiation/propagation, and fracture patterns under varying boundary conditions. Both low friction and conventional compression interfaces were assessed. High-speed video technology was used to monitor macrocracking.

Inferential data analysis proved reliably lower strength results for reduced surface friction at the compression interfaces, regardless of sample shape. Reciprocal comparisons revealed statistically significant strength differences between most sample shapes. Crack initiation and propagation was found to differ for dissimilar compression interfaces.

The principal stress and strain distributions were analyzed, and the strain domain was found to resemble the experimental results, whereas the stress analysis failed to explain failure for reduced end confinement. Neither stresses nor strains indicated strength reductions due to reduced friction, and therefore, buckling was considered. The high-speed video analysis revealed buckling phenomena, regardless of end confinement. Slender elements were the result of low friction, and stocky fragments developed under conventional confinement. The critical buckling load increased accordingly.

The research showed that current test methods do not reflect the ``true'' compressive strength and that concrete failure is strain driven. Ultimate collapse results from buckling preceded by unstable cracking.

17. Key Word	18. Distribution Statement
concrete; failure; crack; test; fracture; high-speed video; compression	

19. Security Classif. (of this report)	20. Security Classif. (of this page)	21. No. of Pages	22. Price
U	U	178	

ACKNOWLEDGEMENTS

The authors would like to thank the Florida Department of Transportation (FDOT) for providing the funding for this research. In particular, Sam Fallaha, William A. Potter, David J. Wagner, and Stephen Eudy provided helpful comments and valuable discussions throughout the project. The staff at the FDOT Structures Research Center was very supportive and contributed to the success of this research.

This research was inspired by Marcus H. Ansley, P.E.; his visions and initial guidance were an encouraging contribution. This project would not have been possible without the dedicated engineer, who passed away in 2010, one year into the project. He left behind many great ideas for others to explore. His passion and enthusiasm inspired the people around him, and he laid the foundation for future research. It remains questionable if this paper does justice to his inspirations. The authors are grateful to Marc for sharing his visions, ideas, and interests, though he is missed for so much more.

EXECUTIVE SUMMARY

The failure behavior of concrete materials is not completely understood because conventional test methods fail to assess the material response independent of the sample size and shape. The specimen geometry, the size of contact surface, and the coefficient of friction at the compression interface are assumed to affect the strength measurements for concrete materials.

To analyze the strength performance, crack initiation, crack propagation, and fracture patterns of concrete in uniaxial compression, an experimental program was developed to study four typical specimen types under varying boundary conditions. Cylindrical specimens with a height-to-diameter ratio of 2 and prismatic samples with square cross sections and height-to-depth ratios of 1 and 2 were tested to evaluate the influence of sample shape. The effect of end confinement was assessed by using different bearing plates. Control group specimens were tested with conventional compression plates, and low friction materials were applied at the compression interface to assess test group samples. The ultimate strength and final fracture patterns were evaluated according to ASTM C 39, while high-speed video technology with 2,000 frames per second (fps) was utilized to monitor crack initiation and crack propagation.

Inferential data analysis with a 4×2 factorial Analysis of Variance (ANOVA) proved reliably lower "ultimate" strength results due to reduced surface friction at the compression interfaces, regardless of sample shape. The intensity of strength reduction, however, was found to differ for each shape. A reciprocal comparison revealed statistically significant strength differences (shape effect) between 5 out of 6 plausible shape combinations — irrespective of surface friction. Strain measurements at mid-height of 6 in. × 12 in. (152 mm × 305 mm) cylinders under increasing and sustained loading showed that the elastic behavior (modulus of elasticity) within the central zone of the specimen is unaf-

fected by the compression interface. Similarly, the onset of stable and unstable cracking appeared to be identical for the two dissimilar surface treatments. Independent of the evaluated sample types, clear differences in crack initiation and crack propagation were observed for different boundary conditions. While conventionally tested specimens initiated cracking from the middle, cracks started to grow from the specimen extremes under reduced surface friction. High surface friction produced Type 1 or Type 2 rupture because higher end confinement restrained the specimens from cracking through the contact surfaces. Reduced friction at the bearing plates caused failure cracks parallel to the applied compression (Type 3), which extended through the complete length of the specimens as a result of unimpeded lateral tensile strains.

The experimental concrete behavior was analyzed according to the principles of continuum mechanics to reflect the three-dimensional principal stress and strain distribution under varying boundary conditions. While the stress analysis was in good agreement with the observed crack orientations, it failed to explain rupture stresses for unconfined uniaxial testing. Accounting for the effects of Poisson's ratio, the strain analysis properly reflected failure under reduced friction, but neither stress nor strain analyses were indicative of strength reduction due to lower surface friction, and the concept of buckling phenomena was considered. Because the internal structural rearrangement of the test specimens was affected by changing boundary conditions, different columnar elements were formed throughout the unstable cracking phase. While slender elements were the result of a low friction compression interface, stocky fragments developed in conventionally tested specimens. Local buckling phenomena were clearly documented by the high-speed video analysis and facilitated explaining the effect of strength reduction, since critical buckling loads decrease as slenderness increases.

It was concluded that current test methods are not reflective of the "true" uniaxial compressive strength and that the specimen response between conventional compression plates differs from the material behavior in concrete structures, as the strength measurement is shape-dependent and affected by the compression interface. Furthermore, this research shows that concrete failure is strain driven and that the stress domain does not suffice to explain cracking. Regardless of end confinement and sample shape, ultimate collapse

of concrete resulted from localized buckling of concrete fragments that were formed throughout the unstable cracking phase.

TABLE OF CONTENTS

LIST OF TABLES

LIST OF FIGURES

GLOSSARY

Analysis of Variance		statistical method to analyze numerical data in mutual dependence of multiple variables.
brush platen		a comb-like steel plate that is used in bi-axial and triaxial compression testing to reduce the end confinement at the compression interface.
capping compound		granulate materials that are melted and formed over the ends of test specimens to provide a smooth, level surface. Usually melted at temperatures above 240 °F (115 °C).
cement		(Portland cement) is a binder that sets and hardens chemically when mixed with water. It is made of limestone and small quantities of other materials (clay, gypsum, etc.). It is the only binding material in concrete.
coefficient of friction	μ	dimensionless scalar that describes the frictional force component (parallel to the friction surface) as a percentage of the force that compresses two interacting materials (perpendicular to the friction surface). It depends on the surface properties of the two contacting materials.

coefficient of variation	CV	normalized variability of data spread of a probability distribution. It is defined by the quotient of the population standard deviation and the population mean.
compression interface		contact layer between the compression bearing plates and the actual test specimen.
concrete		composite construction material mainly consisting of aggregates, cement (binder), and water. In its fresh state, it can be molded into any shape but takes on rock-like properties after hardening (due to hydration).
confidence interval		uncertainty corresponding to a sampling method. It defines the probability associated with a randomly drawn sample from a specified population.
curing		process to guarantee a moist concrete surface throughout the early period (usually 7 days) of concrete hardening for proper hydration processes and reduced cracking. Concrete can be cured through soaking, sprinklers, covering with wet burlap, or by coating with commercially available curing compounds.
direction angle	α	represents the angle a vector forms with one of the axes of the reference frame (also directional cosine).
eigenspace		vector space that is described by the eigenvectors (mutually perpendicular) of a square matrix.

eigenvalue	λ	property of a square matrix corresponding to an eigenvector. It is the factor by which the eigenvector is scaled when multiplied by its square matrix.
eigenvector	$\vec{n}_\Omega$	non-zero vector corresponding to a square matrix that, after being multiplied by the matrix, remains parallel to the original vector.
high-performance concrete		exceeds the properties and constructability of normal concrete. Special mixing, placing, and curing practices are required to produce and handle high-performance concrete. It features high compressive strengths, high early-strengths, high moduli of elasticity.
high-speed video		motion pictures with high frame rates.
high-strength concrete		Although there is no precise point of separation between high-strength concrete and normal-strength concrete, the American Concrete Institute (ACI) defines high-strength concrete as concrete with a compressive strength greater than 6000 psi (41 MPa).
high-strength lightweight concrete		Similar to high-strength concrete, but produced with light-weight aggregates
hydrostatic pressure	P	the omni-directional pressure developed by a fluid due to gravity.
interfacial transition zone	ITZ	Cement paste region that surounds the aggregates, marking the transition between the cement matrix and the granular particles.

light-emitting diode		semiconductor light source.
load cell		sensor that measures the force acting upon it.
linear variable differential transducer		electromagnetic displacement sensor that converts the rectilinear motion of its core into a corresponding voltage signal. Used for deformational measurements.
macrocrack		large-scale crack that is visible to the naked eye.
main effect		impact of a factor on a dependent variable, averaged across the levels of other factors.
microcrack		concrete cracks that are not visible to the naked eye. Develop in concrete without the application of external stresses as a result of temperature effects or relaxation at the matrix-aggregate interface.
modulus of elasticity		material property defining the stress-strain relationship of solids. It predicts the deformation of a body due to the stress acting upon it.
mortar		(also Portland cement mortar) workable paste made of cement, water, and fine aggregates that hardens due to hydration process of cement to develop a rock-like structure.
normal stress	$\sigma_\perp$	stress component that acts perfectly perpendicular to a reference unit area.

normal-strength concrete		concrete mixture with standard strength properties, ranging between 2,000 and 8,000 psi.
null hypothesis	H_0	theory that is believed to be true and can statistically be proven. If found to be true, the hypothesis has to be accepted, but must be rejected if it cannot statistically be proven.
octahedral normal stress	σ_{oct}	component of the stress tensor that acts normal to the deviatoric plane, or along the hydrostatic axis. Its value is equal to the mean stress, σ_m, or one third of the first stress invariance.
octahedral shear stress	τ_{oct}	component of the stress tensor that acts parallel to the deviatoric plane, or perpendicular to the hydrostatic axis.
paste		(also cement paste) matrix material that provides the strength developing properties for concrete and mortar. It is the product of cement powder combined with water.
Poisson's ratio	ν	named after Siméon Poisson, describes the relation between two perpendicular strain measures in solid materials. It is described by the quotient of lateral and axial deformation of an axially strained body.
post-hoc analysis		data analysis that occurs after an experiment has been concluded and the main (first level) results have been determined. It analyzes data patterns of subgroups.

principal direction		stress component directed along/parallel to the principal stress, i.e., perpendicular to the principal planes.
principal stress	$\sigma_{1,2,3}$	occurs on planes (principal planes) that do not experience shear stresses, i.e., planes under pure normal stress.
Rockwell hardness		named after Hugh M. Rockwell, describes the hardness of a material. It is determined through the comparison of two penetration depths of an indenter under a preload and a larger test load. Harder materials typically obtain higher values.
shear stress	$\sigma_{\|\|}$	stress component that acts perfectly parallel to a reference unit area.
significant difference		statistically relevant difference that did not occur randomly and is not due to chance.
slenderness		relationship of specimen height to its cross-sectional area.
standard deviation	μ	statistical property providing information about the dispersion of a data set. It defines the average distance from the data mean and is expressed in the same unit as the data itself.
strain	ϵ	deformation measurement that represents the relative displacement of two particles with respect to their original distance. Although normalized or unitless, it is commonly reported in microstrain (μstrain or 10^{-6}) to avoid small numbers.

strain gauge		a sensor used to measure the strain response of a body. It is attached to the body by a suitable adhesive and deforms as the body deforms. Changes in the electrical resistance of a strained foil gauge can be measured and related to the deformation of the body.
strain tensor	ϵ_{ij}	mathematical expression for the (three-dimensional) strain state of an infinitesimally small material point. It preserves the physical properties of strain, independent of the chosen reference frame.
stress	σ	derived measurement, defining the average force per unit area on a surface/body.
stress tensor	σ_{ij}	mathematical expression for the (three-dimensional) stress state of an infinitesimally small material point. It preserves the physical properties of stress, independent of the chosen reference frame.
Student's t-test		statistical method to analyze the mean differences of two populations while considering the data distribution of individual samples. It determines statistical significance of the populations' differences.
Teflon		(polytetrafluoroethylene (PTFE)) solid material used as low friction dry lubricant. With a coefficient of friction ranging between 0.05 and 0.10, it provides the third-lowest frictional resistance of any known solid.

tensile stress	σ_t	stress phenomenon that elongates a body or puts a physical object into tension.
tensor	A_{ij}	mathematical expression for an object that is bound to geometrical constraints within the dimensions it exists in. A tensor is a multidimensional array of scalar components. The indices required to determine the array dimension determine the order of the tensor.
torsion	t	(torque) mechanical process to twist an object about its own axis.
traction vector	$\vec{t}$	completely describes the three dimensional stress situation over an infinitesimal point-plane (also stress vector).
type 1 error		occurs when rejecting the null hypothesis, although it is in fact true. The significance level, α, of a test hypothesis is the probability for a type 1 error.
ultra high-strength concrete		composed of an optimized gradation of granular constituents, a water-to-cementitious materials ratio less than 0.25, and a high percentage of discontinuous internal fiber reinforcement. Its compressive strength is greater than 21.7 ksi (150 MPa) while sustaining post-cracking tensile stresses are greater than 0.72 ksi (5 MPa).

ultra high-performance concrete		very high-strength concrete mixture consisting of fine sand (no coarse aggregates), cement, silica fume, and quartz flour. Compressive strengths range between 18,000 and 30,000 psi (124 to 207 MPa).
unit vector	$\vec{n}_\Omega$	vector with unit length normally used to describe an orientation.

ACRONYMS

vi	virtual instrument
ACI	American Concrete Institute
ANOVA	Analysis of Variance
c-c	compression-compression
c-c-c	triaxial compression
c-t	compression-tension
COF	coefficient of friction
FDOT	Florida Department of Transportation
FIB	Florida I-Beam
fps	frames per second
HPC	high-performance concrete
HSC	high-strength concrete
HSLWC	high-strength lightweight concrete
ITZ	interfacial transition zone
kip	kilo punds
ksi	kilo punds per square inch

LED	light-emitting diode
LVDT	linear variable differential transducer
MOE	modulus of elasticity
MRAC	modeled recycled aggregate concrete
NSC	normal-strength concrete
pcf	pounds per cubic foot
PTFE	polytetrafluoroethylene
RAC	recycled aggregate concrete
t-t	tension-tension
UHPC	ultra high-performance concrete
UHSC	ultra high-strength concrete

CHAPTER 1

INTRODUCTION

1.1 Introduction

The uniaxial compressive strength of concrete is considered a crucial material property and, as such, of noticeable importance for the design of concrete structures according to current building codes (American Concrete Institute, 2011a). Many mechanical properties and parameters of concrete have been related to the compressive strength via empirical formulas (Neville, 1996; Popovics, 1998; Torrenti et al., 2010) to facilitate design procedures and calculations. Nevertheless, the concrete strength measured by ASTM C 39 (ASTM-International, 2004b) and the design strength according to ACI 214 (American Concrete Institute, 2011b) differ from the ultimate material strength in structural components because certain failure phenomena are not fully understood (Bazant, 2000; van Mier and Man, 2009) and, therefore, are not considered. In uniaxial compression testing, larger specimens usually yield lower strength results (Burtscher and Koilegger, 2003; Turkel and Ozkul, 2010), and the precision of strength measurement is closely related to the evaluated specimen type and size (Burtscher and Koilegger, 2003; Chin et al., 1997; del

Viso et al., 2008; Hake, 2004; Indelicato and Paggi, 2008; Taghaddos et al., 2010; Yazici and Sezera, 2007). Many attempts have been made to establish a single relation between different sample types, but no such single relation is known (Hughes and Bahramian, 1965). In general, it is believed that "the strength of a structure can only be determined by testing of the structure itself" (Burtscher and Koilegger, 2003) because global structural mechanisms and the rearrangement of failure paths throughout the loading stages contribute to final collapse. In particular cases, however, it is difficult to trace the global failure back to the material level. Specifically, the so-called shear failure of prestressed girders with high confinement reinforcement at the end region is a result of the sudden disintegration of the compression struts (Hamilton et al., 2009). The load path and the direction of principal tensile stresses/strains of such shear tests are illustrated in Figure 1.1. Because the principal stresses

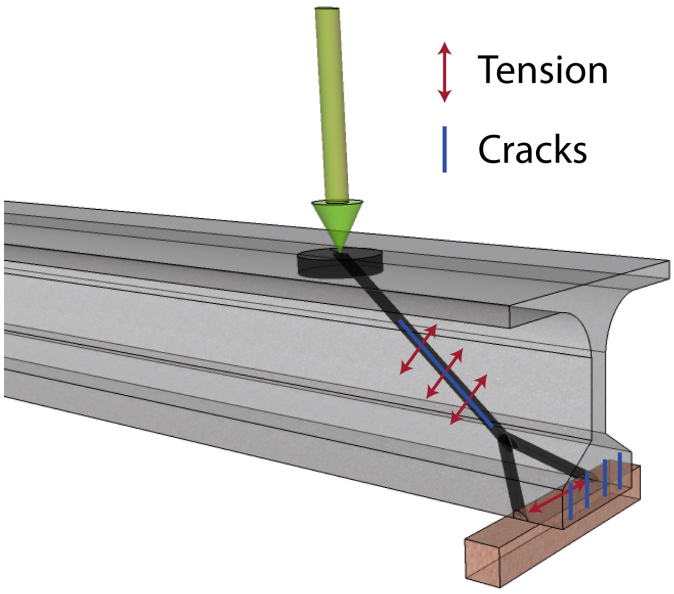

Figure 1.1: Tensile and crack distribution in structural element

are believed to superimpose the principal strains, it is generally assumed that the failure-initiating web cracks, as seen in Figure 1.2, are a consequence of

Figure 1.2: Concrete failure in structural testing

principal tensile stresses. While such theory seems reasonable in shear testing, it fails to explain the failure phenomenon of structural members with high compressive stresses along their longitudinal axis. An example is the anchorage zone of post-tensioned members as shown in Figure 1.3. Although stresses are purely longitudinal, failure cracks occur parallel to the applied compressive stress and are assumed to be a consequence of the so-called bursting stresses (Tawfiq and Robinson, 2008). The local fracture process of the described structural elements at collapse is indicative of the true fracture and failure behavior of concrete materials, but this is not properly reflected by uniaxial

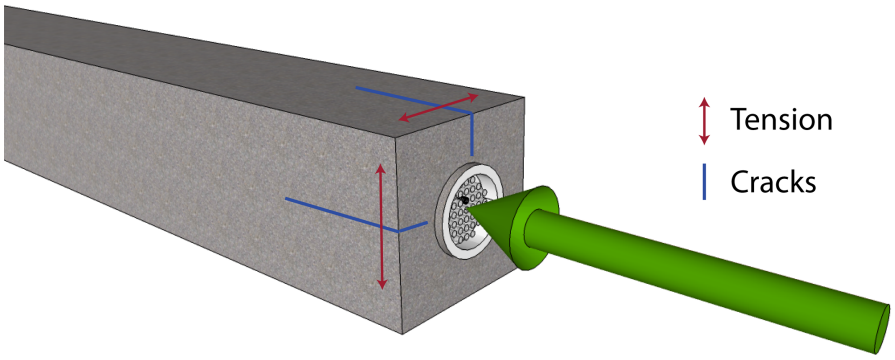

Figure 1.3: Tensile and crack distribution in post-tensioned element

sample testing according to ASTM C 39 (ASTM-International, 2004b) — regardless of sample shape and/or size. "Both the form of failure and the lateral strain measurements of test specimens [...] indicate that friction between the steel loading platen and the concrete restrains the end of the test specimen" (Hughes and Bahramian, 1965).

1.2 Problem Statement

The behavior of concrete on the material level is not completely understood because the conventional test method according to ASTM C 39 (ASTM-International, 2004b) fails to assess the material behavior independent of the sample size and shape. Structural effects during sample testing differ depending on the specimen geometry, the size of contact surface, and the magnitude of surface friction at the compression interface; accordingly, those factors affect the failure behavior of concrete specimens. To assess the true compressive strength of concrete, and to study the natural crack propagation within con-

crete materials, the conventional test method has to be modified to eliminate (or at least reduce) structural effects. It has been suggested that the reduction of end confinement at the specimen extremes eliminates the shape effect (Tschegg et al., 1994), which would indicate a failure mechanism due to lateral dilation. Herein it seems reasonable to assume that the collapse of concrete is a consequence of unimpeded tensile strains (direct or indirect) on the material level, and that a stress-based failure criterion is insufficient to describe failure — a strain criterion appears more suitable.

1.3 Research Objective

The primary objective of this research is to assess the concrete behavior at failure. Specifically, crack initiation, crack propagation, and fracture patterns are the main focus. This study aims to experimentally evaluate the different failure aspects of concrete in uniaxial compression and strives to analyze the corresponding mechanism that leads to final fracture. The research is targeted at typical specimen types to study the effect of dissimilar concrete shapes and specimen sizes. Furthermore, the influence of end confinement is assessed to improve the understanding of concrete failure on the material level. The final objective is to formulate a general failure theory for concrete that is equally applicable on the material and structural scales.

1.4 Research Scope

To assess the failure behavior of concrete under compression, this study encompassed an experimental and analytical evaluation of standard concrete

specimens. Four typical sample types were tested in uniaxial compression under the influence of varying boundary conditions. Cylindrical specimens with a height-to-diameter ratio of 2 and prismatic samples with squared cross sections and height-to-depth ratios of 1 and 2 were tested to evaluate the influence of shape and size on the different failure aspects. To analyze the effect of varying boundary conditions, all tests were carried out with two different bearing plate arrangements. While conventional bearing plates provided the control baseline, a compression interface with a reduced coefficient of friction (COF) was used to study the influence of end confinement at the specimen extremes. The ultimate strength and final fracture patterns were evaluated according to ASTM C 39 (ASTM-International, 2004b), while crack initiation and crack propagation were assessed through high-speed video technology with 2,000 frames per second (fps). The experimentally documented concrete behavior is analytically reflected by analysis of stress and strain according to the principles of continuum mechanics.

1.5 Chapter Overview

The remaining six chapters describe conducted research as follows. A comprehensive overview of the study at hand is given in Chapter 1. The general introduction is followed by the problem statement, leading to the research objectives and the scope of this evaluation. Chapter 2 addresses the theoretical background and offers an overview of the research related literature. The methodology and the fundamental approach to address the problem statement are detailed in Chapter 3, along with the utilized materials, the required test procedures, and the deployed equipment. The test results according to the

different failure aspects of concrete are presented in Chapter 4. Chapter 5 explains the test results analytically and according to the theories of continuum mechanics. Specifically, the principal stress and strain states are reviewed to evaluate the cracking behavior of concrete for varying boundary conditions. Furthermore, the concept of buckling phenomena is discussed. Failure aspects are reviewed in Chapter 6 and individually compared to the findings and conclusions drawn by other researchers. After all failure characteristics are discussed separately, the sequential failure mechanism of concrete in compression is reviewed to relate the experimental and analytical findings on the material level to the failure behavior on the structural scale. Chapter 7 presents the final remarks and outlines the major conclusions before future research topics are proposed.

This text is supplemented by two appendices. Appendix A complements the analytical portion of Chapter 5 and details the developed computer codes that facilitated this study. The documented test results of Chapter 4 — specifically Section 4.6 – are substantiated by the multimedia content presented in Appendix B. In the electronic version of this document, this appendix provides selected full-length high-speed video recordings of collapsing concrete specimens.

CHAPTER 2

BACKGROUND

2.1 Introduction

To evaluate the failure behavior of concrete, this research focuses on two variables that are assumed to affect the strength performance of concrete. Specifically, the effects of the compression interface and the influence of the specimen shape were assessed (as detailed in Chapter 3). Other researchers have studied these aspects separately, but to the authors' knowledge, studies on the combined influence of the evaluated variables are limited or non-existing. Furthermore, the influence of boundary conditions appears mostly ignored in uniaxial compression testing while it is a major concern in biaxial or triaxial experiments. Nevertheless, the strength-affecting aspects and the fracture behavior of concrete have received significant attention since the establishment of modern concrete industries and have been scientifically investigated for over a century.

This chapter reviews the research related literature and presents the findings of other authors in chronological order. The chapter is sectioned according to the two variables analyzed in this research. Publications discussing the

influence of different compression interfaces are reviewed first. Afterwards, research articles on the topic of specimen shape and size are presented.

2.2 The Influence of Compression Interfaces

The restraining effects of surface friction became a significant issue throughout the development and advancement of biaxial and triaxial tests. Föppl (1899) demonstrated its importance, showing that the biaxial compression strength depends on the confinement at the loading surfaces. To eliminate confinement, a 75-to-25 stearin–tallow lubricant between the specimens and the bearing plates was applied, causing strength reduction that was attributed to non-uniform stress distribution. Numerous researchers followed such approach and employed different types of lubricants until Richart et al. (1928) exposed cylindrical concrete specimens to hydrostatic pressure in the radial direction (Figure 2.1), thereby eliminating load application through bearing plates, and

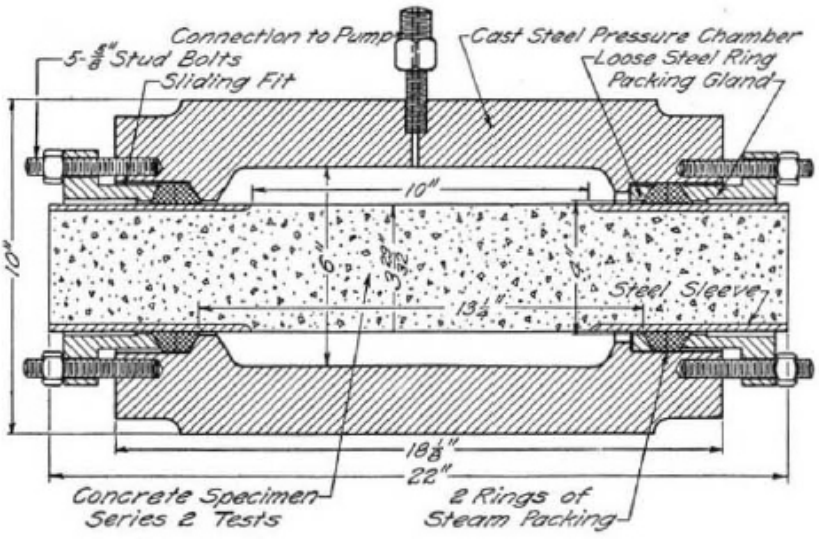

Figure 2.1: Hydraulic pressure chamber according to Richart et al. (1928)

thus avoiding surface friction. However, the shortcomings of such a test setup were understood, and the authors acknowledged that their conclusions were limited (Kupfer et al., 1969; Richart et al., 1928). Hollow cylinders followed, either subjected to internal hydraulic pressure (McHenry and Karni, 1958) or torsion (Bresler and Pister, 1958). Kupfer et al. (1969), recognizing the frictional drawbacks of those methods, replaced the solid bearing plates with brush platens (Figure 2.2) that were stiff enough to transmit the load, but sufficiently

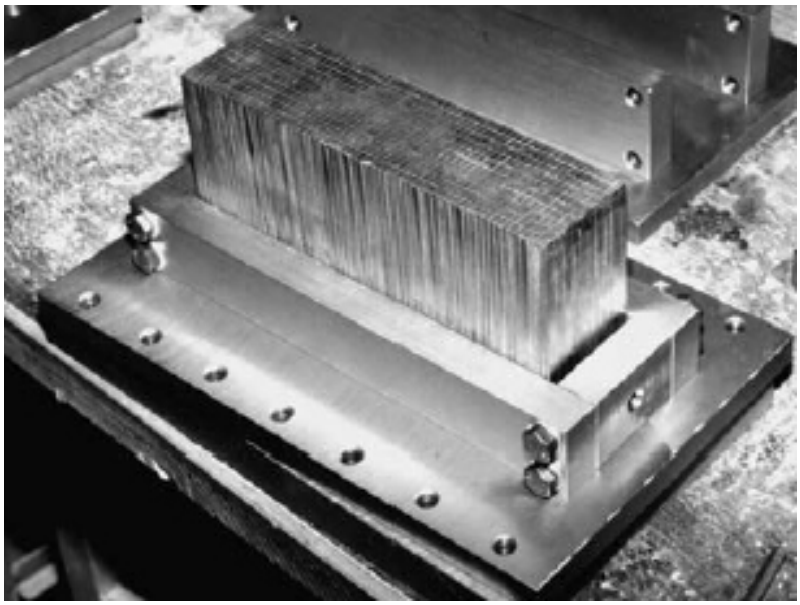

Figure 2.2: Brush Platens according to Kupfer et al. (1969) as replicated by Hampel (2006)

flexible to follow the concrete deformation and thus reduce the lateral restraint. It was proposed to use brush platens in tension tests, but such technique seems questionable due to the stiffening effect of filaments under increasing tensile loads. Nevertheless, the 7.9 in. × 7.9 in. × 2 in. (200 mm × 200 mm × 50 mm) concrete specimens revealed microcracks parallel to the applied uniaxial com-

pression (for normalization of biaxial test results) and failed with the formation of a major crack oriented at approximately 30° with respect to the line of action of the applied compressive load. Mills and Zimmerman (1970) used axle grease between 0.003 in. (0.076 mm) Teflon sheets or 0.004 in. (0.102 mm) polyethylene sheets. The tested 2.25-in. (57.2 mm) cubes cracked parallel to the uniaxial compression force, and it was concluded that surface friction must be eliminated for accurate compression tests. Rosenthal and Glucklich (1970) analyzed hollow concrete cylinders with a 12-in. (305 mm) outer diameter and a wall thickness of 0.98 in. (25 mm) by applying internal and external hydrostatic pressure in combination with axial loads that were applied by two cardboard layers of 0.2-in. (5 mm) thickness. The control cylinders, tested in uniaxial compression, failed by splitting cracks parallel to the applied load. Afterwards, an idealized 5 in. × 5 in. × 0.5 in. (127 mm × 127 mm × 12.7 mm) concrete model was developed by Buyukozturk et al. (1971) and tested in biaxial compression with bearing plates similar to those used by Kupfer et al. (1969). In the uniaxial case, ultimate failure occurred by splitting in planes perpendicular to the face of the specimen and parallel to the load as shown in Figure 2.3. Several others employed the comb-like plates and made similar observations (Atan and Slate, 1973; Tasuji et al., 1978).

In an attempt to formulate a general behavior theory for cement, pastes, mortar, and concretes, Taylor (1971) summarized previous research on the subject and found that most researchers agree; shear failure observed in traditional concrete compression tests is truly due to frictional restraint. It was proposed that the actual failure is a result of lateral tension. This was agreed upon by Tschegg et al. (1994), who understood that the difference in transverse strain (or Poisson's ratio) between the bearing plates and the concrete

Figure 2.3: Concrete model according to Buyukozturk et al. (1971) with vertical failure cracks after uniaxial compression test

specimen causes surface friction and lateral confinement. During the development of a biaxial fracture test for concrete, Tschegg et al. (1994) employed pressure-indicating film to evaluate the existing transverse strain correction techniques. It was found that brush platens cause a non-uniform stress distribution and increase shear stresses due to bending of the filaments under increased loads. With Teflon pads, however, the friction depended on the compressive stress only, i.e., not on lateral deformation. The best results and a uniform stress distribution were achieved by replacing the Teflon sliding layer with a 0.12-in. (3 mm) cardboard layer; furthermore, it was concluded that "the ideal correction would be realized by a device that completely follows the lateral deformation of the specimen during the application of compression and, in addition to this, also allows a homogeneous and constant force initiation in

the specimen".

Carino et al. (1994) investigated the significance of sulfur capping and grinding, using concrete mixtures with strength levels of 6500 psi (45 MPa) and 13 000 psi (90 MPa) and found that "no strength difference due to the method of end preparation was observed for the lower strength concrete, but for the higher strength concrete, grinding resulted in as much as 6 % greater measured strength" (Caldarone and Burg, 2009). While analyzing the performance of capping compounds for cylinder testing, Burg et al. (1999) found that the modulus of elasticity (MOE) decreased while the Poisson's ratio increased for high-strength capping compounds. It was determined that the apparent strength of high-strength concrete (HSC) tested with high-strength caps was lower than the same concrete mixtures tested with conventional strength caps.

Lee et al. (2004) repeated the tests done by Kupfer et al. (1969) for nuclear containment concrete but used Teflon instead of brush platens at the specimen-load frame interface. In compression tests, two Teflon pads were laid upon each other (sliding layer), and, in tension tests, the Teflon pads were glued to the concrete sample with epoxy adhesives. This, however, does not lower the friction but increases the restraint as it creates a rigid connection between the bearing plate and the specimen. Notwithstanding, in uniaxial compression the cracks were formed mostly parallel to the applied compression force (Figure 2.4), and the authors concluded that the failure modes using Teflon pads were satisfactory.

According to van Mier and Man (2009), the fracture process can be subdivided into four stages: elastic, microcracking, macrocrack growth (localization), and bridging. But concrete prisms tested in uniaxial compression experience localization only when care is taken that no frictional restraint

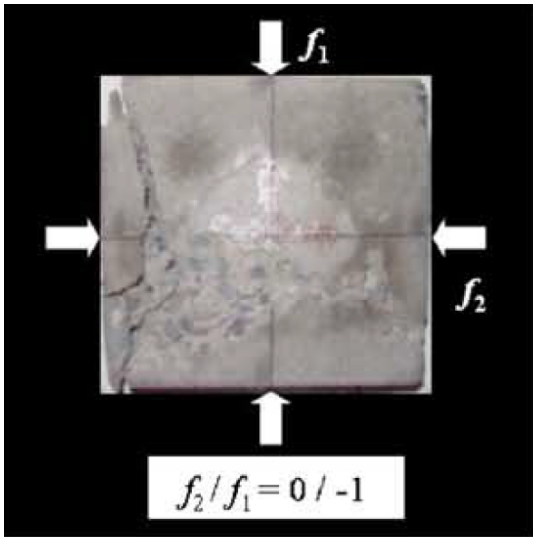

Figure 2.4: Uniaxial compression failure as reported by Lee et al. (2004)

between the loading platen and the specimen disturbs the stress field. The authors stated that it is difficult to simulate the mechanical and fracture behavior correctly, mostly because the frictional restraint cannot be included. Therefore, surface friction is the reason that macrocracks are inclined at 20° to 25° instead of being in line with the compression force.

Because concrete becomes more brittle as its nominal compressive strength increases, it also becomes more sensitive to testing related variables — a phenomenon studied by Caldarone and Burg (2009) while analyzing the importance of surface end preparation for testing HSC cylinders. Mostly based on reviewed literature, it was determined that the preparation of the compression contact surface is "one of the most important variables influencing the compressive strength results." In essence, it was shown that unbonded caps are only acceptable for normal-strength concrete (NSC), whereas suitable manufacturer prequalified bonded caps are required in higher strength regimes. However, ground surfaces were found to be satisfactory throughout all con-

crete strengths — including ultra high-performance concrete (UHPC).

Xiao et al. (2012) used two-dimensional nondestructive digital image correlation to study the crack propagation of modeled recycled aggregate concrete (MRAC) and recycled aggregate concrete (RAC) under uniaxial compression. Idealized concrete specimens were designed (comparable to Buyukozturk et al. (1971)) to hold nine cylindrical aggregate models with a diameter of 1.1 in. (28 mm). Concrete mixtures of various strengths surrounded the idealized aggregates (MRAC and RAC) to produce prismatic specimens with 5.9 in. × 5.9 in. × 1.2 in. (150 mm × 150 mm × 30 mm) dimensions. Two 0.008-in.-thick (0.2 mm) polytetrafluoroethylene (PTFE) sheets were applied at the compression interface to reduce end confinement. "Small strain localizations" (Xiao et al., 2012) were observed at the interfacial transition zone (ITZ) after reaching 45 % of the peak load, and microcracks in the mortar region formed at 75 % of the ultimate strength. Unstable cracking produced vertical fracture cracks parallel to the applied compressive force as shown in Figure 2.5. "The splitting cracks [...] indicate that PTFE layers effectively

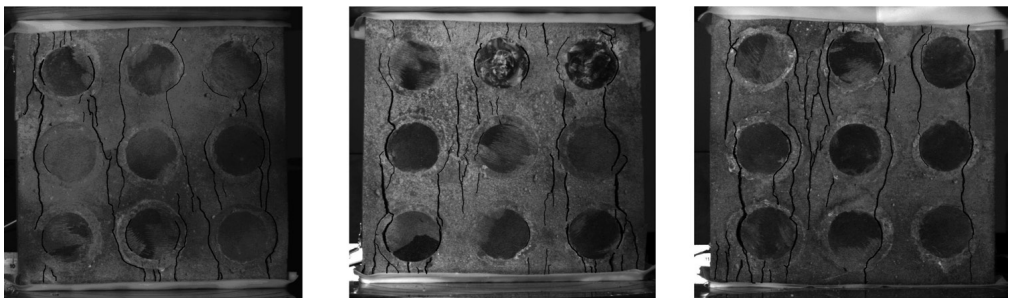

Figure 2.5: Crack patterns of MRAC specimens according to (Xiao et al., 2012)

reduced the frictional restraint [...] between the specimen and the loading

platen" (Xiao et al., 2012). It was concluded that the largely nonlinear stress-strain relationship resulted from the ITZ between aggregates and hardened mortar for both concrete types alike. The crack patterns appeared to be dependent on the relative strength of the used constituents, and the authors proposed to use the idealized concrete models to simulate the behavior of real RAC.

2.3 Shape and Size Effect

A remarkable early work on the influence of sample sizes and shape on concrete strength measurements was done by Gonnerman (1925) who studied prisms and cylinders of different heights and aspect ratios as well as cubes with diverse dimensions. As shown in Figure 2.6, for cylinders with a constant height-to-diameter ratio (h/d or slenderness) of 2, it was found that the

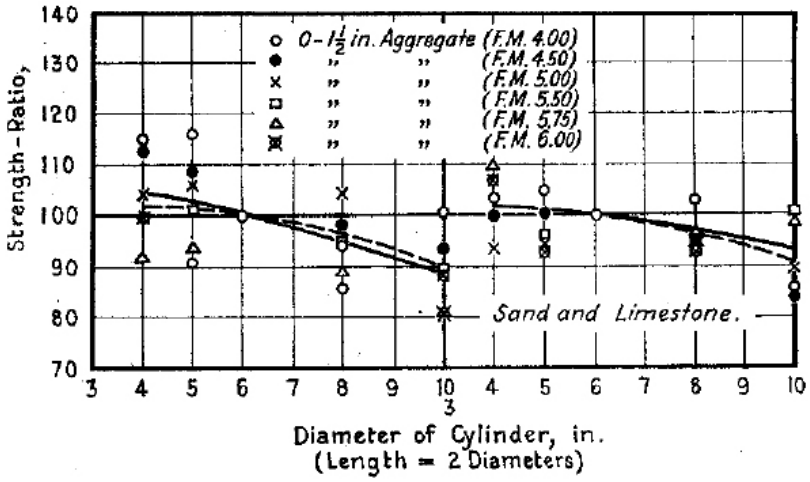

Figure 2.6: Size effect of cylinders with constant slenderness according to Gonnerman (1925)

measured strength increases as the cylinder size decreases. Similarly, prisms under constant slenderness weakened with increased height. The strength of stocky cylinders (h/d = 0.5) was reported to be 178 % larger than that of 6 in. × 12 in. (152 mm × 305 mm) cylinders, and cubes were stronger by 13 % to 18 %. Blanks and McNamara (1935) showed that the cylinder strength decreased, under constant aspect ratio and for aggregate sizes smaller than $\frac{1}{4}$ of the cylinder diameter, as the height increases from 4 in. to 72 in. (0.1 m to 1.83 m), but approaches constant values beyond 48 in. (1.22 m) as graphed in Figure 2.7. Similar findings were made by Gyengo (1938) for columns and

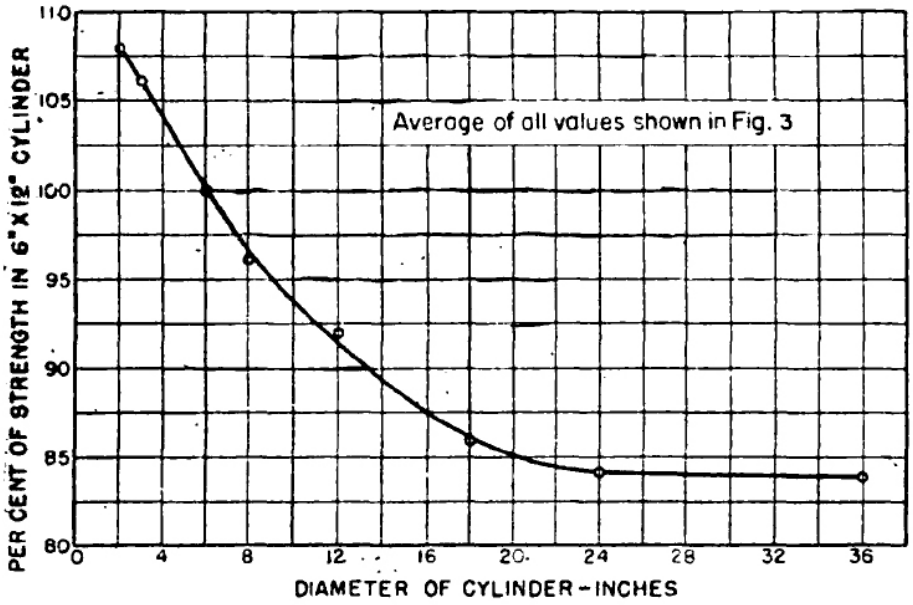

Figure 2.7: Effect of cylinder size on the compressive strength on concrete as reported by Blanks and McNamara (1935)

cubes of different shapes. The strength of square prisms decreased rapidly at first with increasing slenderness ratio, but leveled out at slenderness ratios of 1:3. Cubes of 8-in. (200 mm) edge length were found to be 25 % stronger than

the American standard cylinder of 6 in. × 12 in. (152 mm × 305 mm).

Tucker (1945) used the summation-strength theory to explain the size effect. Accordingly, the compressive strength standard deviation decreases as the specimen diameter increases, and the strength is independent of the specimen area provided that the length-to-diameter ratio is constant (for compression tests). Neville (1956) applied statistical methods to study the ultimate strength of different concrete cubes and observed behavior comparable to Gyengo (1938) and Tucker (1945); a correlation between the strength of concrete specimens and their volume was proposed.

In 1965, Hughes and Bahramian (1965) noticed that " [...] the crushing strength of prisms or cylinders tends towards a constant value as the height-to-width ratio of the specimen is increased", and it was proposed that these effects are due to friction at the compression interface. This was analyzed by comparing strength results of 4-in. (100 mm) cubes to 4 in. × 4 in. × 9.65 in. (102 mm × 102 mm × 244 mm) prisms, which were tested with a combination of polyester film, grease, and hardened aluminum sheets (M.G.A.). Although the so-called M.G.A. pads were damaged after each test, consistent results were obtained, and it was found that the strength results of cubes and prisms were contiguous, and that cracking occurred consistently in vertical planes, parallel to the applied compressive force (Figure 2.8). The slightly higher compressive strength values of cubes were attributed to the remaining friction and the small difference between the lateral expansion of the aluminum and the concrete. The reported data showed significant strength reduction, relative to conventionally tested concrete specimens, but the phenomenon was not acknowledged by the authors. It was shown that the lateral expansion throughout the specimen is more uniform when contact friction is reduced and

Figure 2.8: Vertical crack patterns obtained by using M.G.A. pads (Hughes and Bahramian, 1965)

that the samples deformed "far less" in the longitudinal and lateral directions than conventionally tested specimens. Moreover, the test data revealed that cubes are stronger than prisms, regardless of the evaluated test conditions. This led to the assumption that the platen friction reaches a maximum value which varies depending on the concrete specimen and the platen surfaces. It was understood that cubes (prisms were not mentioned) do not indicate the "true" uniaxial concrete strength, though tested with M.G.A pads. Yet, the M.G.A pads were strongly recommended for biaxial and triaxial testing.

Based on data available in the literature, Neville (1966) proposed a general relationship between concrete specimens of different size and shape. Strength was suggested to be a function of three variables: the specimen height, its maximum lateral dimension (diameter or edge length), and its volume. To evaluate the preferable specimen dimension for quality control, Malhotra (1976) compared the strength differences between 6 in. × 12 in. (152 mm × 305 mm) and 4 in. × 8 in. (102 mm × 203 mm) cylinders from six different concrete projects to prove higher compressive strengths for smaller cylinders. The measurements revealed greater strength variability for increasing concrete strength, which was attributed to increasing stiffness levels. A hypothesized "density effect" for smaller specimens could not be confirmed by the presented test data. However, the results revealed that the standard deviation of compres-

sive strengths increases while the cylinder diameter decreases — as it was proposed by Tucker (1945). Consequently, Malhotra (1976) recommended tall cylinders for standard quality control. Moreover, it was found that more test samples are required to guarantee equal precision (lower variance in strength results) — according to the test data twice as much.

While analyzing the post-failure behavior of concrete under uniaxial compression, Kotsovos (1983) noticed that the strength performance of a specimen is influenced by the compression interface, and the researcher made use of different anti-friction media to confirm an insignificant impact on the ascending portion of the stress-strain curve (using strain gauges at the cylinders mid-height). The post-ultimate behavior on the other hand and the ultimate

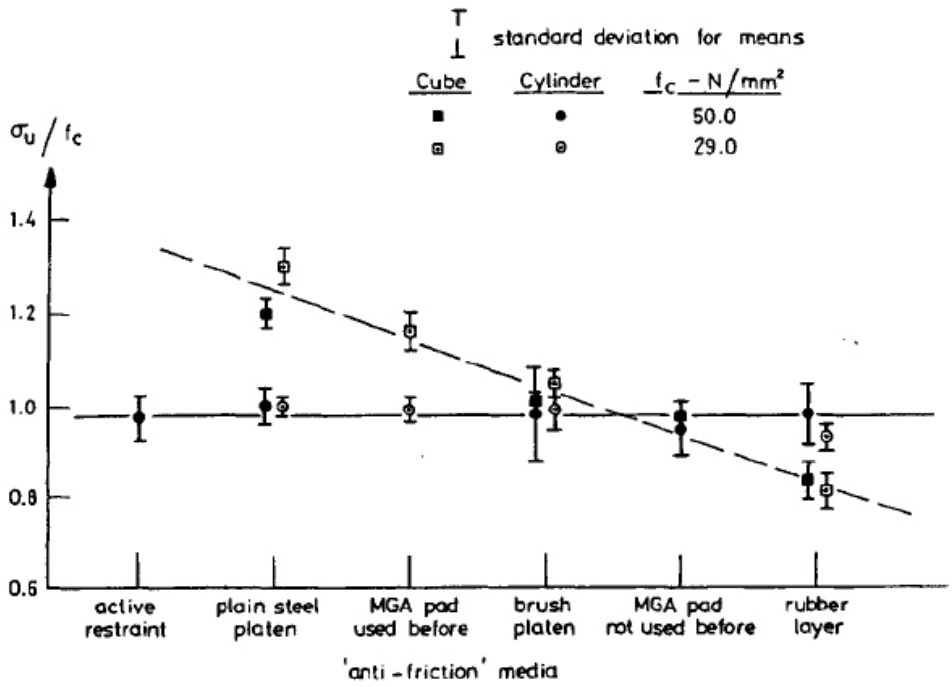

Figure 2.9: Strength variation due to different anti-friction media as reported byKotsovos (1983)

compressive strength appeared affected according to Figure 2.9.

Pistilli and Willems (1993) studied the strength variation of typical sample sizes, and it was concluded that "the ratio of 4 in. × 8 in. (102 mm × 203 mm) to 6 in. × 12 in. (152 mm × 305 mm) cylinder strengths ranged from 0.96 to 1.06. The strength differences due to cylinder size did not appear to be of practical significance for concretes with actual measured strengths ranging from 4000 psi to 9000 psi (28 MPa to 62 MPa)" (Caldarone and Burg, 2009).

To examine the effect of nonstandard curing regimes, Day and Haque (1993) evaluated two different cylinder types and showed that the strengths of 3 in. × 6 in. (76 mm × 152 mm) and 6 in. × 12 in. (152 mm × 305 mm) cylinders are statistically identical. The analysis suggested that this relationship might be valid for concrete strengths up to 7250 psi (50 MPa).

To study the effect of shape, size, and casting direction on the stress-strain curve of HSC, Chin et al. (1997) tested cylinders, prisms, and cubes of different proportions and stated that larger specimens provide lower strength and lower toughness indices, but with a vanishing effect for dimensions less than 4 in. (100 mm). It was concluded that the use of cylindrical specimens generally results in lower strength and lower strain at peak stress. Yazici and Sezera (2007) analyzed eight different concrete mixtures in an attempt to relate the measured concrete strength of different cylinder types to each other. A conversion factor of 103 % was proposed for 4 in. × 8 in. (102 mm × 203 mm) cylinders, while the difference in strength was explained by surface friction and the reduced probability for microcracks and defects in smaller specimens.

Turkel and Ozkul (2010) aimed to eliminate the wall effect for cubes of four different edge lengths and showed that dimensional effects still exist (Figure 2.10) after disregarding the outermost mortar layer of molded specimens.

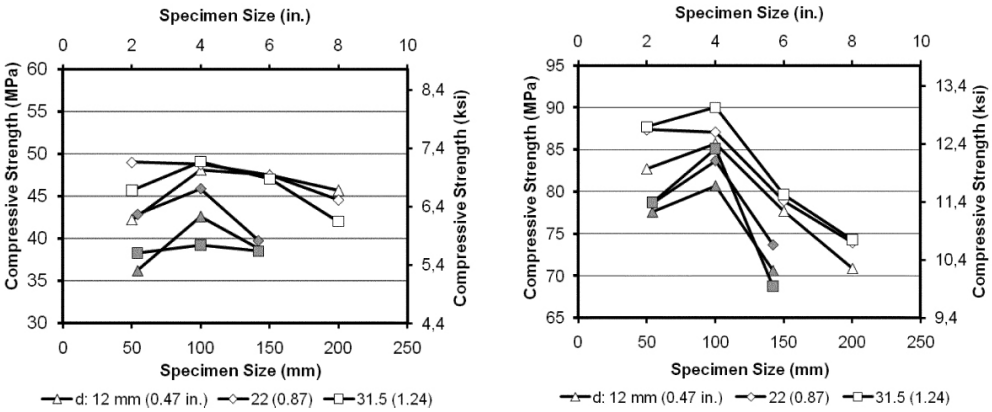

(a) For moderate-strength concretes (b) For high-strength concretes

Figure 2.10: Compressive strength variation according to Turkel and Ozkul (2010)

CHAPTER 3

EXPERIMENTAL PROGRAM

3.1 Introduction

To analyze the rupture behavior of concrete in compression, an experimental program was developed to study crack initiation, crack propagation, concrete strength, and final rupture patterns of typical concrete specimens. This chapter describes the experimental strategy and details the techniques/procedures used to obtain methodologically sound data.

The fundamental approach will be described first and is followed by the utilized materials, their constituents, and their physical properties. Afterwards, the specimen preparation, measurement techniques, and utilized equipment will be described.

3.2 Experimental Design

The influence of surface friction is a known and important factor during multiaxial concrete testing (Buyukozturk et al., 1971; Kupfer et al., 1969; Tschegg et al., 1994), but only a few studies have been carried out to quantitatively

analyze its impact on standard uniaxial compression tests. Studies in this area have been conducted primarily with regard to high strength concrete, focusing on the special strength requirements of the contact surfaces (Burg et al., 1999; Carino et al., 1994; Hampel, 2006; Lessard et al., 1993; Pistilli and Willems, 1993). However, the lateral restraint is assumed to influence the concrete strength significantly (Mills and Zimmerman, 1970; Roddenberry et al., 2011; Taylor, 1971; van Mier and Man, 2009) and, therefore, is of fundamental importance.

The experimental program aims to generate test data suitable for evaluating the failure behavior of concrete under compression. Assuming that friction at the compression interface impacts the strength and fracture behavior, a program was developed to study two different lateral restraints on a variety of four geometrically diverse specimen types. The following test concept is a ramification of the assumed strain behavior of typical concrete specimens under uniaxial compression. Such strain behavior, according to the underlaying test concept, is illustrated in Figure 3.1. Due to Poisson's ratio, any specimen made of concrete experiences lateral deformation under longitudinal compression (ASTM-International, 2002c); usually between 15 % and 20 % (Mehta and Monteiro, 2005), while a value of 20 % is normally assumed in concrete design (Prestressed Concrete Institute, 2004). The lateral deformation, however, is typically restrained at the specimen ends because the standard bearing plates are made of regular hardened steel. In fact, the difference in Poisson's ratio between the steel and concrete causes friction between the two contacting materials (Tschegg et al., 1994) and, in consequence, the specimen tends to bulge out according to Figure 3.1(a). To generate a more uniform deformation, the lateral restraint at the two contacting materials has to be reduced. This

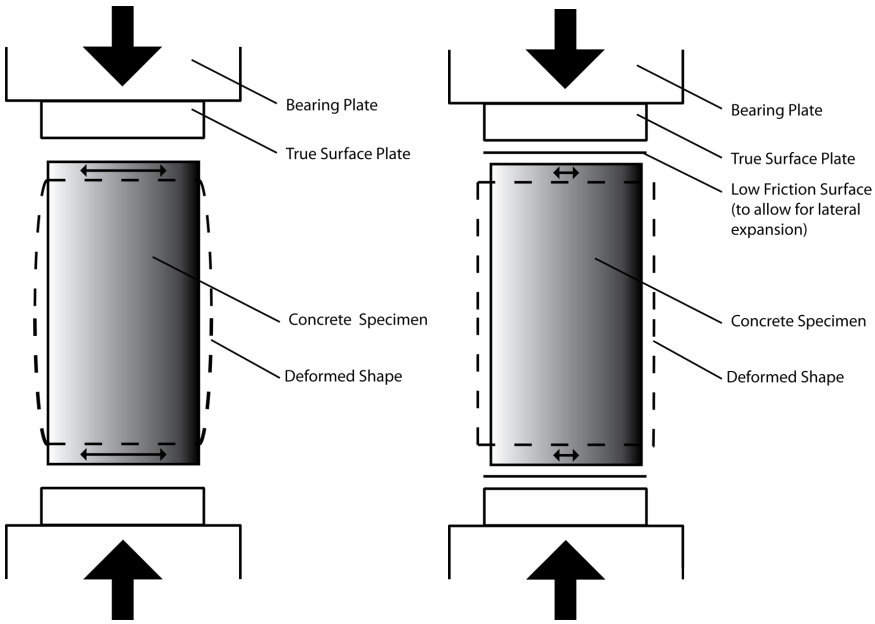

(a) Under regular friction (b) Under low friction

Figure 3.1: Strain behavior of test specimen

may be achieved by introducing a low friction layer as shown in Figure 3.1(b). Section 3.8 provides specific information on the low friction interface that was used for this study, but at this point it is emphasized that the experimental program was designed to include a control group according to Figure 3.1(a) and a test group according to Figure 3.1(b).

It is presumed that the deformation behavior shown in Figure 3.1 is independent of the chosen sample shape or size and that the frictional restraint impacts the failure behavior regardless of the specimen type. To analyze this hypothesis, the experimental program was sectioned into four different sample types (test series) according to Figure 3.2, each with a control group and a test group. Test series 1 and 2 were comprised of two different cylindrical shapes with a length-to-diameter ratio of 2; namely 12-in. (305 mm) length with 6-in. (152 mm) diameter for test series 1 and 8-in. (203 mm) length with

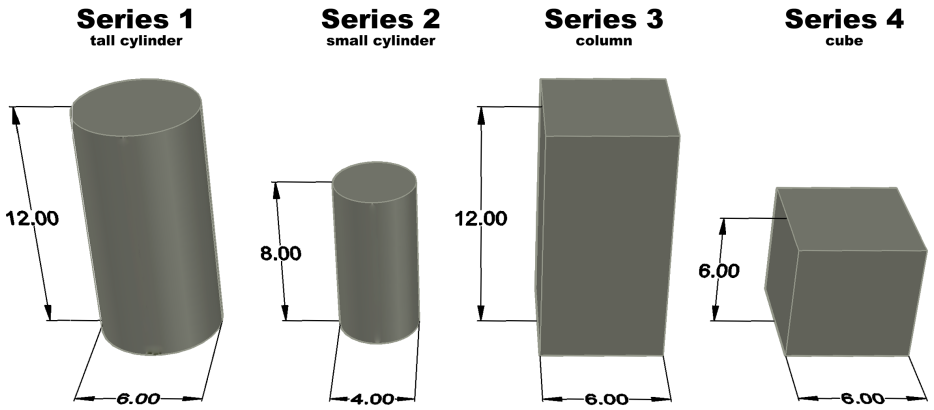

Figure 3.2: Test series (dimensions in inches)

4-in. (102 mm) diameter for test series 2. Rectangular prisms were studied in test series 3 and 4, encompassing columns of 12-in. (305 mm) length and a 6 in. × 6 in. (152 mm × 152 mm) cross section in test series 3 and cubes with a side length of 6 in. (152 mm) in test series 4. Each test series incorporated 20 specimens, to provide 10 samples in each of two groups as highlighted by the experimental design in Table 3.1.

Table 3.1: Experimental design

Series	Type	Specimen Quantities			
		Control[1]	Test[2]	Series	Total
1	Tall Cylinder	10	10	20	80
2	Small Cylinder	10	10	20	
3	Column	10	10	20	
4	Cube	10	10	20	

[1] Conventional surface friction
[2] Reduced surface friction

To analyze the control group and test group for concrete strength, crack

initiation, crack propagation, failure behavior, and final fracture patterns, all test data were digitally recorded, and high-speed video technology was utilized to capture the collapsing specimens at 2000 fps. The specific equipment, test methodologies, and corresponding measuring techniques are outlined later in this chapter (Section 3.6 to 3.11), subsequent to the description of the materials chosen for the specimens.

3.3 Mix Designs

To guarantee proper comparison of test results throughout the entire experimental program, it was important to select a standard strength concrete with low or negligible strength gain after the first 28 days of curing. Such properties were found in a Florida Department of Transportation (FDOT) approved mix design as it is used by the local construction industry. Accordingly, a 4000-psi (27.6 MPa) concrete mixture, free of mineral admixtures (fly ash, blast-furnace slag, silica fume, etc.) and with a water-to-cement ratio of 0.46, was used. Table 3.2 details the selected mix design and shows the proportions of each constituent. The theoretical unit weight of the hardened concrete was 141.4 pounds per cubic foot (pcf), and the air content was around 4.5 %. This specific mix design had a target slump of 4 in. $\pm$ 1 in. (102 mm $\pm$ 25.4 mm) and is marked by the supplier, Florida Rock Industries, Inc., as Product B57CC.

3.4 Materials

All material components were in compliance with their corresponding ASTM standards. While most performance criteria were tested by third parties, the

Table 3.2: Concrete mix design

Constituents	Type	Weight $\frac{\text{lbs}}{\text{yd}^3}$	Mass $\frac{\text{kg}}{\text{m}^3}$
Cement	II	570	338
Coarse aggregates	# 67 Stone	1750	1038
Fine aggregates	Silica Sand	1232	731
Water	N/A	262	155
Admixture 1	Air Entrainer	1.6 oz.	61.9 ml
Admixture 2	Water Reducer	40.3 oz.	1,559 ml
Total		3817	2264

[1] Conventional surface friction
[2] Reduced surface friction

results were shared by the material suppliers. The following subsections outline each constituent separately and discuss their physical properties according to the specified requirements.

3.4.1 Cementitious Materials

The cementitious components for this study consisted of Type II cement as specified by ASTM C 150 (ASTM-International, 2002b). General use and sulfate resistance make Types I & II the most commonly-supplied cements in Florida. The two cement types are almost identical — most other countries do not differentiate between them (Mehta and Monteiro, 2005) — except that ASTM C 150 (ASTM-International, 2002b) limits the C_2A content to 8 % for Type II cements and prescribes a maximum limit of 58 % of the sum of C_3S and C_3A when a moderate heat of hydration is desired. Because this research analyzes small test samples with volumes far below regular structural components, moderate hydration heat was preferable, and a Type II cement was

chosen. The physical and chemical properties of the employed cement have been evaluated by Florida Rock Industries, Inc. and are outlined in Table 3.3 along with the ASTM C 150 (ASTM-International, 2002b) requirements. Ta-

Table 3.3: Standard chemical requirements of cement and test results

Chemical Compounds	Test Result %	ASTM C 150 Requirements
Silicon Dioxide (SiO_2)	20.68	20.0 Min
Aluminum Oxide (Al_2O)	5.02	6.0 Max
Ferric (Iron) Oxide (Fe_3O_2)	3.69	6.0 Max
Calcium Oxide (CaO)	64.28	...
Magnesium Oxide (MgO)	0.72	6.0 Max
Sulfur Trioxide (SO_3)	3.02	3.0 Max
Lose on ignition	2.01	3.0 Max
Insoluble Residue	0.14	0.75 Max
Alkalies as (Na_2O)	0.34	0.60 Max
Tricalcium Silicate (C_3S)	64.5	...
Dicalcium Silicate (C_2S)	7.8	...
Tricalcium Aluminate (C_3A)	7.1	8.0 Max
Tetracalcium Aluminoferrite (C_4AF)	11.2	...
$CaCO_2$ in Limestone, %	97.0	70.0 Min
Limestone, %	2.0	5.0 Max

ble 3.3 shows that the used cement is suitable and in complete conformity with ASTM C 150 (ASTM-International, 2002b); its specific gravity attains 3.15.

3.4.2 Fine Aggregates

The fine aggregates used for the concrete mixture are made of natural minerals from sedimentary rock/silica sand (carbonate rock) and were mined from

Quarry Mine # 47-314 in Florida. The particle size ranges from 75 µm to 4.75 mm (# 200 sieve to # 4 sieve). Its properties are constantly controlled at the pit, and Florida Rock, Inc. made the test results available. Accordingly, the specific gravity of the fine aggregates amounts to 2.66. The results of the sieve analysis and the specified grading ranges according to ASTM C 33 (ASTM-International, 2003a) are outlined in Table 3.4. The chart in Figure 3.3 illustrates the gradation of the concrete sand and emphasizes that the particle distribution conforms to ASTM C 33 (ASTM-International, 2003a). The fineness modulus, FM, of the sand mixture was determined according to Equation 3.1:

Table 3.4: Gradation and specifications for concrete sand

Sieve Size			Retaining	Passing	Grading Range	
US	in.	mm	%	%	min %	max %
# 4	0.187	4.75	0	100	95	100
# 8	0.093	2.36	2	98	85	100
#16	0.046	1.18	14	84	65	97
# 30	0.024	0.60	27	57	25	70
# 50	0.012	0.30	34	23	5	35
# 100	0.006	0.15	20	3	0	7
# 200	0.003	0.075	3	0	0	4
Sum			100	365[1]	275[1]	413[1]

[1] ζ (sum of percentage passing)

$$FM = \frac{N(100) - \zeta}{100} \tag{3.1}$$

where N is the number of sieves with mesh openings larger than or equal to 150 µm (# 100 sieve), and ζ is the sum of percentage passing. Thus, the fine-

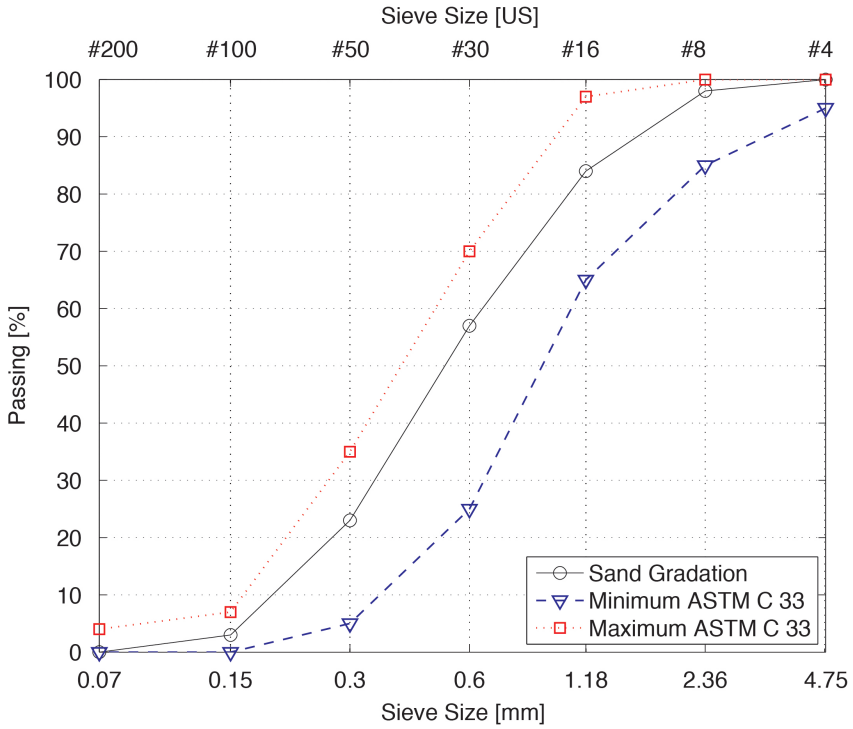

Figure 3.3: Concrete sand gradation chart

ness modulus amounts to 2.35, and the used concrete sand can be considered very fine, as the majority of the material is retained by the second (0.30 mm or # 50) sieve (Neville, 1996).

3.4.3 Coarse Aggregates

The particles with grain sizes bigger than 4.75 mm (# 4 sieve) are considered coarse aggregates (ASTM-International, 2003a; Mehta and Monteiro, 2005). In this research, those aggregates were made of a sedimentary rock consisting predominantly of calcium carbonate, commonly referred to as limestone. The coarse aggregates were mined from Quarry Mine # 38-268 in Florida and screened to qualify as 67-Stone gradation. Sieve analysis, characterizations, and gradation are constantly conducted at the mine, and Table 3.5 presents

the findings. Figure 3.4 graphs the gradation of the coarse aggregates and

Table 3.5: Gradation and specifications for limestone 67-stone

Sieve Size			Retaining	Passing	Grading Range	
US	in.	mm	%	%	min %	max %
1	1.0	25.40	0	100	100	100
$\frac{3}{4}$	0.75	19.05	14	86	90	100
$\frac{3}{8}$	0.375	9.53	49	37	20	55
# 4	0.187	4.75	31	6	0	10
# 8	0.093	2.36	2	4	0	5
Sum			96	233[1]	210[1]	270[1]

[1] ζ (sum of percentage passing)

shows the particle distribution envelope required by ASTM C 33 (ASTM-International, 2003a). Slight discrepancies can be observed for 0.75-in. stones; however, the grading is within acceptable ranges for the purpose of this research. The fineness modulus of the limestone 67-stone was calculated according to Equation 3.1 with a value of 2.67, and the specific gravity was measured at 2.560 (SSD).

3.4.4 Admixtures

Two liquid admixtures were added to the mix: one admixture for air entraining purposes per ASTM C 260 (ASTM-International, 2010) and another one for water reduction and retarding per ASTM C 494 (ASTM-International, 2004a) Type D.

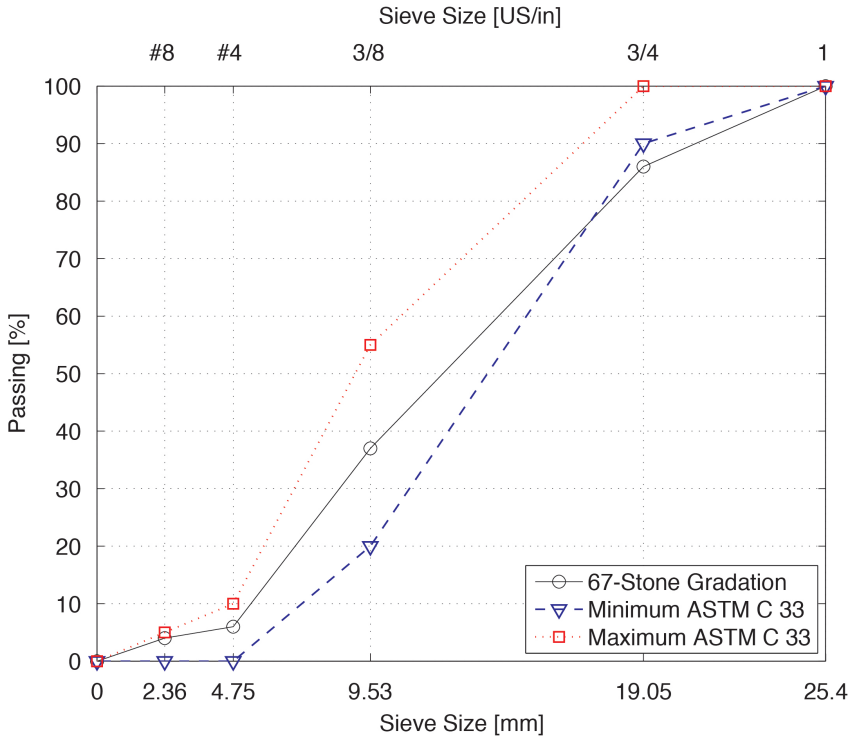

Figure 3.4: 67-Stone gradation chart

3.5 Mixing and Batching

All specimens were cast from one single concrete batch that was obtained from a local concrete supplier[1] and was batched and pre-mixed at the concrete plant before drum mixing trucks delivered it to the laboratory. The required amount of fresh concrete was determined based on the specifics provided in Table 3.6. To compensate for material losses during specimen preparation, 120 % of the required volume was mixed and delivered. Immediately after truck arrival, slump tests were carried out according to ASTM C 143 (ASTM-International, 2003b). The concrete was discarded if the measured slump exceeded 4 in. ± 1 in. (102 mm ± 25.4 mm). If, on the other hand, the value

[1]Florida Rock Industries, Inc., 1005 Kissimmee St, Tallahassee, FL 32310

Table 3.6: Geometric properties of concrete specimens

Specimen	Cross section		Height/Length		Volume	
	$in.^2$	mm^2	in.	mm	$in.^3$	L
Tall Cylinder	28.27	18,238	12	304.8	339.24	5.56
Small Cylinder	12.57	8,110	8	203.2	100.56	1.65
Column	36.00	23,226	12	304.8	432.00	7.08
Cube	36.00	23,226	6	152.4	216.00	3.54

undercut the target slump, additional water was added to the mixture and the mixing procedure was continued. After adequate mixing, the test was repeated until the slump was acceptable.

3.6 Specimen Preparation

All specimens were cast simultaneously using internal vibration for compaction with two layers per specimen following the standard practice for making and curing concrete test specimens in the laboratory according to ASTM C 192 (ASTM-International, 2002a) and AASHTO T 126 (American Association of State Highway and Transportation Officials, 2001). The material was funneled into the molds in two layers while vibration was applied after each layer. Vibration was continued only long enough to achieve proper consolidation. The molds, then, were covered with plastic lids or tarps to impede vaporizing water. Finally, the freshly prepared specimens were stored on a leveled surface.

The molds were removed after 24 hours to moisture cure all test samples in water tanks. The lime water was concentrated at 0.35 oz (10 g) of lime per 1 gal. (3.79 L) of water while its temperature was maintained around

73.5 °F ± 3.5 °F (23.0 °C ± 2.0 °C). Figure 3.5 graphs the hourly water temperature readings of the two storage/water tanks as well as the ambient air temperature to confirm the constant curing conditions throughout the moisture treatment. While the ambient air temperature reached values between 69 °F

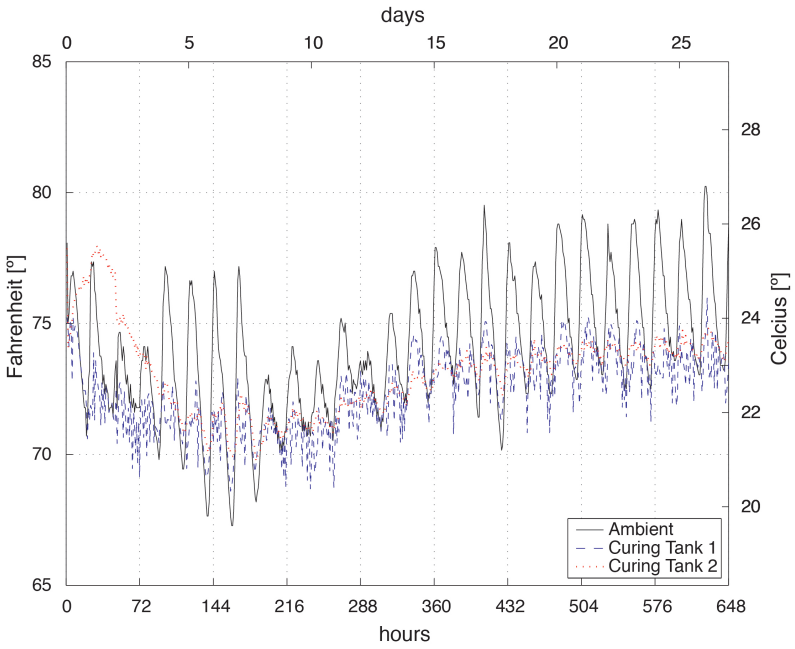

Figure 3.5: Curing temperature throughout curing period

and 80 °F (21 °C and 26 °C), the temperature cycles of the two water baths maintained stable values within the prescribed temperature range specified by ASTM-International (2002a). The specimens were removed from the water bath 28 days after casting. To eliminate the normally required neat cement or sulfur caps according to ASTM C 617 (ASTM-International, 1998) and to allow for proper comparison of cylinder and prism test results, the cylindrical specimens were ground to be parallel on both ends using the commercially-available concrete cylinder end grinder at the FDOT Structures Research Center (Fig-

ure 3.6). The Gilson HM 716A simultaneously mounts four cylinders of ei-

Figure 3.6: End grinder for concrete cylinder

ther 4 in. × 8 in. (102 mm × 203 mm) or 6 in. × 12 in. (150 mm × 305 mm) size, and a complete grinding procedure (for both surfaces) requires approximately 10 minutes per 4 cylinders. After the grinding process was accomplished, the cylindrical specimens were cleaned (hosed with water) and stored, along with all prismatic specimens, at room temperature in a climate controlled environment. All specimens (cylinders, cubes, and columns) were separated into two groups — a test group and a control group with equal sample population — after one week of drying. To reduce the friction at the compression interfaces during compression testing, the end surfaces of the test group samples were coated with two layers of commercially-available dry lubricant graphite paint[2].

In an effort to measure the strain behavior, some cylindrical specimens

[2]SLIP Plate, Heavy Duty, all purpose Lubricant, Dry Film Graphite Lubricant, SUPERIOR GRAPHITE CO., Chicago, IL, 60606 USA

were equipped with strain gauges. The concrete surfaces of those 6 in. × 12 in. (152 mm × 305 mm) cylinders were smoothed with a rotating concrete grinder and P120 sand paper, de-dusted with compressed air, and cleaned with acetone before the strain gauges were adhered to the concrete surface using Cyanoacrylate Zap PT-27 Gel. In agreement with Ross and Hamilton (2011) and based on the experience at the FDOT Structures Research Center, a gauge length of more than two times the maximum aggregate size is most suitable for concrete specimens. Accordingly, 2.2-in.-long (60 mm) strain gauges were used for this study, specifically magnetic field gauges of type MFLA-60-350-1L with a gauge factor of 2.09 ± 1 % and a resistance of 349.5 Ω ± 1.5 Ω, as produced by Tokyo Sokki Kenkyujo Co., Ltd. The strain gauges were applied in the longitudinal and transverse directions at mid-height of the cylinder and arranged in pairs separated by 180° to correct for any bending strains (Ross and Hamilton, 2011).

3.7 Compressive Strength Measurement

All uniaxial strength tests were carried out using a 550-kip (2.4 MN) load frame, model 311.415 as produced by Material Testing Systems (MTS), holding a 6-in.-stroke (152 mm) actuator (model 209.22) with an area of 183 in.^{2} (0.118 m^2) and a 550-kip (2.4 MN) load cell (model 661.32B-02). A model 407-Controller with digital readout monitored the load cell voltage and controlled the actuator at a stress rate of 35 psi/s ± 7 psi/s (0.25 MPa/s ± 0.05 MPa/s).

Uniaxial testing was based on the procedures and methodologies outlined in ASTM C 39 (ASTM-International, 2004b) and AASHTO T 22 (American Association of State Highway and Transportation Officials, 2006); the entire

equipment and hardware components complied with the specified criteria. All experiments were carried out accordingly, applying the compressive force continuously and without shock. The ultimate compressive strength was calculated by dividing the maximum load carried by the specimen by the average cross-sectional area.

3.8 Compression Interface – Bearing Plates

All control group specimens were tested conventionally, with both ground concrete surfaces exposed to the bearing plates of the compression machine. To eliminate interlocking effects at the end surfaces, smooth hardened steel plates without grooved concentric circles were substituted for the regular bearing plates. Special attention was paid to maintain a Rockwell hardness of HRC 55 as it represents the standard hardness of compression plates inside compressive strength testing machines. In the test group, on the other hand, the ground concrete surfaces were coated with two layers of commercially-available dry lubricant graphite paint as outlined in Section 3.6. To further reduce the surface friction of the test group, the bearing plates of the compression machine were equipped with smooth (no grooves) hardened steel plates (HRC 55) that were coated with Tungsten Disulfide/Disulphide (WS2). With a static COF below 0.07 and a dynamic COF of 0.03, tungsten disulfide provides a lower friction restraint than Teflon (0.05) or Graphite (0.1) (Bhushan and Gupta, 1991) and according to the manufacturer[3], it features the lowest COF available in a solid material. This specific type of dry film lubricant coating was chosen for this research because it bonds to metal surfaces without the use of binders and

[3]BryCoat Inc., 207 Vollmer Avenue PO Box 1976, Oldsmar, FL 34677-6976, USA, `http://www.brycoat.com/dry-film-ws2.html`

cannot chip, peel, or flake. Moreover, it withstands high compressive stresses — above 300 ksi (2.07 GPa) — at a thickness of 20 µin. (0.5 µm). Because it is applied to the substrate (hardened steel plates) at ambient temperatures, it does not anneal or warp the substrate material and preserves the levelness of the compression plates.

In an effort to determine the best suited low friction coat for the compression plates, preliminary tests were conducted using a ceramic material marketed as $AlMgB_{14+}$. While the coating satisfactorily fulfilled all performance criteria (e.g., compressive strength and wear down) and in standard applications (industrial tools) provides a COF of 0.02, it did not achieve the desired lubricity in combination with ground or graphite coated concrete surfaces.

3.9 Failure Criterion

In concrete testing and according to ASTM C 39 (ASTM-International, 2004b) and AASHTO T 22 (American Association of State Highway and Transportation Officials, 2006), failure is attained when the load carried by the specimen is less than 95 % of the peak value sustained by the specimen. However, since high-speed video technology was an integral part of this study, a more rigorous failure criterion was needed to guarantee adequate video results. Although the defined failure criterion is influenced by the high-speed video equipment and the data acquisition system, a discussion about these factors will not occur here, as they are outlined separately in Sections 3.10 and 3.11. However, it is important to mention that failure was defined as a specified load drop within a certain time frame. In other words, all specimens were considered to be collapsed if the compressive load fell by more than 5 kip (22 kN) within less

than 5 ms. This failure criterion was found to perfectly coincide with the total break down of all tested specimens.

Preliminary testing was necessary to define a suitable failure criterion, and it is emphasized that at higher load drops within different periods, it was difficult/impossible to video capture the fracturing of the specimens. On the other hand, a lower load drop was found to be too sensitive, resulting in premature termination of the experiments — far before the ultimate strength was reached.

3.10 High-Speed Video Equipment

In an effort to capture the propagation of macrocracks and to study the rupture behavior of concrete, high-speed video technology was employed using the hardware available at the FDOT Structures Research Center (Figure 3.7). This particular equipment consists of a N3 300 ASA Mono High-Speed Camera produced by Integrated Design Tools (IDT), multiple PENTAX™ lenses, tripods, two IDT 19 cell, and two IDT 7 cell light-emitting diode lights. The N3 3000 ASA Mono Camera features a 1.3-megapixel chip, is equipped with a 2-GB on-board memory, and acquires the video footage at a maximum capture rate of 65,000 fps or a maximum resolution of 1280×1024, while each pixel measures $12\,\mu m \times 12\,\mu m$.

In operation, the camera sends out a pulse for every frame it acquires and constantly overwrites its internal memory to buffer the video pictures. This process can be interrupted by triggering the camera either manually or by a specified trigger signal (load drop). Accordingly, the high-speed video equipment was linked to the data acquisition system as illustrated in Figure 3.8

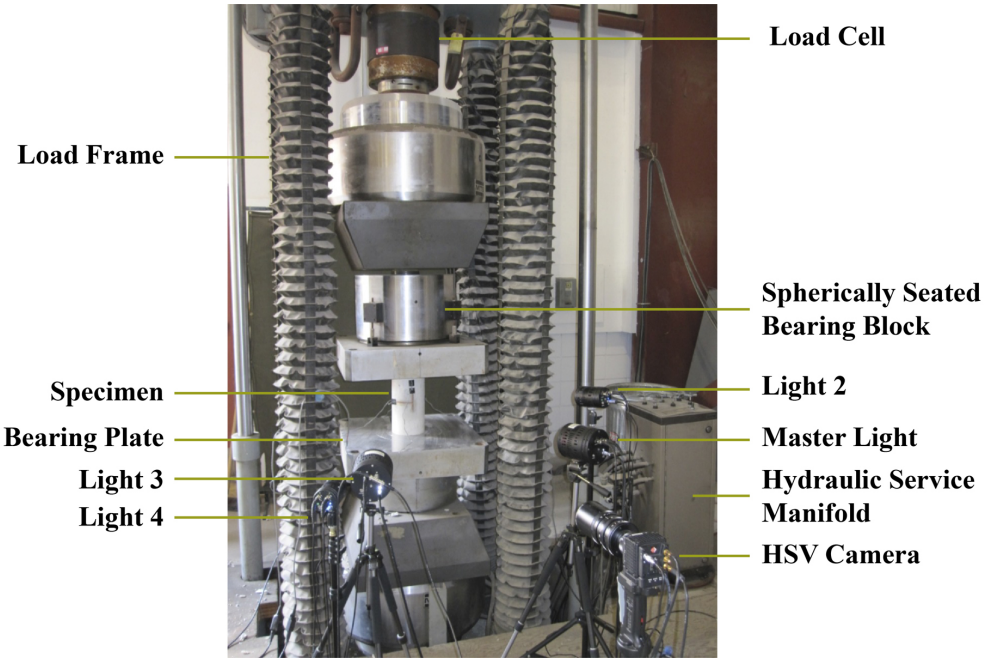

Figure 3.7: Experimental setup

to assure correct timing that guarantees proper capturing of crack propagation and final failure behavior. The trigger marks the event and can be set anywhere within the buffer, so that pre-trigger (before event) and post-trigger (after event) result in a full memory. For this study, the camera was triggered based on the failure criterion defined in Section 3.9 with a measured load drop of 5 kip (22 kN) at a data rate of 200 Hz. Preliminary testing showed that a post-trigger of 0.5 seconds is sufficient to capture the complete macrocrack phase and collapse of concrete specimens. Consequently, at the chosen frame rate (2000 fps) and picture resolution (up to 1280 $\times$ 256), the rupture cracks were captured 2.5 seconds before failure occurred and approximately 3 seconds before complete collapse. Only one camera was used with a single vantage point to capture the "front/North side" of each specimen.

Figure 3.8 also outlines the wiring scheme that was necessary to achieve maximum illuminosity. At capture rates as high as used in this study (2 kHz),

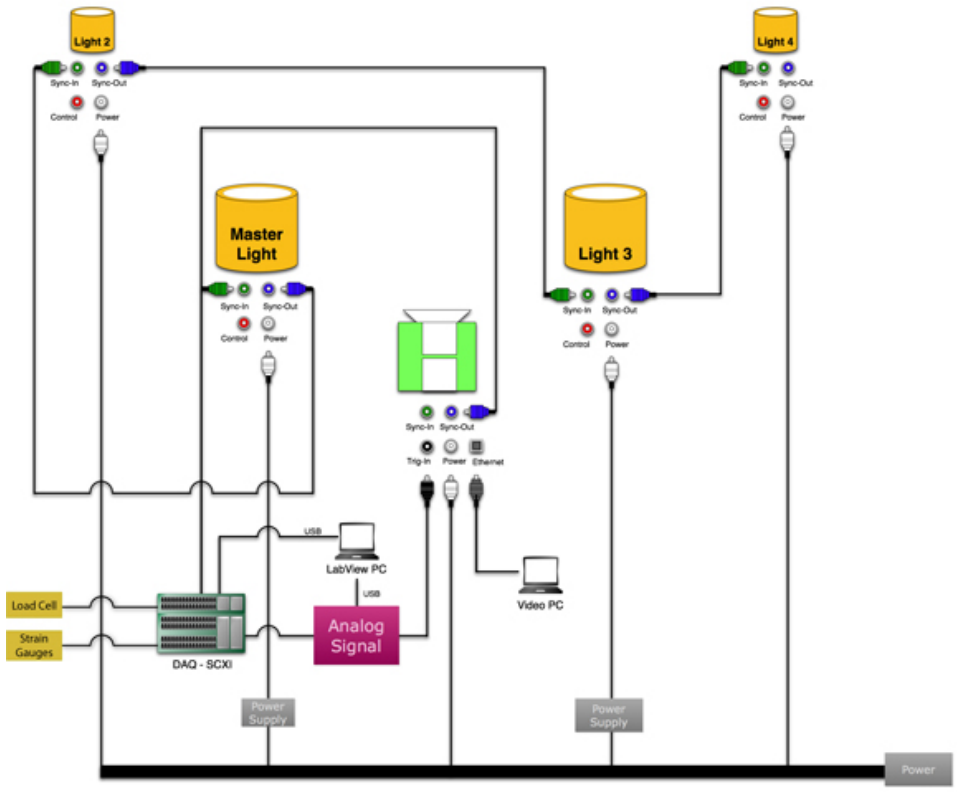

Figure 3.8: Camera setup and data acquisition arrangement

the light source has to be synchronized to the shutter of the camera to produce valuable video footage that does not suffer from "ghosting". This study was one of the first FDOT research projects to take advantage of the high-speed video equipment. Earlier testing was done using four 500-W construction spot lights to illuminate the frames, but the video output did not compare to the quality that was achieved with the synchronized light-emitting diode lights.

3.11 Data Acquisition

All data acquisition was handled by a National Instruments SCXI-1520 eight-channel module that converted the load cell and strain gauge voltages into digital data, which was passed on via USB to a personal computer (see Fig-

ure 3.8) at a sample rate of 2 kHz. The data acquisition system received a pulse from the high-speed video camera at 2 kHz (0.5 ms) that was used to check for synchronization at a rate of 200 Hz (5 ms), while the intermediate 10 data points were autonomously recorded by the SCXI module. A LabView[4] virtual instrument (*vi*) was programmed[5] to analyze the acquired data for the specified load drop. The load behavior was monitored at the load cell inside the MTS test frame and evaluated in a software buffer that was designed to store the data in packages of 10 readings (0.005 s). Failure was achieved when the first reading differed from the tenth reading by more than 5 kip (22 kN), which caused the *vi* to send a trigger signal (via USB through the analog signal converter) to the high-speed camera.

To prevent large file sizes and to avoid unnecessary data prior to concrete failure, a second buffer was programmed that accepted the raw data from the first buffer to determine the average (per channel) over one second or 2000 data points; i.e., as long as the first buffer did not detect the load drop, the stored data was reduced/averaged to a sample rate of 1 Hz (inside the second buffer). However, the sample rate conversion did not happen immediately but was buffered as well, over a timeframe of three seconds to align the recorded text data (strain, load, etc.) — of each test file — with the frames captured by the high-speed video camera. The final three seconds (camera buffer at 2000 fps) of each test were stored at a sample rate of 2 kHz.

It is emphasized that the event (failure) may happen at any point in time and not necessarily at an integer second. To avoid the loss of data, this had to be considered. For example, if the load drop occurred at 120.4 s, the first 120 s

[4]National Instruments (2009). *LabVIEW 2009 (32 and 64-bit).* Build 9.0.0.4022, (Software).

[5]by Seth Murphy, FDOT Structures Research Center

would be written, but the following 0.4 s would be lost. This was compensated for by recording all data before writing the 2-kHz data to file. In such cases, the average was determined from a smaller, not full second, data set (0.4 s). While not all events occurred on the full second, no data was lost.

The use of a software trigger at such high data rates results in a lag time between software and hardware. Because the acquired data had to be constantly analyzed for the specified load drop, an offset between the recorded text data and video pictures is unpreventable; this offset depends on the computing power of the personal computer executing the *vi*. In other words, initially the raw data was not perfectly synchronized and had to be post-processed using the frame delays shown in Table 3.7. An adequate hardware trigger could solve

Table 3.7: Software-hardware delay (in frames[1])

Sample	Series 1	Series 2	Series 3	Series 4
1	211	159	192	284
2	137	216	182	289
3	261	175	223	216
4	151	186	183	219
5	151	169	207	288
6	228	104	233	174
7	198	222	257	140
8	247	144	203	205
9	175	232	235	227
10	277	179	110	230
AVG	203.6	178.6	202.5	227.2

[1] 1 frame = 0.5 ms

this difficulty and prevent the need for post-processing; however, the minimum

offset was calculated with 104 frames (52 ms) and the maximum was found at 439 frames (219.5 ms) with an average delay of 242 frames (121 ms).

CHAPTER 4

TEST RESULTS

4.1 Introduction

This chapter presents the test results and findings that were documented according to the methodologies and procedures outlined in Chapter 3. The following sections provide a detailed description of the laboratory test results and the post-processed data.

The strength measurements are presented first and are followed by the results of statistical evaluations, before the strain measurements are reported. Thereafter, the final fracture patterns are reviewed, which are preceded by the observed crack propagation using example frames captured by the high-speed video equipment.

4.2 Control Strength

The strength development was monitored throughout the entire experimental phase to guarantee a theoretically sound baseline for the comparison of test results between different specimen shapes. Because all specimens were made

from one single concrete batch and testing was conducted over a timespan of several months, reference 6 in. × 12 in. (152 mm × 305 mm) cylinders were assessed at regular intervals before and while testing the actual test specimens in each series. A minimum of three cylinders was conventionally tested for ultimate strength at the age of 3, 7, 28, 56, 84, and 112 days (d) to determine the average strength development of the concrete mixture over time. The average strength measurements of the reference cylinders are graphed in Figure 4.1 along with the test calendar. Evidently, the concrete mixture gained strength

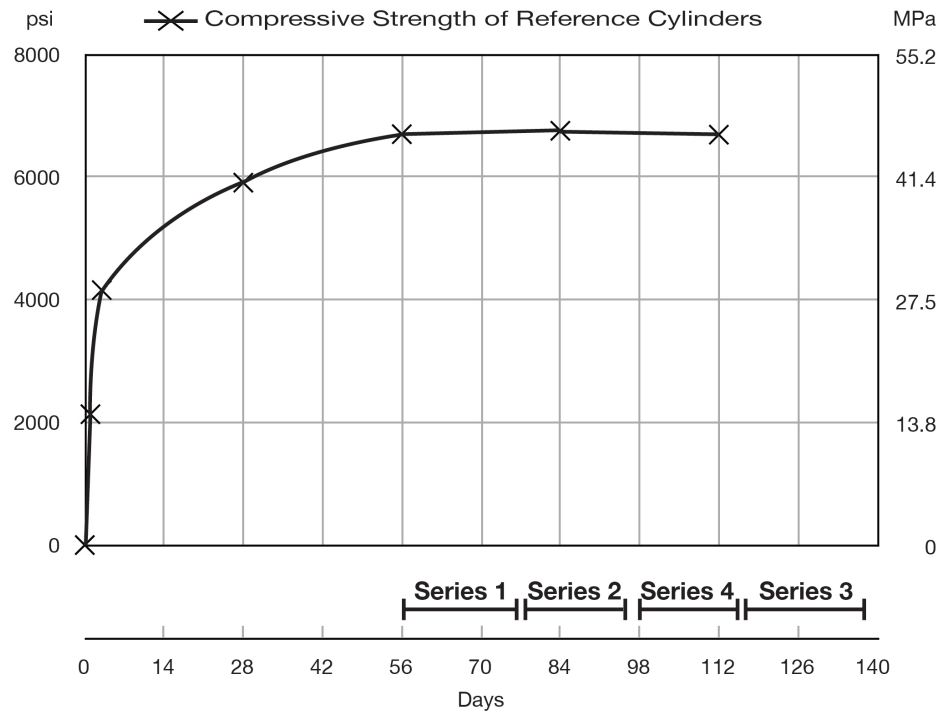

Figure 4.1: Test calendar and compressive strength development

rapidly within the first 28 d, but leveled thereafter, confirming insignificant strength gain after 56 d. The actual test program did not begin before two consecutive average reference cylinder strength results differed by less than

10 %. Consequently, test series 1 (tall cylinders) experiments were initiated at a maturity of 56 d. Series 2 (small cylinders) followed at an age of 80 d, before series 4 (cubes) was tested from 98 d to 114 d. Afterwards, series 3 (columns) was completed. All tests were completed within 138 d of casting.

4.3 Compressive Strength Results

The ultimate strength results of all sample types were determined according to Section 3.7 using conventional compression plates for control group breaks and a low friction compression interface for the test group experiments. Tables 4.1 and 4.2 list the measured strength values in correspondence to their group (control/test) and highlight the minimum (Min), maximum (Max), mean (μ), standard deviation (σ), and coefficient of variation (CV) values per series or shape. The standard deviation ranged between 279 psi (1.9 MPa) and 937 psi (6.4 MPa), averaging at 475 psi (3.3 MPa). With a mean value of 5861 psi (40.4 MPa) throughout all test series (regardless of group), the coefficient of variation ranges between 5.0 % and 15.8 %, far beyond the recommended value of 2.4 % for standard 6 in. $\times$ 12 in. (152 mm $\times$ 305 mm) cylinders prepared under laboratory conditions (American Concrete Institute, 2011b; ASTM-International, 2004b). However, with the exception of series 4 control group samples and series 2 test group specimens, the coefficient of variation attained consistent precision. The divergence from ACI 214 (American Concrete Institute, 2011b) is assumed to be attributable to the comparatively limited sample population within each series.

While Tables 4.1 and 4.2 reveal dissimilar strength results for different specimen types (series), Table 4.3 summarizes the within-group (conventional

Table 4.1: Compressive strength results — Imperial (psi)

	Control Group				Test Group			
	Series 1	Series 2	Series 3	Series 4	Series 1	Series 2	Series 3	Series 4
	6613	7044	5526	8224	5498	5122	4588	6322
	6958	6572	5423	7881	5538	5932	4795	6322
	6854	6273	5522	6940	5831	5481	4476	6443
	7038	6846	5364	6897	5719	3806	5349	5511
	6905	7279	5147	6563	5926	4395	5602	5441
	7289	6729	5513	6876	6377	4184	4276	5975
	6234	6287	5980	6579	5249	3976	4569	5681
	6211	6975	5330	4687	5990	3852	4897	5596
	6668	6396	5579	7052	5719	4784	4966	5682
	6885	6512	4924	7124	5363	4302	5630	6011
Min	6211	6273	4924	4687	5249	3806	4276	5441
Max	7289	7279	5980	8224	6377	5932	5630	6443
μ[1]	6765	6691	5431	6882	5721	4583	4915	5896
σ[2]	342	341	279	937	332	726	473	368
CV[3]	5.0	5.1	5.1	13.6	5.8	15.8	9.6	6.2

[1] μ population mean
[2] σ population standard deviation
[3] CV population coefficient of variation (%)

vs. reduced friction) differences. Overall, the control and test group samples reached different average strength levels. Although the control group measured 22 % higher mean strength values (μ), the coefficients of variation (CV) are comparable. Nevertheless, the apparent strength results were influenced by the shape of the concrete samples and the surface friction at the compression interface as emphasized by Figure 4.2. The specimens tested with conventional surface friction (control group) consistently produced higher apparent strength results than those tested with reduced end confinement (test group). Figure 4.2

Table 4.2: Compressive strength results — Metric (MPa)

	Control Group				Test Group			
	Series 1	Series 2	Series 3	Series 4	Series 1	Series 2	Series 3	Series 4
	45.6	48.6	38.1	56.7	37.9	35.3	31.6	43.6
	48.0	45.3	37.4	54.3	38.2	40.9	33.1	43.6
	47.3	43.2	38.1	47.8	40.2	37.8	30.9	44.4
	48.5	47.2	37.0	47.6	39.4	26.2	36.9	38.0
	47.6	50.2	35.5	45.2	40.9	30.3	38.6	37.5
	50.3	46.4	38.0	47.4	44.0	28.9	29.5	41.2
	43.0	43.3	41.2	45.4	36.2	27.4	31.5	39.2
	42.8	48.1	36.8	32.3	41.3	26.6	33.8	38.6
	46.0	44.1	38.5	48.6	39.4	33.0	34.2	39.2
	47.5	44.9	33.9	49.1	37.0	29.7	38.8	41.4
Min	42.8	43.2	33.9	32.3	36.2	26.2	29.5	37.5
Max	50.3	50.2	41.2	56.7	44.0	40.9	38.8	44.4
μ^1	46.7	46.1	37.5	47.5	39.4	31.6	33.9	40.7
σ^2	2.4	2.4	1.9	6.5	2.3	5.0	3.3	2.5
CV[3]	5.0	5.1	5.1	13.6	5.8	15.8	9.6	6.2

[1] μ population mean
[2] σ population standard deviation
[3] CV population coefficient of variation (%)

graphs the within-series divergence and only suggests an influence of the two dissimilar boundary conditions. Accordingly, Figure 4.3 plots the same mean compressive strength results but in reference to the different surface treatments (per group). The graph clearly shows decreasing strength values due to reduced surface friction, regardless of the evaluated specimen type (series). However, the two analyzed surface properties influenced the strength results differently for dissimilar shapes, as seen by the slope of the trend lines.

Although the coefficient of variation showed consistency (see above), so far,

Table 4.3: Average control group and test group behavior

	Control Group		Test Group		Group Δ^4		
	psi	MPa	psi	MPa	psi	MPa	%
μ^1	6442	44.4	5279	36.4	1163	8.00	22
σ^2	678.7	4.68	630.6	4.35			
CV[3]	10.5		11.9				

[1] μ population mean
[2] σ population standard deviation
[3] CV population coefficient of variation
[4] Δ Difference between control group and test group

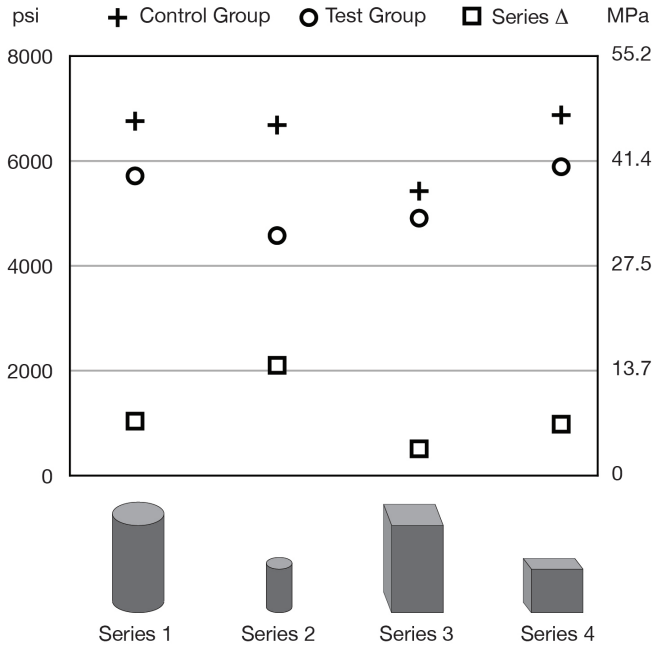

Figure 4.2: Mean compressive strength results and average differences per series

only mean values have been discussed while ignoring the spread of individual data points within each series or group population. For physical relevance, i.e., for reliability of the presented mean values and their reported trends, the distribution of individual data points is considered. Inferential data analysis was applied using a 4×2 factorial Analysis of Variance (ANOVA) with factor

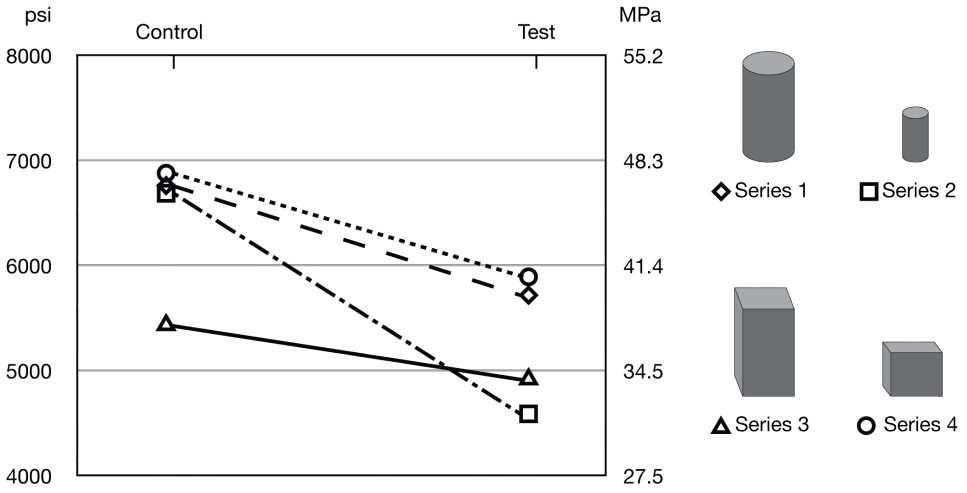

Figure 4.3: Mean compressive strength results per group

shape (series 1, 2, 3, and 4) and factor surface treatment (control group vs. test group) to evaluate the shape effect as well as the influence of surface friction, individually and combined, under statistical significance. The input matrix for the statistical analysis consists of the acquired strength results as outlined in Tables 4.1 and 4.2. The confidence level for this study was found to be appropriate at 95 % ($\alpha = 0.05$) to reduce the chance of type 1 errors (false positive) to less than 5 %.

Based on the available 80 data points, the ANOVA revealed a significant main effect for shape with $F(3,72) = 23.191$, $p < 0.001$. For proper interpretation of the main effect, post-hoc analysis was applied using pairwise comparison (Bonferroni corrected), proving a significant difference between all test series except between series 1 and series 4 (tall cylinder vs. cube) according to Table 4.4. In addition, the ANOVA showed a significant effect for the surface treatment, $F(1,72) = 99.070$, $p < 0.001$. This was further evaluated (post-hoc) by Student's t-test, since it is appropriate to study the influence of surface friction on ultimate strength within each series separately. The null hypothesis

Table 4.4: Pairwise comparison of main effect (P–Values)

	Series 1	Series 2	Series 3	Series 4
Series 1		0.003	$\leqslant 0.001$	n.s.
Series 2			0.038	$\leqslant 0.001$
Series 3	Sym.			$\leqslant 0.001$
Series 4				

n.s. = not significant

assumes that the control and test groups are similar, with differences due to chance (per series), while Student's t-test evaluates this null hypothesis and accepts it to be true for p-values above 0.05 (95 % confidence level). The t-test results of all four series are outlined in Table 4.5 together with the mean values, standard deviation, and the percentage of strength reduction within each series. The one-tailed (hypothesizing strength reduction) t-test with the assumption of non-equal variance (heteroscedastic) results in p-values far below 0.01 for each data set, implying statistical significance for all four test series, i.e., the null hypothesis can be rejected and the reliability of lower strength results for reduced end confinement is proven within the 95 % confidence interval — independent of the evaluated specimen types. Based on Figures 4.2 and 4.3, it was previously stated that, on average, the control group specimens (conventional surface friction) sustained higher ultimate loads than the specimens in the associated test groups (low surface friction); the t-test results now confirm statistical significance of this general trend.

A maximum apparent strength difference of 31.5 % was observed for series 2, whereas the minimum difference of 9.5 % was found for series 3. This alluded to a combined influence of surface friction heterodyned with the spec-

Table 4.5: Statistical property of ultimate compressive strength per series and group

	Specimen	Group	Mean Value μ		Standard Deviation σ		P-Value[1]	Series Δ[2]
			psi	MPa	psi	MPa	-	%
1	Tall Cylinder	Control	6765	46.64	342	2.36	< 0.001	15.4
		Test	5721	39.44	332	2.29		
2	Small Cylinder	Control	6691	46.13	341	2.35	< 0.001	31.5
		Test	4583	31.60	726	5.01		
3	Column	Control	5431	37.45	279	1.92	0.005	9.5
		Test	4915	33.89	473	3.26		
4	Cubes	Control	6882	47.45	937	6.46	0.005	14.3
		Test	5896	40.65	368	2.54		

[1] Determined by 1-tailed, two-sample unequal variance (heteroscedastic) t-test
[2] Assuming 100 % in control group, $\frac{\text{Control}-\text{Test}}{\text{Test}} 100\%$

imen shape. Analytically, the 4×2 factorial ANOVA showed an interaction effect between series (shape) and group (surface treatment) with $F(3,72) = 8.285$, $p < 0.001$, denoting that lower surface friction impacts the ultimate strength results differently depending on the analyzed shape; the series Δ in Figure 4.2 generalizes this finding for the mean values.

The statistical significance of the difference in strength reduction per specimen shape was evaluated using contrasts, resulting in the surface-shape interaction matrix shown in Table 4.6. Evidently, series 2 is the only one that is reciprocatively different, verifying that surface friction impacts series 1, 3, and 4 similarly as suggested by the sloped trend lines in Figure 4.3.

In summary, the measured strength results showed that concrete samples under reduced surface friction collapse at lower compressive stresses than con-

Table 4.6: Surface-shape interaction matrix (P–Values)

Surface in	Series 1	Series 2	Series 3	Series 4
Series 1		0.002	n.s.	n.s.
Series 2			$\leqslant 0.001$	$\leqslant 0.001$
Series 3	Sym.			n.s.
Series 4				

n.s. = not significant

crete specimens tested with conventional friction — a trend that was statistically confirmed for all four evaluated shapes. However, surface friction at the compression interface impacts the apparent strength measurement differently, depending on the sample shape.

4.4 Strain Measurements

To evaluate the strain behavior of concrete under increasing and sustained loading, 6 in. × 12 in. (152 mm × 305 mm) cylindrical specimens (Series 1) were tested, under conventional and reduced friction, with 2.2-in.-long (60 mm) strain gauges that were adhered to the concrete surface at mid-height. Measurements were taken in longitudinal (compressive strain) and transverse (tensile strain) directions, and all gauges were arranged in pairs, separated by 180°. The reported strain measurements represent the calculated mean values of two corresponding strain gauge readings.

The compressive stress was increased at a stress rate of 35 psi/s ± 7 psi/s (0.25 MPa/s ± 0.05 MPa/s) and held constant after reaching 90 % of the average 6 in. × 12 in. (152 mm × 305 mm) cylinder strength, as measured previ-

ously under the corresponding friction scenario. Accounting for the significantly different strength performance of series 1 specimens tested under conventional and reduced friction (15.4 %, as reported in Table 4.5), the intensity of the sustained stress for the control and test groups amounted to 6090 psi (42.0 MPa) and 5150 psi (35.5 MPa), respectively.

4.4.1 Conventional Surface Friction

For concrete cylinders tested with conventional compression plates, the uniaxial compressive stress is graphed with respect to the average longitudinal (compressive) strain in Figure 4.4. The five tested specimens showed repeat-

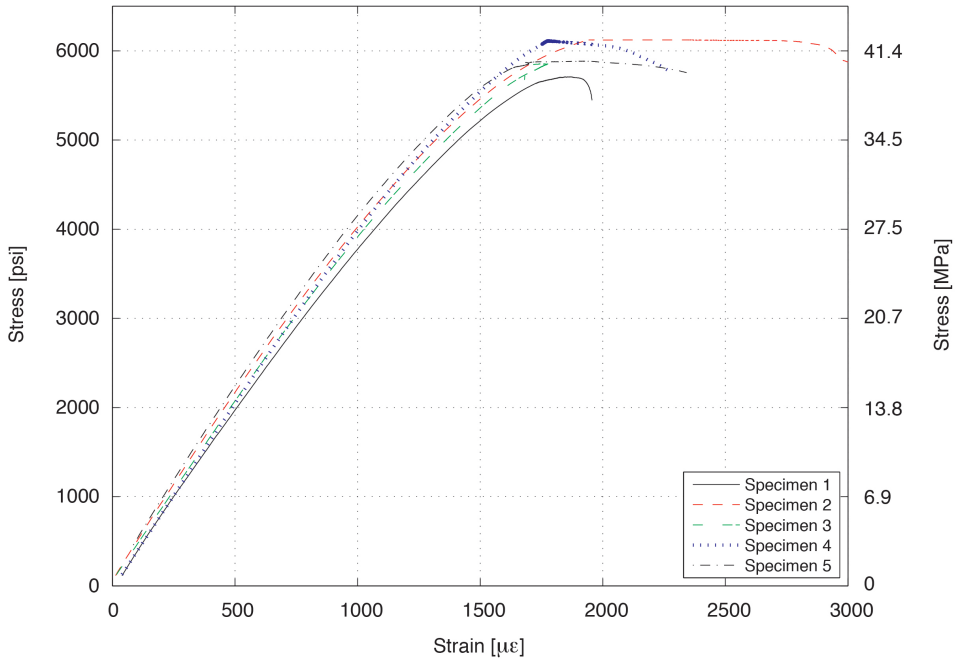

Figure 4.4: Relationship between compressive stress and longitudinal strain under conventional friction (load sustained at 90% of the measured control group strength)

able strain behavior, rendering almost identical stiffness values. The experi-

mentally determined MOE according to ASTM-International (2002c) amounts to approximately 4000 ksi (27.5 GPa) for all specimens, being more elastic than 4680 ksi (32.2 GPa) as predicted by the ultimate strength based formula provided in ACI 318 8.5.1 (American Concrete Institute, 2011a). The stress-strain response deviated from linearity around 3500 psi (24.1 MPa) or at 800 $\mu\epsilon$, and the strain rate (change in slope) increased drastically in the vicinity of 5000 psi (34.4 MPa), corresponding to 1300 $\mu\epsilon$. It is noted that specimens 1 and 3 failed before or right at the target sustained stress level. Nevertheless, for the samples that did not fail prematurely, the stress-strain curve plateaued after reaching the sustained stress, and the compressive strain kept growing while the stress remained constant. Failure strains under sustained loading ranged between 2100 $\mu\epsilon$ and 2900 $\mu\epsilon$.

Figure 4.5 plots the transverse (tensile) strain corresponding to the uniaxial compressive stress. The proportional limit was reached around 150 $\mu\epsilon$, corresponding to approximately 3500 psi (24.1 MPa) as seen previously in Figure 4.4. The strain rate (slope) increased rapidly at approximately 300 $\mu\epsilon$ or around 5000 psi (34.4 MPa); the strain continued to increase beyond the 1000 $\mu\epsilon$ that was reached at the peak sustained stress.

4.4.2 Reduced Surface Friction

The compressive strain performance of concrete specimens tested with reduced friction at the compression interface is illustrated in Figure 4.6. The evaluated specimens showed comparable stress-strain responses throughout all loading stages, and the experimentally determined MOE according to ASTM-International (2002c) appears identical for all test samples, with values ranging

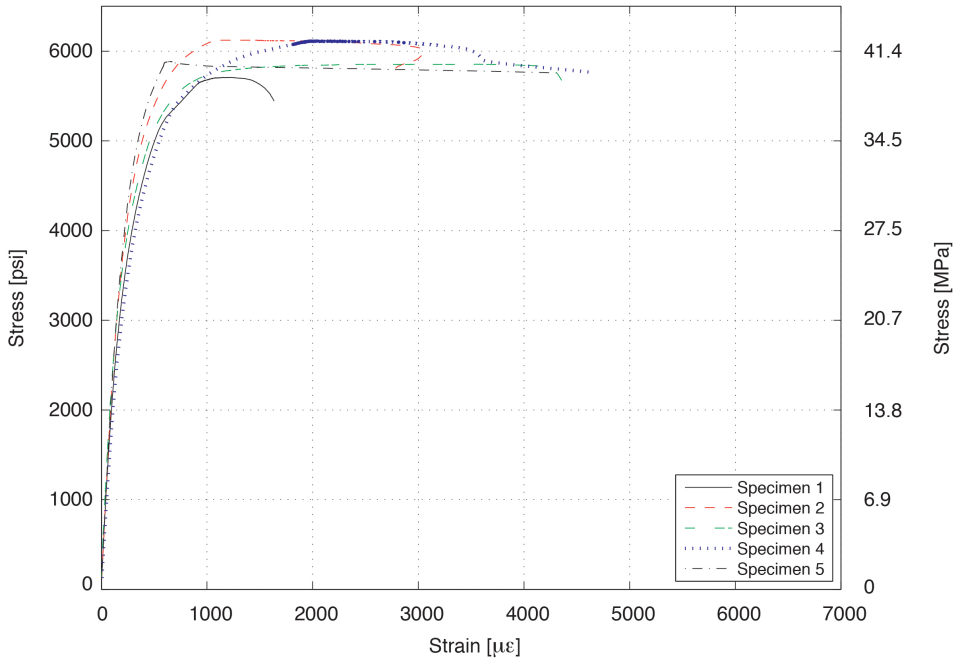

Figure 4.5: Relationship between compressive stress and transverse strain under conventional friction (load sustained at 90% of the measured control group strength)

around 4000 ksi (27.5 GPa) — ACI 318 8.5.1 (American Concrete Institute, 2011a) predicts an MOE of 4310 ksi (29.7 GPa) for theses specimens, if the average ultimate strength value of the test group samples is utilized. Linearity was maintained up to 800 με or 3500 psi (24.1 MPa), which is practically identical to the specimens tested with conventional friction. However, no specimen in Figure 4.6 showed a drastic strain rate (change in slope) increase while the compressive stress continued to ascend. All specimens reached the sustained stress level[1], and the longitudinal compressive strain kept growing although the compressive stress remained constant. The failure strain ranged between 2000 με and 3000 με.

The transverse tensile strain behavior under uniaxial compressive stress

[1] A user error occurred while programming the target sustained load for Specimen 2.

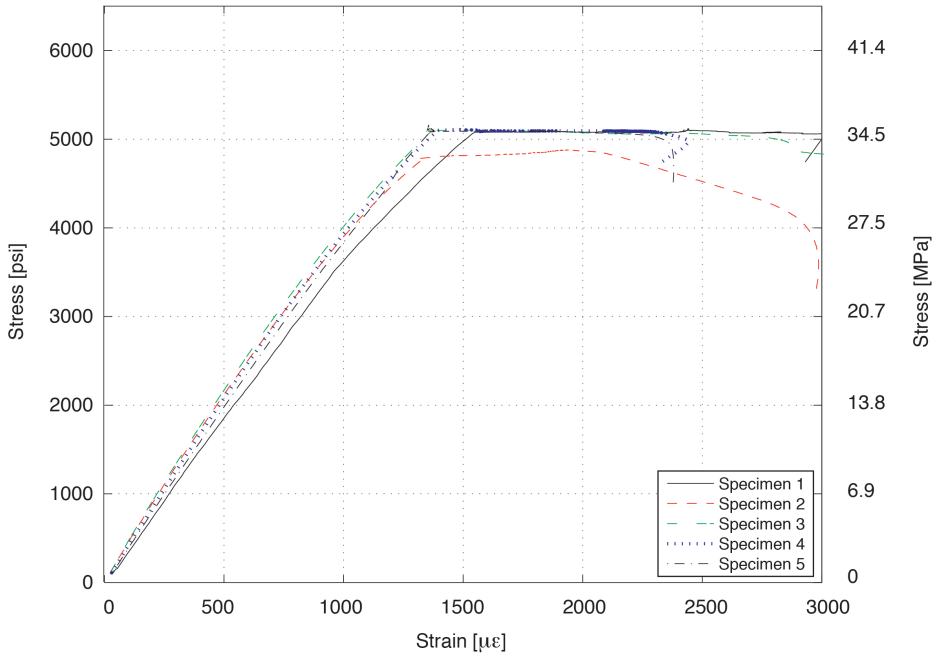

Figure 4.6: Relationship between compressive stress and longitudinal strain under reduced friction (load sustained at 90% of the measured test group strength)

is graphed in Figure 4.7. Similar to Figure 4.6, the proportional limit was reached at 3500 psi (24.1 MPa), which equates to a tensile strain of approximately 150 με. Afterwards, the strain rate increased (but no drastic strain rate (slope) change occurred under reduced friction as previously seen (under conventional friction) in Figure 4.5) until the sustained stress level was reached between 300 με and 400 με. The stress-strain curve plateaued thereafter, and the "apparent" failure strain was around 6000 με.

4.5 Failure and Fracture

General fracture patterns of typical concrete specimens are described in ASTM C 39 (ASTM-International, 2004b) and AASHTO T 22 (American Association of State Highway and Transportation Officials, 2006); although the two guide-

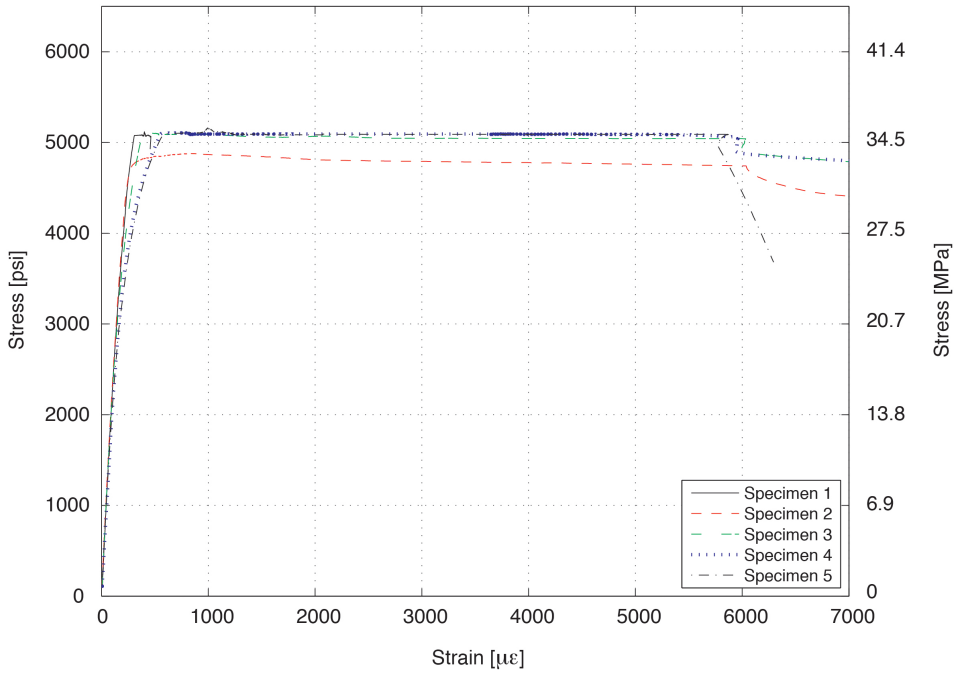

Figure 4.7: Relationship between compressive stress and transverse strain under reduced friction (load sustained at 90% of the measured test group strength)

lines are in agreement with each other, their described fracture types differ slightly. ASTM C 39 (ASTM-International, 2004b) provides a more rigorous description and, therefore, is used to characterize the final fracture patterns of the collapsed specimens in this research (Figure 4.8).

4.5.1 Conventional Surface Friction

All failure patterns in the control group (conventional surface friction) specimens compared well to each other with cone shaped failure patterns and preserved top and bottom surfaces — at least one surface was completely preserved. Figure 4.9 is representative of the final fracture pattern of concrete cylinders under regular friction; although 6 in. × 12 in. (152 mm × 305 mm) samples are depicted, the failure shape was found to be typical for all test

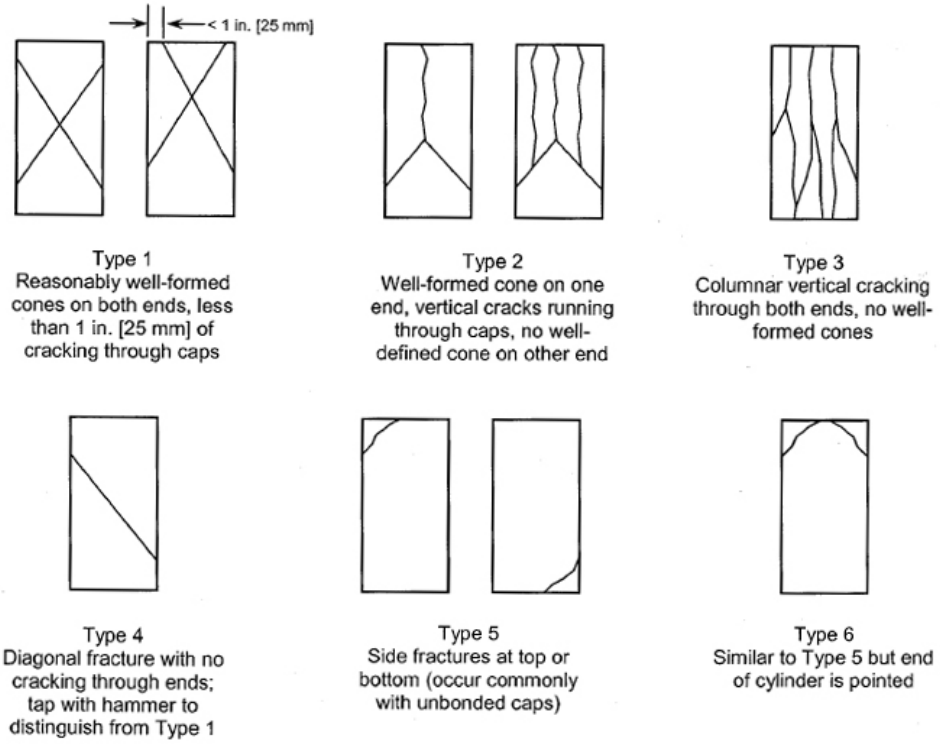

Figure 4.8: Schematic of typical fracture patterns (ASTM-International, 2004b)

(a) Cone on top end (b) Cone on both ends (c) Preserved surface

Figure 4.9: Fracture pattern of control group cylinders (conventional friction)

group specimens in series 1 and 2. Similarly, concrete cubes and columns (series 3 and 4) under regular friction preserved their compression surface almost entirely — in most cases on both ends. The typical final failure pattern of prismatic specimens is exemplified by the photographs in Figure 4.10 showing characteristics similar to cylindrical specimens tested under equal conditions.

(a) Cone on both ends (b) Cone (square) on top end

Figure 4.10: Fracture pattern of control group cubes (conventional friction)

According to ASTM C 39 (ASTM-International, 2004b), the observed fracture patterns for cylindrical and prismatic specimens can be classified as Type 1 or Type 2 failure, since one end (e.g., Figures 4.10(a) and 4.9(b)) or both ends (e.g., Figures 4.10(b) and 4.9(a)) showed reasonably well-formed cones.

The cracked facets appeared dusty for all control group specimens, especially in regions where the cones were formed. A discussion about the significance of dusty failure planes is presented in Section 6.5.

4.5.2 Reduced Surface Friction

Considerably different fracture patterns were observed for the test group specimens. Independent of the sample shape, all concrete samples cracked parallel to the applied compression force, splitting each specimen apart throughout the entire length, leading to fracture cracks through the contact surfaces — no top or bottom surface was completely preserved. The cylindrical specimens typically fractured into two or three elements separated by 180° or 120°, respectively, as shown in Figure 4.11. Some cylinders showed spalling at the

(a) Crack parallel to cylinder axis (b) Vertical cleavage (c) Small cone on top end

Figure 4.11: Fracture pattern of test group cylinders (reduced friction)

top end (Figure 4.11(a)), and others at the bottom end (Figure 4.11(b)). A few samples preserved a small portion of the compression surface at the inner core, forming cones with heights less than one quarter of the cylinder length (Figure 4.11(c)).

As shown in Figures 4.12 and 4.13, prismatic specimens tested under reduced friction showed similar fracture patterns with vertical cracks throughout the entire length/height of the specimens but without the preservation of core components. The columns in test series 3 mostly cracked into two or four ma-

(a) Axial cleavage (b) Dual vertical cracks

Figure 4.12: Fracture pattern of test group columns (reduced friction)

jor pieces, either separated by 180° or 90° similar to Figure 4.12(a). However, some columns formed dual or multiple cracks similar to the fracture pattern shown in Figure 4.12(b). Figure 4.13 verifies analogous fracturing for cube shaped specimens under reduced friction. Multiple vertical cracks throughout the entire height of the cubes can be considered the standard fracture pattern (Figure 4.13(a)), as no cube failed under a single crack or by separation into two pieces. All compression surfaces (top and bottom) were found to be

(a) Vertical cracks (b) Cracked top surface

Figure 4.13: Fracture pattern of test group cubes (reduced friction)

randomly cracked as indicated by Figure 4.13(b).

No dust was discovered on the failure planes of any test group sample, and all cracked concrete facets appeared clean and shiny; the specimens were split into clean shards. Section 6.5 elaborates on the significance of clean concrete surfaces.

4.5.3 Summary of Fracture Results

The final fracture patterns of the collapsed concrete specimens showed comparable failure patterns within each of the two groups. Regardless of the four diverse sample shapes, all specimens in the control group reliably rendered Type 1 or Type 2 failure patterns (ASTM-International, 2004b), preserving one or both compression surfaces completely. Independent of the specimen shape, all control group specimens showed dusty failure facets, especially at the end regions where the cones were formed. All specimens tested

with reduced surface friction, on the other hand, showed Type 3 failure patterns (ASTM-International, 2004b) with vertical cracks throughout the entire specimen height. The cracked concrete facets were free of dust, and appeared clean and shiny.

4.6 Crack Propagation and Rupture

To document the propagation of macrocracks before and at rupture, high-speed video technology as detailed in Section 3.10 was used to capture 2,000 fps. Example frames of these recordings are illustrated in Figures 4.14 through 4.19 for series 1 & 2, 3, and 4. The six frames in each figure represent the general behavior of each group and series, respectively, showing the development of rupture cracks for cylindrical and prismatic concrete samples at the time of failure. The images surrounded by a gray border denote the failure frames based on the measured 5-kip (22 kN) load drop criterion that was precisely defined in Sections 3.9 through 3.11.

Although the videos revealed consistent cracking behavior within each group, the following observations are based on a distinct vantage point, captured by a single camera without any irrefutable knowledge about the backside of the specimens. This is emphasized particularly for prismatic specimens, as only one surface could be recorded.

4.6.1 Conventional Surface Friction

The generally observed crack propagation in cylinders (series 1 and 2) tested with standard end conditions is illustrated in Figure 4.14. According to Figures 4.14(a) and 4.14(b), macrocracking began in the middle of the cylinder.

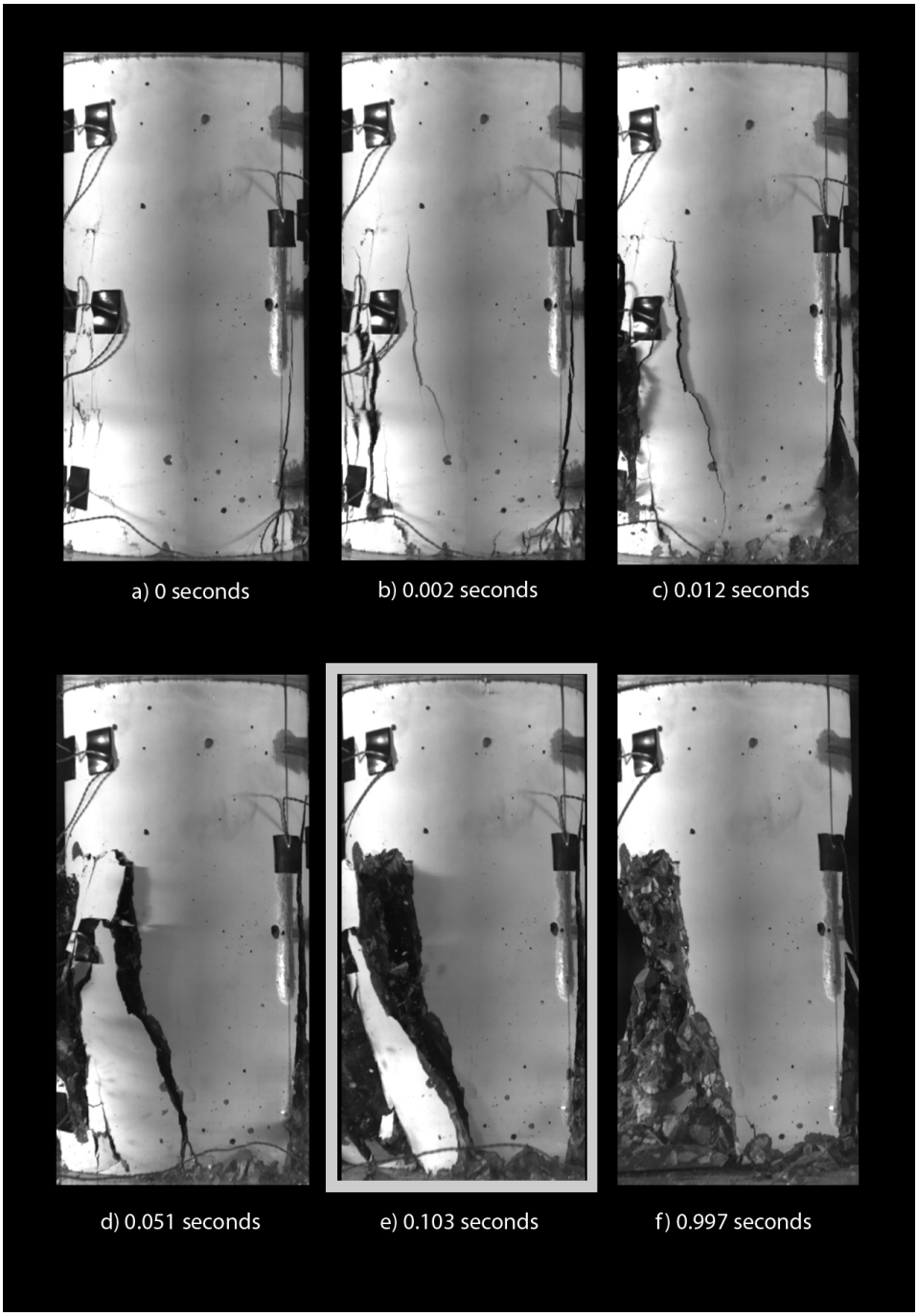

Figure 4.14: Cylinder failure under regular friction

It then propagated downward and dilated throughout Figure 4.14(b) to Figure 4.14(d). In the later frame, Figure 4.14(e), the spalled concrete pieces

abraded the remaining concrete structure, which in Figure 4.14(f) consisted of a well-formed cone at the bottom of the cylinder. The cylinder collapsed after Figure 4.14(d), about 0.1 s after the first cracks appeared on the cylinder's surface.

Figure 4.15 depicts the cracking for control group specimens in series 3. Figure 4.15(a) shows a vertical crack in the middle of the column, that was found in 9 out of 10 specimens in the control group recordings, and in this particular case existed 2.5 s before failure. In Figure 4.15(b), this crack eluded its vertical path and developed towards the lower right corner at 30° to the direction of the applied load. This crack widened in Figure 4.15(c), before a second inclined crack developed that ran towards the lower left corner as seen in Figure 4.15(d). Finally, as the bottom cone-shaped element and the remaining inverted funnel-shaped segment at the top pushed against each other, splitting occurred to separate the top section at its weakest point, causing failure according to Figure 4.15(e). The final fracture pattern, as it was observed after testing, is shown in Figure 4.15(f) with a pyramid core that preserved its bottom surfaces.

The development of failure cracks for the control group specimens in series 4 is portrayed by the high-speed video frames in Figure 4.16. In the cube under regular friction, cracking initiated from the top left corner according to Figure 4.16(a); from there it propagated to the center as illustrated in Figures 4.16(b) and 4.16(c). The applied compression force combined with surface friction hindered further crack distribution, and local buckling occurred in the upper third on the left side of Figure 4.16(d). This happened in multiple places and finally caused failure in Figure 4.16(e). The resulting fracture pattern in Figure 4.16(f) shows that the outer portion of the sample spalled off with a

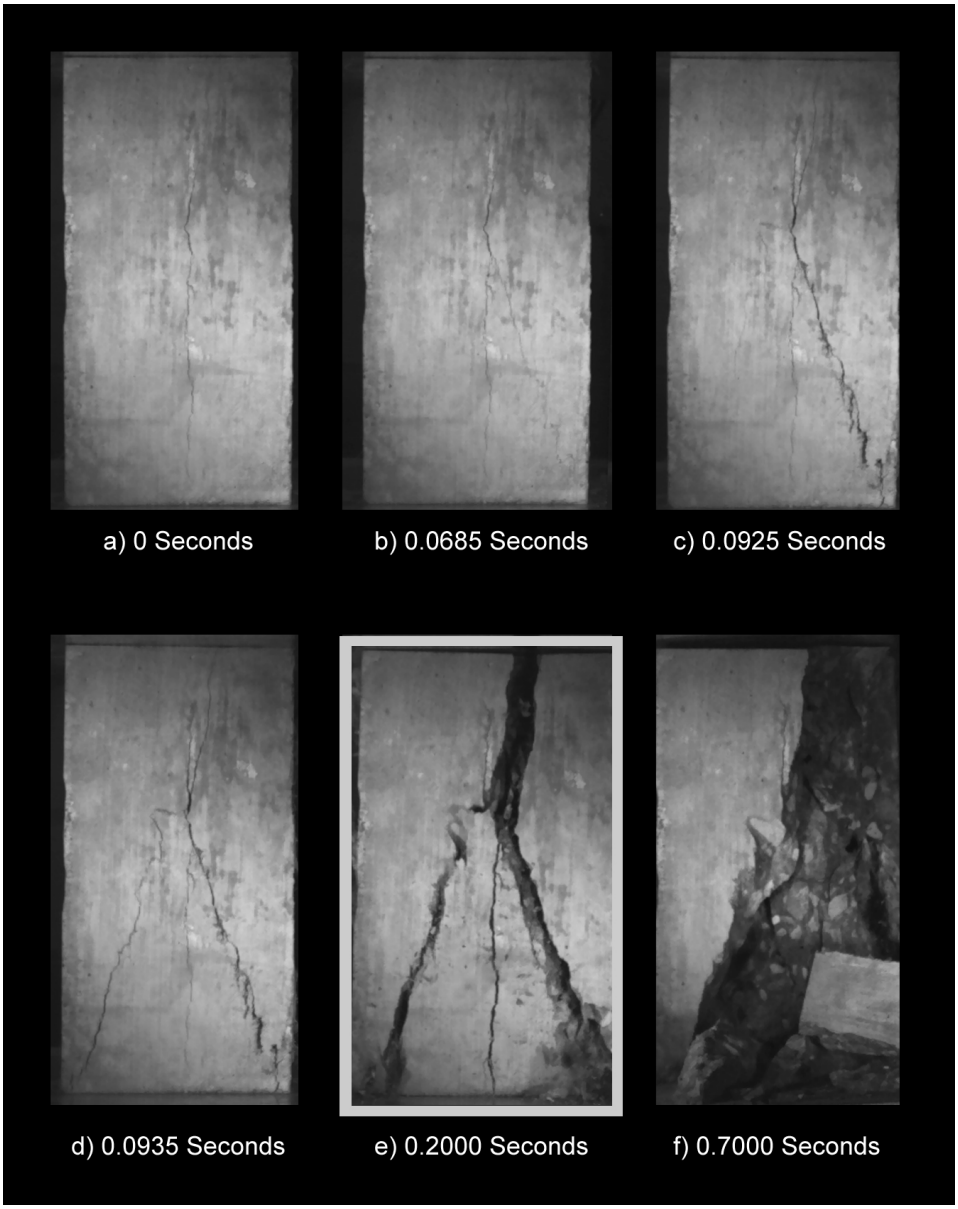

Figure 4.15: Column failure under regular friction

preserved top and bottom pyramid remaining at the specimen's core.

4.6.2 Reduced Surface Friction

The six frames of Figure 4.17 describe the general failure pattern that was recorded for cylinders tested with reduced surface friction. In Figure 4.17(a),

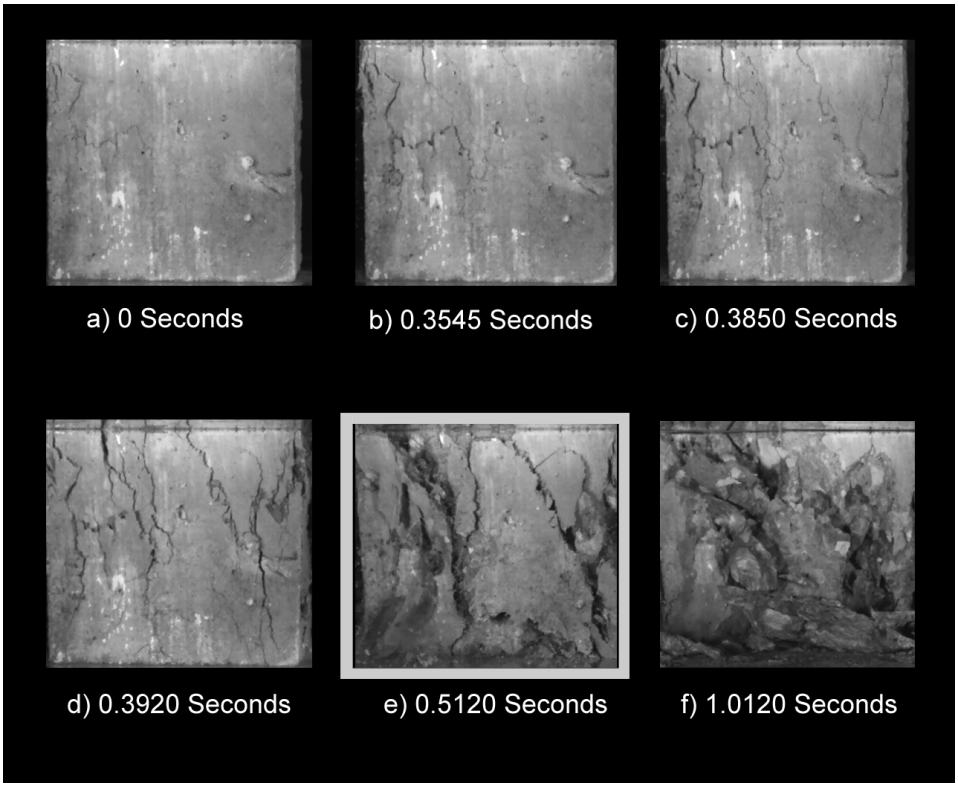

Figure 4.16: Cube failure under regular friction

cracking was initiated from the top region of the cylinder and propagated downwards (Figure 4.17(b) through Figure 4.17(c)) until it reached the bottom in Figure 4.17(d) and separated the cylinder into clean concrete shards in Figure 4.17(e). Afterwards, the specimen collapsed; in Figure 4.17(f), the cleavage fracture was widened and the shards dispersed. Consequently, the load drop criterion did not occur until 1.007 s after the first cracks became visible.

Under low surface friction, the columnar specimens showed the fracture behavior illustrated in Figure 4.18. No column showed vertical cracks prior to the video recordings; consequently, the first visual crack in Figure 4.18(a) was observed 0.059 s seconds before failure. This crack initiated in the lower third — close to the contact surface — and quickly propagated upwards within 0.01 s

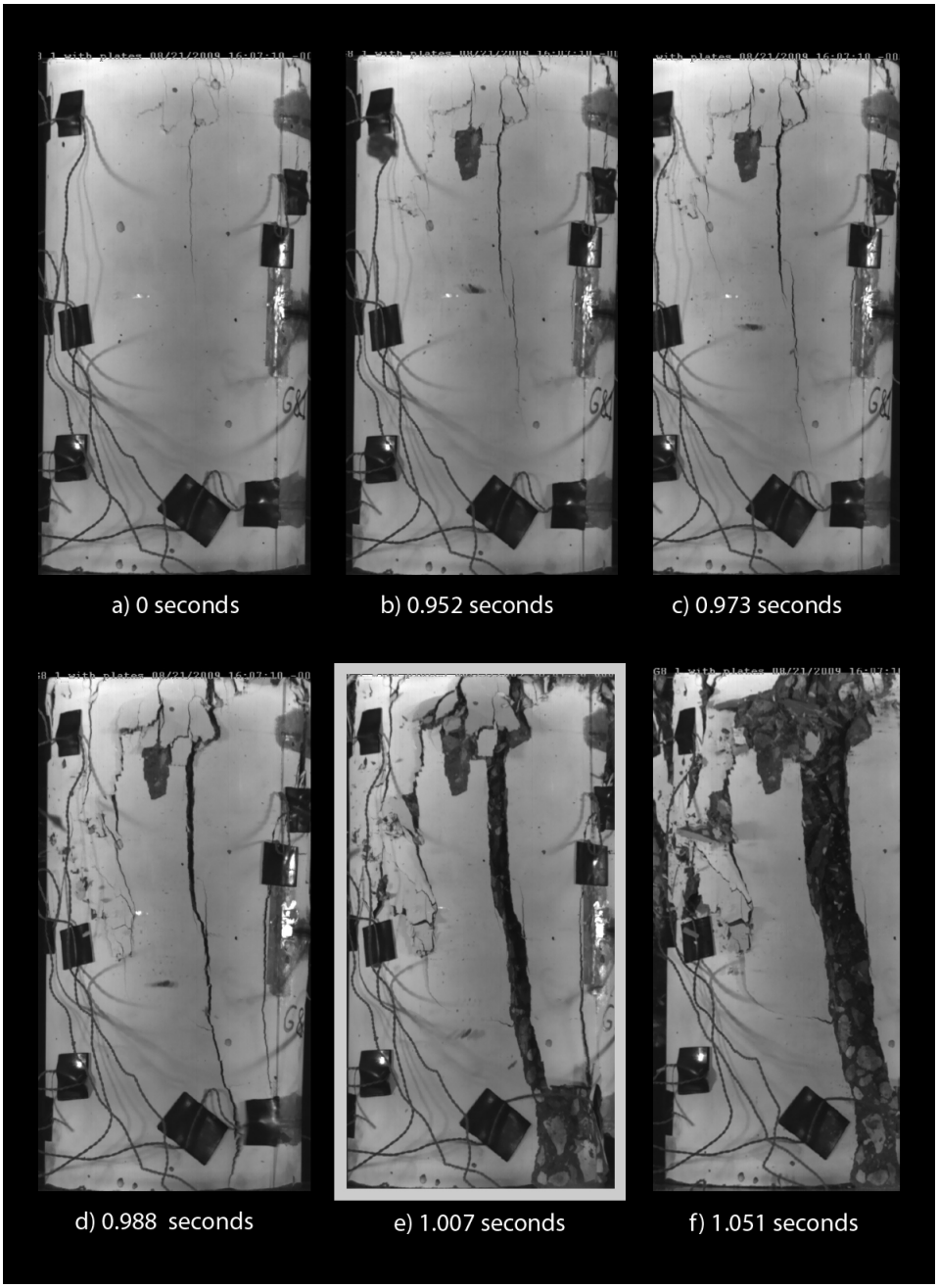

Figure 4.17: Cylinder failure under low friction

(Figure 4.18(b)). One frame later (0.0005 s), in Figure 4.18(c), the crack on the lower left side was observed with a length of approximately 7 in. (178 mm), suggesting that rupture cracks can propagate through concrete at (or faster

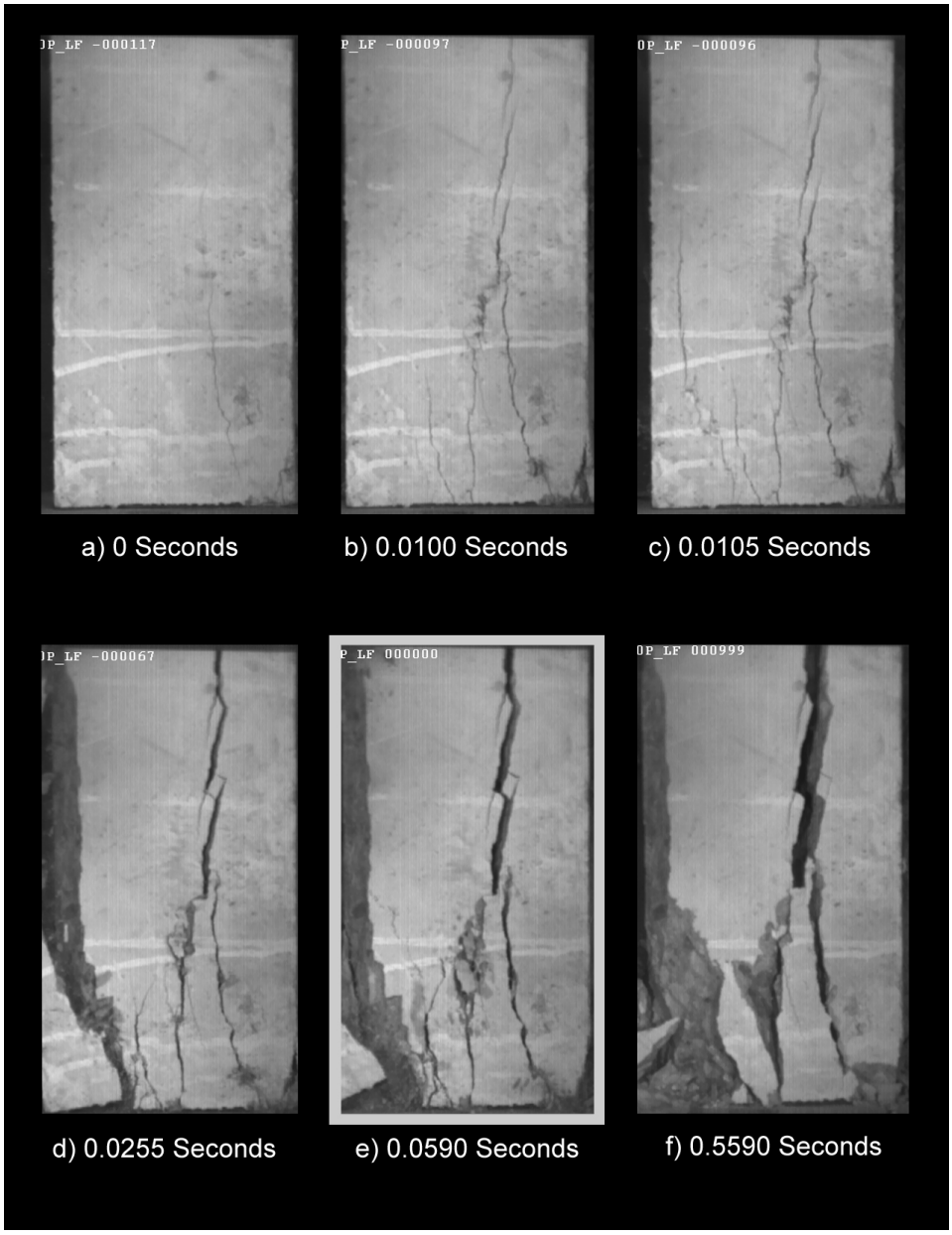

Figure 4.18: Column failure under low friction

than) the speed of sound. However, the earlier developed crack at the center expanded in Figure 4.18(d), but the specimen at this point still resisted an increase in force (in spite of the cross section reduction at the left). The specimen cleaved further in Figure 4.18(e) causing the 5-kip (22 kN) load drop

and the final fracture pattern in Figure 4.18(f).

The observed test group crack propagation for concrete cubes tested with reduced end confinement is generalized by Figure 4.19. For the depicted ex-

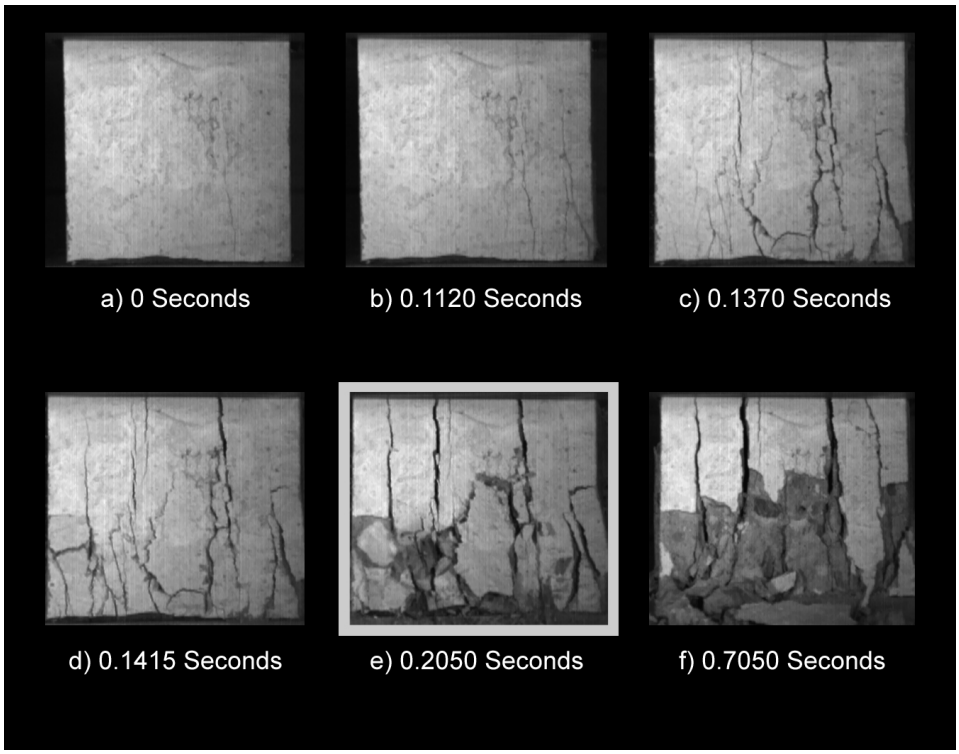

Figure 4.19: Cube failure under low friction

ample, rupture cracks initiated from the lower right corner, as seen in Figure 4.19(a), and moved vertically upwards in Figure 4.19(b). After the first major crack widened enough to separate the specimen, further vertical cracks started to grow as seen in Figure 4.19(c). At this point, the specimen was divided into parallel shards that corporate (providing the same cross section as the complete specimen) to resist the applied compression force. For ultimate rupture, buckling was initiated in Figure 4.19(d) causing failure according to Figure 4.19(e) and the final fracture pattern as shown in Figure 4.19(f).

4.6.3 Summary of Rupture Results

The rupture process of concrete specimens was observed to vary depending on the surface friction at the compression interface, irrespective of the evaluated sample shapes. While the specimens tested with conventional friction initiated cracking from mid-height and propagated at an angle (depending on the specimen height) towards the compression ends, the test group samples showed first cracks anywhere throughout the specimens (even at the extremes) and propagated vertically — along the applied compression force.

CHAPTER 5

ANALYSIS

5.1 Introduction

The preceding chapter showed clear differences between conventionally tested concrete samples and those tested under reduced friction. Depending on the confinement level, different failure loads and varying crack patterns occurred. The objective of this chapter is to reflect such behavior mathematically and to analytically explain the measured test results.

A generalized three-dimensional stress state for the uniaxial compression test is reviewed first and then is analyzed for varying boundary conditions (surface friction). The analysis is then extended to encompass the more rigorous strain behavior in three dimensions. Finally, the observed local buckling of concrete shards is discussed.

All mathematical procedures outlined in this chapter have been numerically and analytically evaluated using data processing software. The developed algorithms as well as the codes generated for proper visualization of data trends were written in MatLab[1] and are documented in Appendix A.

[1]MATLAB version 7.13.0.564 (R2011b), Natick, MA: The MathWorks Inc., 2011.

5.2 Stress Analysis

The stress state that arises from a uniaxial compression test with conventional surface friction (Figure 3.1) can be represented by the traction vectors acting on the infinitesimal rectangular parallelepiped ($dx\,dy\,dz$) in Figure 5.1. Be-

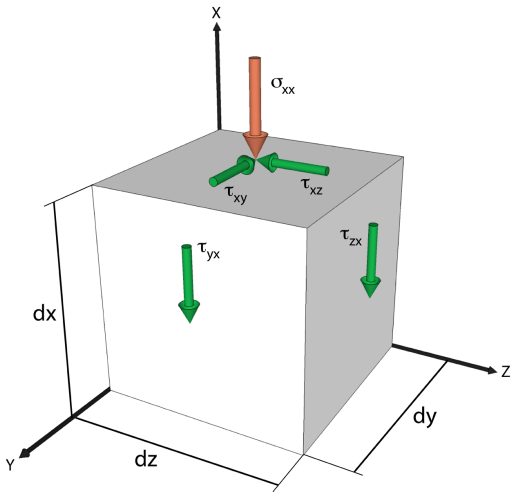

Figure 5.1: Normal and shear stresses in uniaxial compression tests with surface friction

cause surface friction produces end confinement, the specimen expansion (due to Poisson's ratio) at the compression interface is restrained, and shear stresses (τ_{xy} and τ_{xz}) are developed at the contact surfaces (x-surface). For rotational equilibrium, those shear stresses have to be balanced by the shear stresses (τ_{yx} and τ_{zx}) on the mutually perpendicular surfaces (y- and z-surface) — see da Silva (2006) for more details.

The boundary conditions can be written in matrix form and represented by the second order stress tensor (Sadd, 2004), that then generalizes the stress

state for a uniaxial compression test:

$$\sigma_{ij} = \begin{bmatrix} -\sigma_{xx} & -\tau_{xy} & -\tau_{xz} \\ -\tau_{yx} & 0 & 0 \\ -\tau_{zx} & 0 & 0 \end{bmatrix} \tag{5.1}$$

The shear stresses with shared indices must be identical (e.g., $\tau_{xy} = \tau_{yx}$) because they are equally distanced from the center of the infinitesimal small material element ($dx\,dy\,dz$), reducing the stress tensor in Expression 5.1 to a function of three variables (σ_{xx}, τ_{xy}, and τ_{xz}).

5.2.1 Principal Stress Values

To analyze the three dimensional stress state, σ_{ij}, for its principal stress magnitudes (λ), the eigenvalues of the stress tensor have to be determined according to Equation 5.2 (da Silva, 2006; Hosford, 2010).

$$det(\sigma_{ij} - I\lambda) = det \begin{vmatrix} -\sigma_{xx} - \lambda & -\tau_{xy} & -\tau_{xz} \\ -\tau_{xy} & -\lambda & 0 \\ -\tau_{xz} & 0 & -\lambda \end{vmatrix} = 0 \tag{5.2a}$$

Solving the determinant, using the rule of Sarrus, yields a cubic expression in terms of λ, that then represents the characteristic equation for the stress description of a uniaxial compression test:

$$0 = -\lambda^3 + (-\sigma_{xx})\lambda^2 + (\tau_{xy}^2 + \tau_{xz}^2)\lambda \tag{5.2b}$$

Rearranging Equation 5.2b shows that the first principal stress value (λ_1) must be equal to zero, which is expected, since the traction vectors (see Figure 5.1) are acting in two planes only (rotational symmetry).

$$0 = \lambda[-\lambda^2 + (-\sigma_{xx})\lambda + \tau_{xy}^2 + \tau_{xz}^2] \qquad \Rightarrow \lambda_1 = 0 \tag{5.2c}$$

Note that this statement ($\lambda_1 = 0$) must be true for any intensity of normal stresses or shear stresses. However, the remaining two principal stress values can be determined from the quadratic equation that remains inside the brackets of Expression 5.2c:

$$0 = -\lambda^2 + (-\sigma_{xx})\lambda + \tau_{xy}^2 + \tau_{xz}^2 \tag{5.3}$$

Solving Equation 5.3 for λ_2 and λ_3 returns the two remaining principal stress magnitudes.

$$\lambda_{2,3} = \frac{-\sigma_{xx}}{2} \pm \sqrt{\frac{{\sigma_{xx}}^2}{4} + {\tau_{xy}}^2 + {\tau_{xz}}^2} \tag{5.4}$$

For λ_2 and λ_3 to be physically meaningful, the solution of the square root has to be real. Because all terms under the square root in Expression 5.4 are squared and additive, they cannot take on negative values, and the solution to Equation 5.4 will always be real and physically relevant.

Assuming λ_2 to be the minimum (negative) outcome of Equation 5.4, it can be stated that a principal compressive stress ($\lambda_2 = \lambda_c$) is mandatory to exist regardless of the frictional restraint. This was expected as well, because the applied compression stress in a uniaxial test must not disappear (even under very high shear stresses). In fact, it is more critical to analyze λ_3 for its probability to be positive ($\lambda_3 = \lambda_t$), as this would cause principal tensile

stresses to arise, which are necessary to initiate concrete cracking.

It can be seen from Expression 5.4 that the first term under the square root ($\frac{{\sigma_{xx}}^2}{4}$) balances the negative term in front of the square root. It follows, then, that λ_t is equal to zero under the assumption of a frictionless compression interface. That is, in such a case only λ_t takes on a (negative) value, and a pure uniaxial compression state is generated. However, any frictional restraint (or shear stresses) at the compression interface results in positive values for λ_t and tensile stresses to arise.

The shear stresses are a result of the end confinement, which in turn depends on the surface friction. It is therefore appropriate to state that the two values τ_{xy} and τ_{xz} are a function of the interface media coefficient of friction, μ_1 and μ_2, and the normal stress, σ_{xx}, that operates on the compression surface. The principal stresses become:

$$\lambda_{2,3} = \lambda_{c,t} = \frac{-\sigma_{xx}}{2} \pm \sqrt{\left(\frac{\sigma_{xx}}{2}\right)^2 + (\mu_1 \sigma_{xx})^2 + (\mu_2 \sigma_{xx})^2} \tag{5.5a}$$

Rearranging Equation 5.5a, by factoring out the common term σ_{xx}, yields the principal stress values in their most simplistic form and as a function of the coefficient of surface friction:

$$\lambda_{2,3} = \lambda_{c,t} = \frac{-\sigma_{xx}}{2} \pm \sqrt{{\sigma_{xx}}^2 \left(\frac{1}{4} + {\mu_1}^2 + {\mu_2}^2\right)} \tag{5.5b}$$

In agreement with the physical interpretation, it can be seen that the relationship is linear in σ_{xx}. As the normal stress increases, the principal stress value increases proportionally. That is, its orientation remains constant (as long as the coefficient of friction remains constant). In addition, Equation 5.5b

depends on the surface friction in a nonlinear fashion. But because the expression is linear in σ_{xx}, it can be normalized for the uniaxial compressive stress and graphed as a function of the coefficient of friction, μ, at the compression interface, which is significant because the magnitude of λ ultimately determines the orientation/direction angles of the principal stress. Figure 5.2 illustrates Expression 5.5b for the condition $\mu_1 = \mu_2$, as this is the most applicable case for a conventional uniaxial compression test. It can be seen that

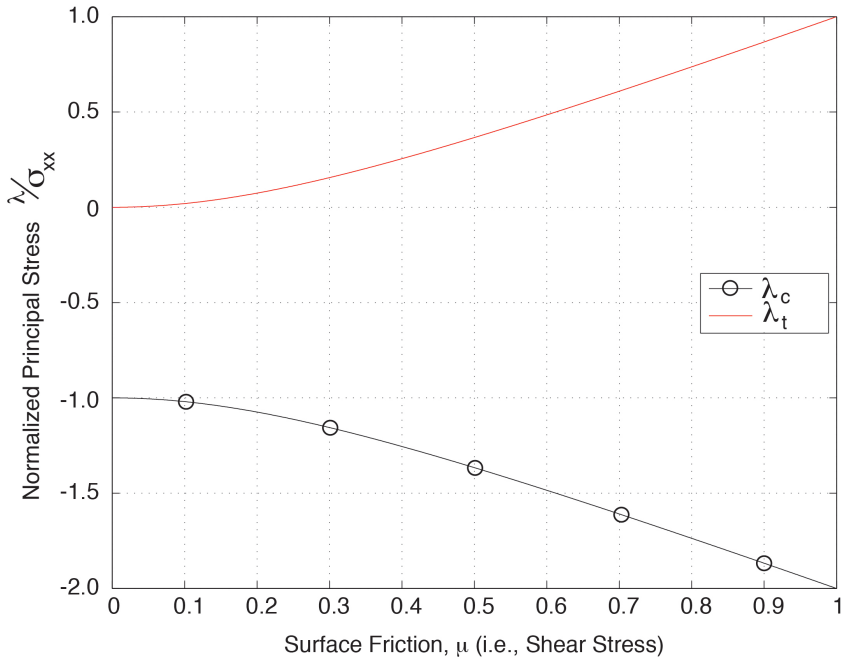

Figure 5.2: Principal stress magnitude λ_3 dependent on coefficient of surface friction μ

the magnitude of the principal tensile stress follows an ascending parabolic trend for increased surface friction, while the opposite is true for the intensity of the principal compressive stress. It is noted that the principal tensile stress λ_t takes on the same value as the uniaxial compressive stress, or σ_{xx}, for the

theoretical case of $\tau_{xy} = \tau_{xz} = \sigma_{xx}$ ($\mu = 1.0$).

5.2.2 Principal Stress Orientation

The orientation of the principal stresses is described by the eigenspace of the stress tensor, σ_{ij} (da Silva, 2006; Sadd, 2004). That is, the principal stress magnitude λ has to be subtracted from the diagonal terms (σ_{ii}) of the stress tensor, which then is multiplied by an unknown unit vector and equated to zero:

$$(\sigma_{ij} - \delta\lambda)\vec{n} = \begin{bmatrix} -\sigma_{xx} - \lambda & -\tau_{xy} & -\tau_{xz} \\ -\tau_{xy} & -\lambda & 0 \\ -\tau_{xz} & 0 & -\lambda \end{bmatrix} \begin{Bmatrix} n_x \\ n_y \\ n_z \end{Bmatrix} = 0 \qquad (5.6)$$

Solving Equation 5.6 for the unknown unit vector, $\vec{n}$, returns the eigenvector that corresponds to the principal stress magnitude (λ) — three principal stress magnitudes provide three eigenvectors. Because λ is a function of the surface friction, it can be concluded that the orientation of the principal stress in a uniaxial compression test is dependent on the surface friction as well. This is considered a good reflection of the different stress distributions and the observed varying crack orientations under changing end confinement, as presented in Chapter 4.

According to the literature (da Silva, 2006; Hosford, 2010; Sadd, 2004), the eigenvectors are usually returned in vector form or in terms of their components along the original reference frame ($\vec{n}$). But for visualization purposes and to relate the results to a uniaxial compression test, it is more beneficial to represent the principal stress directions according to their orientation in space. The principal stress state is then described by the three direction angles ac-

cording to Figure 5.3, with each angle relative to one of the reference axes. Those directional properties can be derived solely from the principal direction

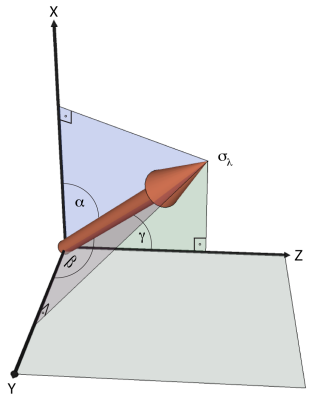

Figure 5.3: Principal direction angles α, β, and γ

vector as specified by Equation 5.7.

$$\cos\alpha = \frac{n_x}{|\vec{n}|} = n_x \qquad \cos\beta = \frac{n_y}{|\vec{n}|} = n_y \qquad \cos\gamma = \frac{n_z}{|\vec{n}|} = n_z \tag{5.7}$$

It follows that the directional cosines are a function of the unit vectors (principal stress vector) that describe the eigenspace of the stress tensor, and therefore depend on the end confinement as well. Accordingly, the directional angles can be graphed in terms of the surface friction. Figures 5.4 and 5.5 graph the three directional angles α, β, and γ (absolute values) in dependance of the frictional restraint. Figure 5.4 plots the surface friction vs. the directional angles of the principal compressive stress (λ_c), while the change of the directional angles due to alternating surface friction for the principal tensile stress (λ_t) is illustrated in Figure 5.5.

It can be seen in Figure 5.4 that the principal compression stress angle

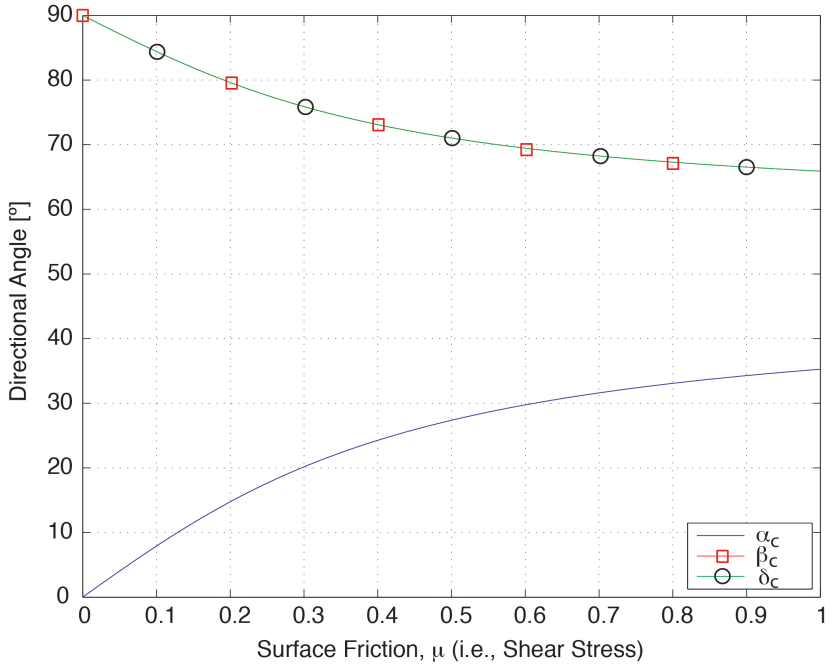

Figure 5.4: Directional angles for principal compressive stresses as a function of the shear stress

α_t increases for elevated shear stresses at the compression interface, signifying that the principal compression stress deviates from the vertical direction (x-axis) for increasing surface friction. Figure 5.5, on the other hand, illustrates that the principal tensile stress operates at an angle (α_t) of 90° to the x-axis (that is, horizontally) for the theoretically assumed case of zero shear stress and decays for increased end confinement until it converges towards 55° for increasing confinement.

Because both graphs plot the absolute directional angles, it follows that α_c in compression must be complementary to α_t in tension. Comparing Figure 5.4 to Figure 5.5, it can be seen that the summation of α_t and α_c yields 90° for any given frictional restraint, validating the derived equations and plots.

It is emphasized that the data points for β overlap the data points of

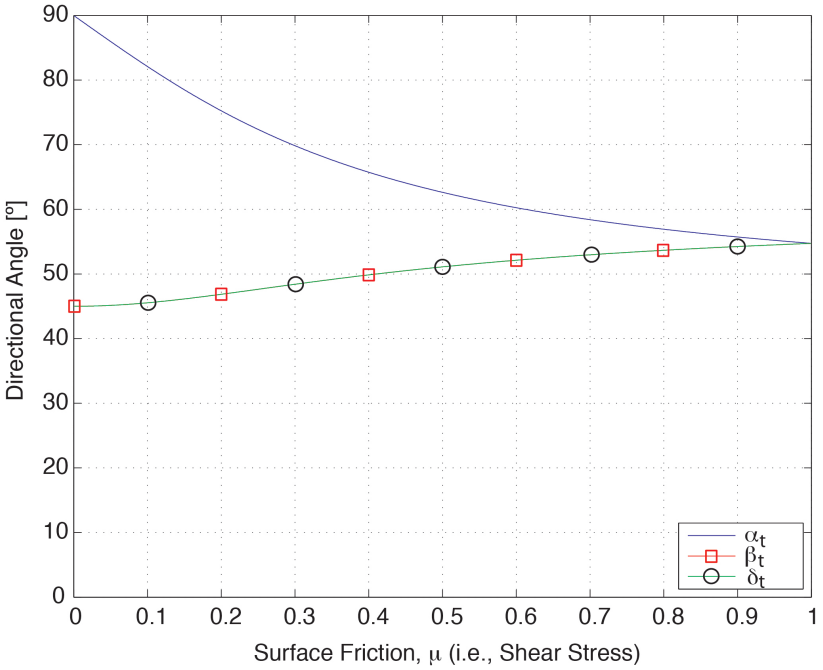

Figure 5.5: Directional angles for principal tensile stresses as a function of the shear stress

γ in both plots because the traction vectors in a uniaxial compression test operate in two planes only (here in the xy-plane and the xz-plane, without any components operating in the yz-plane). In other words, Figures 5.4 and 5.5 indicate rotational symmetry of α about the x-axis as would be expected in a uniaxial compression test along the vertical axis with equal confinement in the horizontal directions. It can be stated that an increase in frictional restraint causes the principal tensile stress angle α to flatten out in a nonlinear fashion (Equation 5.5b).

In general (da Silva, 2006; Sadd, 2004), an eigenspace (principal reference frame) is described by three mutually perpendicular unit vectors and is $[C][C]^T = [C]^T[C] = I$, where C is a matrix containing the three principal direction vectors. If the first principal stress magnitude, λ_1, is equal to zero,

all corresponding directional angles for λ_1 must be constant throughout any change in surface friction because all stresses are planar in λ_c and λ_t. Accordingly, the stress state in a uniaxial compression test is rotation-symmetric about the compression axis, and the principal compressive stress direction is mutually perpendicular to the principal tensile stress direction and an axis perpendicular to the rotational axis (here, any axis inside the yz–plane).

5.2.3 Interpretation of Stress Analysis

The principal compressive stress direction, α_c, in Figure 5.4 was shown to be vertical (along the x-axis) for zero surface friction and to diverge from the vertical axis as the confinement increases. Similarly, the orientation of the principal tensile stress, α_t, in Figure 5.5 grew towards the horizontal direction as the surface friction approached zero. The two graphs are considered to be in good agreement with the documented test results since the failure cracks occurred relatively parallel to the direction of the applied compressive force (x-axis) for all specimens in the test group (reduced surface friction), whereas the specimens tested with conventional end confinement showed cracks up to 30° relative to the vertical direction. However, to describe concrete rupture, Figure 5.2 appears problematic, as it fails to explain the failure phenomenon at zero friction — assuming that cracks are induced by tension. According to the graph, it seems impossible to fail a specimen under such boundary conditions because no tensile stresses are developed. Although test group experiments in this research did not produce true uniaxial test conditions (zero friction), the evaluated test setup is considered a close approximation according to the observed crack propagation and failure patterns, therefore

revealing the limitation of a stress-based failure analysis as highlighted by Figure 5.2. It must be concluded that a pure stress description is not sufficient to characterize concrete failure throughout the entire failure regime.

5.3 Strain Analysis

As mentioned before, any longitudinally strained concrete specimen tends to dilate laterally due to Poisson's effects (see Section 3.2). Such behavior can be considered a pure strain phenomenon because no lateral stresses are developed under perfect boundary conditions (zero friction). However, conventional testing with surface friction at the compression interfaces causes strain gradients throughout the specimen because lateral dilation is impeded at the specimen's extremes. The resulting strain behavior of typical specimens under uniaxial compression is accordingly visualized in Figure 5.6. The amount of confinement defines the preservation of the initial contact surface, while the Poisson's ratio — at any given longitudinal strain level because it is not constant (Hussein and Marzouk, 2000) — determines the lateral deformation. However, the generalized three-dimensional strain state at the compression interface can be modeled for an infinitesimal material element (detailed in Figure 5.6) according to Figure 5.7. The represented strain state differs in complexity from the previously discussed stress distribution because all lateral components, ϵ_{ii}, are now considered. Nevertheless, the boundary condition shown in Figure 5.7 can still be described by a second order tensor that now generalizes the three-

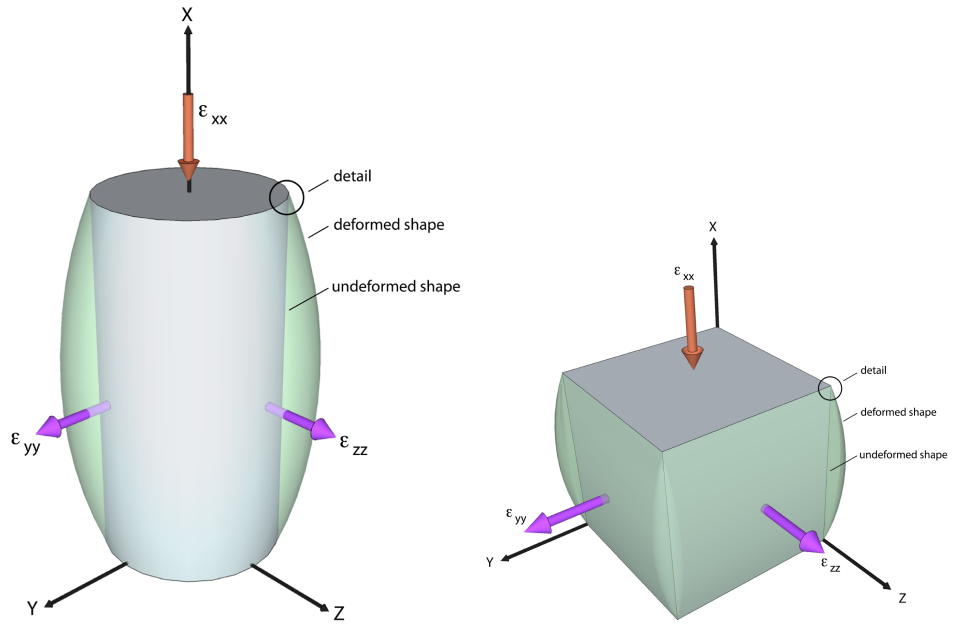

(a) Cylinder (b) Cube

Figure 5.6: Deformed and undeformed specimen shapes (global behavior)

dimensional strain situation.

$$\epsilon_{ij} = \begin{bmatrix} -\epsilon_{xx} & -\gamma_{xy} & -\gamma_{xz} \\ -\gamma_{yx} & \epsilon_{yy} & 0 \\ -\gamma_{zx} & 0 & \epsilon_{zz} \end{bmatrix} \tag{5.8}$$

Analogous to the stress tensor, the strain components with sheared indices need to be numerically equal (da Silva, 2006). In addition, the strain behavior at the contact surface is similar regardless of the direction ($\gamma_{xy} = \gamma_{xz}$). Therefore, Expression 5.8 describes ϵ_{ij} as a function of four variables (ϵ_{xx}, ϵ_{yy}, ϵ_{zz}, and γ), or three variables ($\epsilon_{yy} = \epsilon_{zz}$) for isotropic materials like concrete.

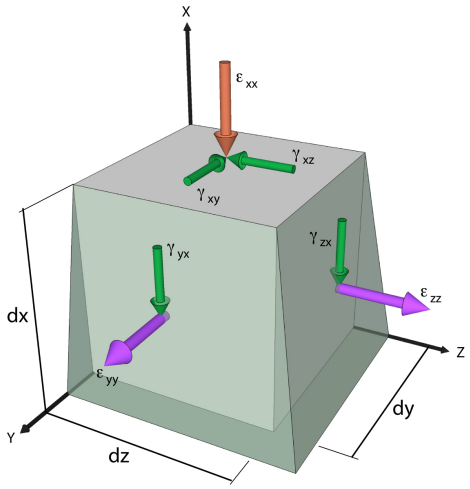

Figure 5.7: Normal and shear strains in uniaxial compression tests with surface friction

5.3.1 Principal Strain Values

The principal strain values are described by the eigenvalues of the strain tensor (da Silva, 2006) which are the determinant of the strain tensor after subtraction of λ along the diagonal terms, ϵ_{ii}, as shown in Equation 5.9.

$$det(\epsilon_{ij} - I\lambda) = det \begin{vmatrix} -\epsilon_{xx} - \lambda & -\gamma_{xy} & -\gamma_{xz} \\ -\gamma_{xy} & \epsilon_{yy} - \lambda & 0 \\ -\gamma_{xz} & 0 & \epsilon_{zz} - \lambda \end{vmatrix} = 0 \tag{5.9a}$$

The rule of Sarrus solves the determinant and provides the characteristic equation for the generalized strain situation, returning λ in form of a cubic equation according to Equation 5.9b.

$$\begin{aligned} 0 = &- \lambda^3 + (-\epsilon_{xx} + \epsilon_{yy} + \epsilon_{zz})\lambda^2 + (\epsilon_{xx}\epsilon_{yy} + \epsilon_{xx}\epsilon_{zz} - \epsilon_{yy}\epsilon_{zz} + \gamma_{xy}^2 + \gamma_{xz}^2)\lambda \\ &- (\epsilon_{xx}\epsilon_{yy}\epsilon_{zz} + \epsilon_{yy}{\gamma_{xz}}^2 + \epsilon_{zz}{\gamma_{xy}}^2) \end{aligned} \tag{5.9b}$$

It follows that the characteristic equation for the strain state (Equation 5.9b) is more convoluted than the characteristic equation that describes the stress state (Equation 5.2b), under equal test conditions. Because the lateral dilation components are a function of the axial deformation and are dependent on the Poisson's ratio, the expression can be reduced:

$$\begin{aligned} 0 = &- \lambda^3 - [\epsilon_{xx}(1-2\nu)]\lambda^2 + [{\epsilon_{xx}}^2(2\nu-\nu^2)+2\gamma^2]\lambda \\ &- [\epsilon_{xx}\nu({\epsilon_{xx}}^2\nu+2\gamma^2)] \end{aligned} \tag{5.9c}$$

Although simplified for normal strains, Equation 5.9c is rather complex due to the constant term $[\epsilon_{xx}\nu({\epsilon_{xx}}^2\nu+2\gamma^2)]$, which makes it nontrivial to factor out λ. Cardon's method can be used to put the equation into a depressed state but such analyses are beyond the scope of this text. However, Equation 5.9c can be numerically evaluated and analyzed for changing surface confinements by utilizing the shear strains, γ, as running variables — reflecting the deformational changes for material elements under different boundary conditions. The normalized results (relative to the axial strain, ϵ_{xx}) of that analysis are illustrated in Figure 5.8. The graphed strain behavior follows a trend similar to the stress curve in Figure 5.2, but with an offset at zero end confinement due to the Poisson's effect.

5.3.2 Principal Strain Orientation

The spacial directions of the principal strains are inherent to the strain tensor, ϵ_{ij}, similar to the principal stress orientation (da Silva, 2006; Sadd, 2004). However, because the diagonal of the tensor is now completely populated due to Poisson's effects, the eigenspace changes accordingly as seen in Equa-

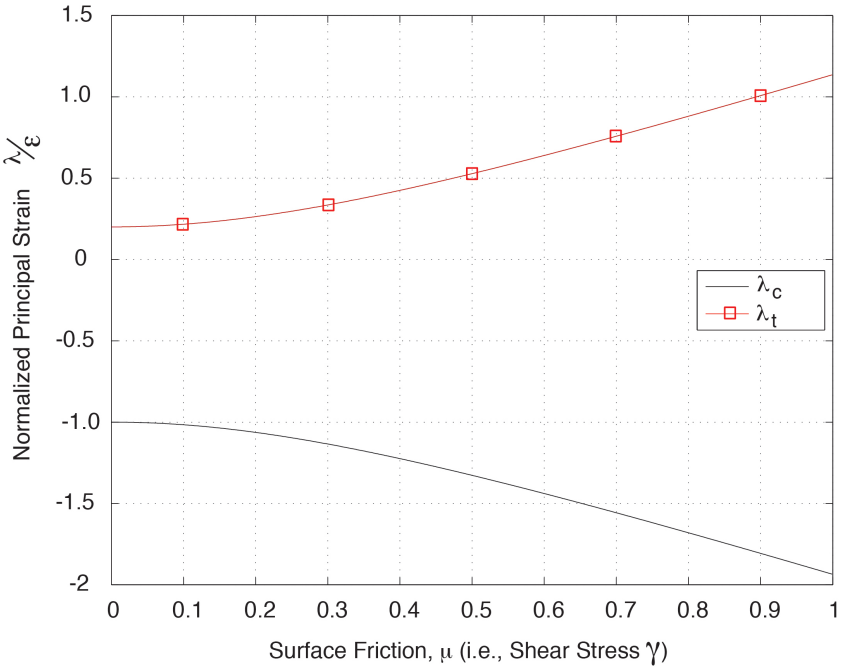

Figure 5.8: Principal strain magnitudes λ_2 and λ_3 dependent on coefficient of surface friction μ

tion 5.10.

$$(\epsilon_{ij} - \delta\lambda)\vec{n} = \begin{bmatrix} -\epsilon_{xx} - \lambda & -\tau_{xy} & -\tau_{xz} \\ -\tau_{xy} & \epsilon_{yy} - \lambda & 0 \\ -\tau_{xz} & 0 & \epsilon_{zz} - \lambda \end{bmatrix} \begin{Bmatrix} n_x \\ n_y \\ n_z \end{Bmatrix} = 0 \qquad (5.10)$$

In agreement with Figure 5.3 and Equation 5.7, each of the three eigenvectors that describe the principal strain state can be expressed by the three direction angles, α, β, and γ. The principal compression strain orientation can then be graphed for every increment of surface friction as shown in Figure 5.9. According to the plot, the principal compressive strain is oriented along the x-axis for zero surface confinement and increasingly diverges for increasing shear strains. Comparing Figure 5.9 to Figure 5.4, it can be seen that the two

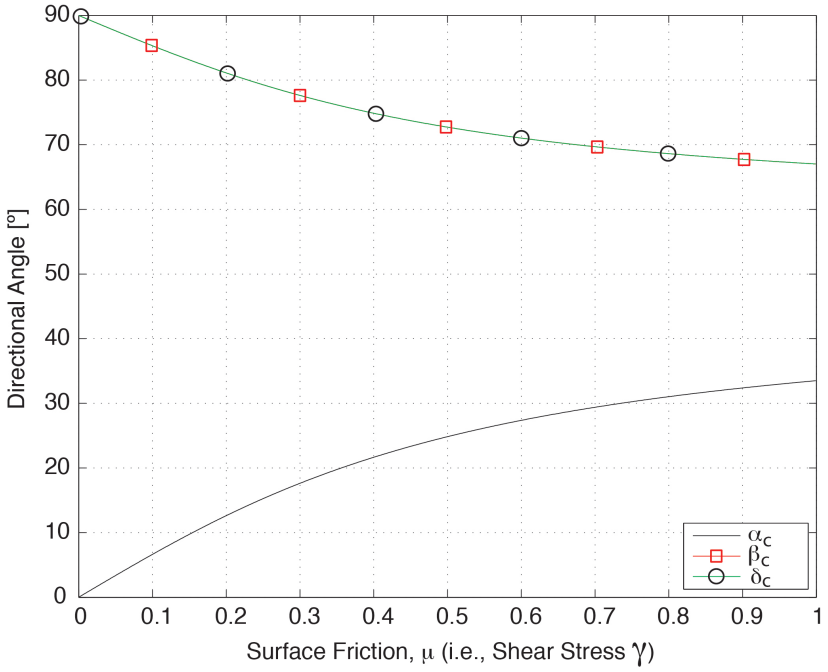

Figure 5.9: Directional angles for principal compressive strain as a function of the shear stress

graphs are similar but not identical — due to the addition of lateral dilation.

The direction of the principal tensile strain is illustrated in Figure 5.10 for increasing shear strains or surface friction. Accordingly, the principal tensile strain is oriented perpendicularly to the x-axis as long as no shear strains are present. With increasing shear strains, the principal tensile strain retracts from 90° and converges towards 58°. The graph compares well to Figure 5.5 but cannot be considered identical.

5.3.3 Interpretation of Strain Analysis

It was shown that the strain behavior in a uniaxial compression test differs from the stress distribution for identical boundary conditions. Due to intrinsic properties (i.e., Poisson's ratio), the material dilates laterally and experiences

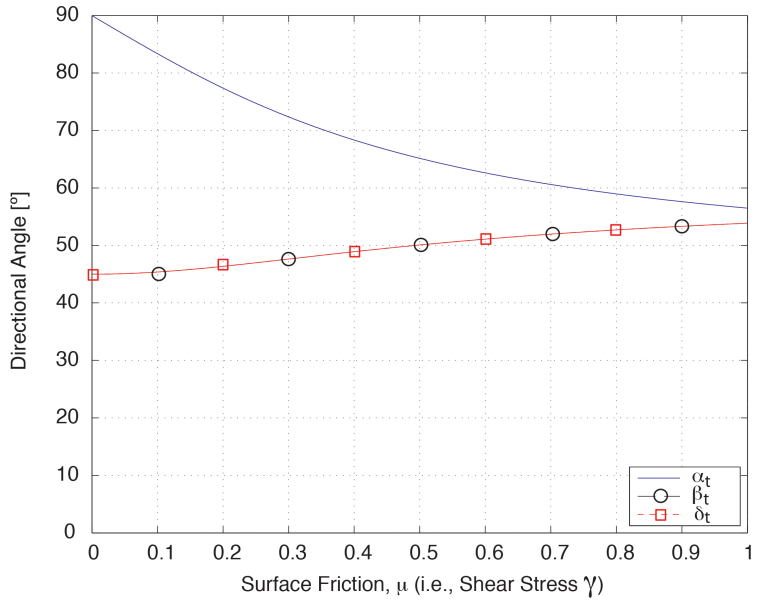

Figure 5.10: Directional angles for principal tensile strain as a function of the shear stress

tensile strains even under true uniaxial compression (zero friction). As the surface confinement increases, the tensile strains intensify and change their orientation. With cracks as a result of tensile strains, the strain analysis provides a sufficient characterization of the failure behavior throughout the entire failure regime.

Although the modeled strain behavior reflects the tensile strains properly, both stress and strain analyses fail to explain the strength difference due to altered surface friction. In fact, the previous analyses seem rather problematic because the tensile stresses and strains increase for elevated confinement. This, however, contradicts the documented test results since a clear reduction in apparent strength was found for reduced surface friction. It must be stated that other (non elastic) factors impact the failure behavior and the ultimate strength of concrete.

5.4 Local Buckling Effects (Instability)

The high-speed video recordings revealed different crack propagation for dissimilar end conditions. Moreover, after cracking developed individual concrete shards, the footage disclosed localized buckling phenomena for both conventional and reduced surface friction (see Figures 4.14(d), 4.16(d), and 4.19(d), for example). Although, according to Figure 5.2, the principal compression intensifies for increased shear stresses at the contact surface, it must be noted that the crack orientation changes as well (e.g., Figure 5.4). The changed inclination of cracks causes different failure patterns (compare Figures 4.10 and 4.11) and different types of concrete shards. Figure 5.11 conceptualizes

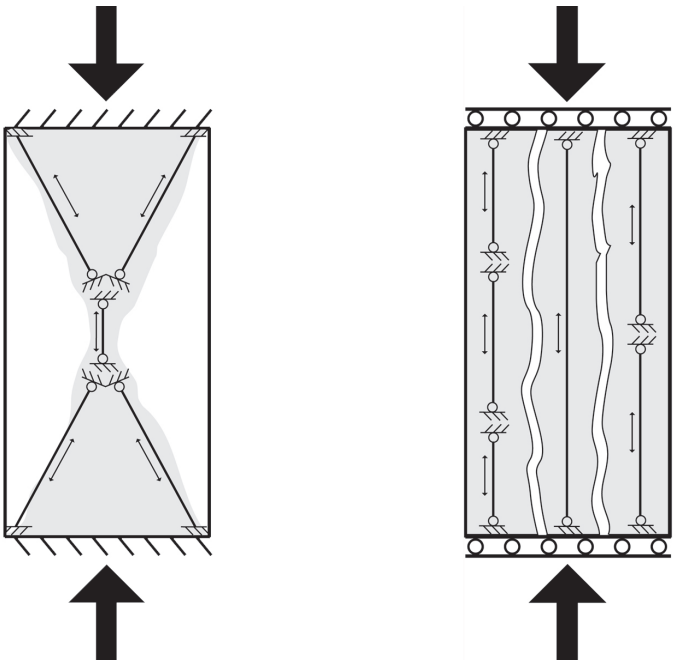

(a) Conventional friction (b) Reduced friction

Figure 5.11: Idealized buckling concept (local instability)

the observed buckling phenomena for idealized boundary conditions. Generally, the fragments under conventional friction are inclined from both specimen ends as illustrated in Figure 5.11(a), while the shards under reduced friction are usually formed vertically according to Figure 5.11(b). In consequence, the test group samples cracked into elements that were (possibly) as long as the sample itself, while the control group specimens cracked into shorter pieces, approximately half the specimen height. In addition, the ends of the concrete shards were differently restrained, with more confinement for the control group specimens. Those characteristics are significant factors for local buckling phenomena and need to be considered for the effective length in Euler columns. In other words, the critical load for the concrete shards in the control group is higher due to shorter buckling length and increased end confinement.

CHAPTER 6

DISCUSSION

6.1 Introduction

This study evaluates the influence of surface friction at the compression interface on four typical concrete sample shapes, and distinctive behavioral variations in strength, crack initiation, crack propagation, and failure pattern have been shown. This chapter reviews the previous findings in an effort to relate the preceding analysis to the experimental test results. The different failure characteristics are discussed separately, before the last section attempts to merge all failure aspects to embrace a general failure theory for concrete in compression on the material and structural levels.

6.2 Strength

The test results proved surface friction to have an important impact on the strength performance of typical concrete samples. The specific characteristics of the interacting contact surfaces play a prominent role in terms of the quantitative reduction of apparent compressive strength. A within-group com-

parison via Student's t-tests confirmed the influence of surface friction on the ultimate strength measurements regardless of the specimen shape. It was shown that a decrease in surface confinement lowers the apparent uniaxial "ultimate" strength of concrete specimens. The measured reduction between the two assessed surface treatments was found to range between 9.5 % and 31 % with small cylinders on the low end and columns on the high end, respectively. With an averaged strength reduction of 22 %, the measured test results are considered to be in good agreement with the literature (Hughes and Bahramian, 1965) for tests on prismatic specimens which measured strength differences between 8 % and 40 %.

The shape effect was confirmed by ANOVA to be significant within a 95 % confidence interval for all test series except between series 1 (tall cylinder) and series 4 (cube). In general, this is in good agreement with other studies (Chin et al., 1997; Gonnerman, 1925; Hughes and Bahramian, 1965; Malhotra, 1976), apart from the insignificant strength difference between tall cylinders and cubes. However, analogous observations have been reported as well (Day and Haque, 1993; Gyengo, 1938). Although researchers have suggested that dimensional effects vanish with reduced surface friction (Hughes and Bahramian, 1965; Tschegg et al., 1994), based on the available data in this study and the corresponding statistical analyses, it is concluded that such effects exist regardless of the two evaluated friction media.

Though both effects (shape and surface) have been confirmed and exist independent of each other, their interaction-analysis showed that series 2 (small cylinder) reacts reliably differently to surface friction than all other specimen types in this research. It is assumed that this is attributable to the difference in contact area as well as to the specimen height, which in a reciprocal-series

comparison shows the highest divergence for series 2. It can be stated that the shape effect is not a phenomenon that is caused by surface friction alone — as expected previously (Hughes and Bahramian, 1965; Tschegg et al., 1994). Under such assumption, all test group specimens would provide similar strength results without statistically significant differences. Because that is not the case, it is concluded that the geometry of the specimen plays an important role (Bazant and Pfeiffer, 1987; Caner and Bazant, 2002; Neville, 1966; Shah and Ouyang, 1994).

6.3 Strain

The compressive and tensile strains were measured at mid-height for series 1 specimens under conventional and reduced surface friction. To evaluate the strain behavior before and at failure, the uniaxial compressive stress was steadily increased to 90 % of the average failure stress (as measured for each friction scenario) and sustained thereafter.

In the control group, two out of five specimens failed prematurely, before the 90 % average failure stress could be sustained. "Stress levels are very sensitive to internal structural differences and hence subject to significant statistical variation" (Loo, 1992). Considering a 5.0 % coefficient of variation for conventional compressive strength in series 1, the sustained stress approached failure closely, rendering the experiments vulnerable to outliers at the lower strength spectrum[1].

The measured MOE showed equivalent stiffness for all specimens, indepen-

[1]Other sustained stress levels were evaluated, but without reputable outcome. Similar to Smadi et al. (1985), a 95 % stress level could only be sustained for a few seconds, whereas 85 % of the average failure load may have not sufficed to produce final collapse after 3 days.

dent of end confinement. Because ACI 318 8.5.1 (American Concrete Institute, 2011a) predicts the MOE based on the ultimate compressive strength, the calculated stiffness differed between the two groups, with stiffer values for specimens tested under conventional friction. It appears that such effect was not measurable because the longitudinal strain gauges covered merely 20 % of the specimen height/length and were located in a region with uniform deformation characteristics, regardless of end confinement. This verifies Figure 5.11 and the so-called central zone which is "generally accepted to be subjected to a near-uniform uniaxial compressive stress in contrast to the complex and indefinable compressive state of stress imposed on the end zones by frictional restraints due to the interaction between specimen and loading device" (Kotsovos, 1983). Consequently, the MOE — measured on 6 in. × 12 in. (152 mm × 305 mm) concrete cylinders — according to ASTM-International (2002c) is unaffected by the compression interface.

Linearity was maintained until a compressive strain of 800 µϵ was reached for both surface conditions alike, and "there is little doubt that this deviation from proportionality marks the onset of cracking" (Kaplan, 1963). It is assumed that this is "primarily due to bond breakdown at the aggregate mortar matrix interface after which the material exhibits distinct inelastic properties but still behaves in a relatively stable manner" (Kotsovos and Newman, 1977). Within the stable cracking limits, fracture — at the ITZ — only propagates if the stress further increases. However, the stable phase is followed by unstable cracking (throughout further load increments) that generally occurs around 75 % of the short-term ultimate compressive strength (Newman and Newman, 1971; Rüsch, 1960; Smadi et al., 1985) and is due to fracture within the mortar matrix and bridging between existing bond cracks (Mey-

ers et al., 1969). The onset of unstable cracking is referred to as "critical load/stress" (Sturman et al., 1965) because the long-term strength of concrete falls below this critical value (Meyers et al., 1969). If the compressive stress is sustained within the unstable cracking range, any concrete specimen eventually collapses. The longitudinal compressive strains in Figure 4.4 showed that the onset of unstable cracking for conventionally tested specimens occurred around 1300 $\mu\epsilon$, corresponding to 5000 psi (34.4 MPa) or approximately 75 % of the ultimate strength. Due to the average strength difference between the control and test groups, the specimens under reduced friction did not reach the unstable cracking phase within the ascending portion of the stress-strain curve. No rapid strain rate change was displayed in Figure 4.6, and the sustained stress level appeared to be right at the transition point between stable and unstable cracking. Consequently, the stable and unstable cracking phases within the central zone of the specimen seem unaffected by the compression interface — at least up to 75 % of the conventional compressive strength or 90 % of the test group strength — because the ascending portion of the two compressive stress-strain graphs (Figures 4.4 and 4.6) are congruent. Kotsovos (1983) reported similar findings, and it appears reasonable that the first two deformation stages are not significantly affected by specimen end confinement, because elastic deformations and stable cracking are intrinsic material mechanisms that are microstructure dependent.

The transverse tensile strains, as a result of Poisson's effects, were graphed in Figures 4.5 and 4.7, for conventional end confinement and reduced surface friction at the compression interface, respectively. Analogous to the compressive strains, all three deformation stages — elastic , stable cracking, and unstable cracking — were reflected by the tensile strain data for conventional

compression tests (Figure 4.5), and the test results for specimens with reduced end confinement (Figure 4.7) only reflected the first two deformation stages throughout the ascending portion of the stress-strain curve. For both test scenarios, elasticity (pre-cracking) was maintained for tensile strains below 150 $\mu\epsilon$, and stable cracks formed between 150 $\mu\epsilon$ and 300 $\mu\epsilon$.

After the formation of stable cracks, the conventionally tested specimens experienced a drastic tensile strain rate increase, and the stress-strain curve plateaued around 1000 $\mu\epsilon$. However, the specimens tested under reduced surface friction reached their sustained stress level around 300 $\mu\epsilon$, and no rapid strain rate change occurred — though it appears certain that unstable cracks formed under sustained stress. Conventionally tested specimens finally collapsed at strain measurements between 3000 $\mu\epsilon$ and 4000 $\mu\epsilon$, whereas the strain gauges for the test group samples measured values up to 6000 $\mu\epsilon$. Such data must be interpreted with care, and it is emphasized that tensile strain measurements with surface mounted gauges can be problematic for brittle materials because single cracks are averaged over the entire gauge length. In fact, "direct observation is desirable since the strains at which cracks are formed and the exact nature of the cracks may be determined" (Sturman et al., 1965), especially since the material in the direct vicinity of a crack is strain-relieved while the actual crack opening may widen. Certainly, this is acceptable for the elastic phase and tolerable throughout stable cracking, but "the onset of localized cracking cannot be uniquely defined since its assessment depends on the method of detection used" (Kotsovos and Newman, 1977). As a result, strain measurements within the unstable cracking stage are rather indicative of local crack widening or global (entire specimen) dilation. Nevertheless, the extreme tensile strain measurements suggest higher ductility for the test group

specimens or a more sudden/explosive collapse for specimens tested with conventional compression plates.

6.4 Cracking

The amount of confinement controls the final fracture pattern. High surface friction results in Type 1 or Type 2 rupture according to ASTM C 39 (ASTM-International, 2004b) because higher confinement restrains the concrete from cracking through the contact surfaces. Reduced friction at the bearing plates causes failure cracks parallel to the applied compression, running through the complete length of the specimens as a result of unimpeded lateral tensile strains — a behavior that was verified by the stress/strain analyses and is substantiated by the referenced literature (Atan and Slate, 1973; Buyukozturk et al., 1971; Kupfer et al., 1969; Lee et al., 2004; Mills and Zimmerman, 1970; Rosenthal and Glucklich, 1970; Tasuji et al., 1978). Although most studies focused on concrete in biaxial or triaxial testing states, it appears that the control samples under reduced friction — tested in uniaxial compression for normalization of biaxial or triaxial test results — failed in similar patterns as the test group specimens evaluated in this research, with vertical cracks. Some studies (Atan and Slate, 1973; Kupfer et al., 1969; Tasuji et al., 1978) report inclined cracks (up to 30°), but the hypothesis is still valid, as those failure patterns are the consequence of increased shear stresses/strain due to the filaments of the brush platens (Hampel, 2006; Tschegg et al., 1994; van Mier, 1984) used in those studies.

Surface friction has a significant impact on cracking behavior and crack propagation during compression testing. Moreover, the location of crack ini-

tiation appears affected because the conventionally-tested specimens cracked from the center of the sample toward the top or bottom, while the specimens tested with reduced surface friction started to crack from the top or the bottom and propagated vertically through the entire length of the sample. It is concluded that natural failure behavior of concrete in compression is only truly reflected if surface friction at the compression interface is reduced/eliminated.

6.5 Failure Planes

The concrete dust that was found on the failure facets of regularly tested specimens proved to be a post-failure phenomenon by the high-speed video analysis. After major cracks were formed, the concrete pieces spalled off and abraded the residual concrete structure to develop dusty failure surfaces. Such behavior was not observed for the concrete samples tested with reduced end confinement as their failure planes were clean, shiny, and absent of dust.

The crush-dust is considered a post-failure phenomenon that only occurs for specimens with restrained ends. The clean failure facets — that initially exist for both test conditions — are indicative of the actual failure mechanism of concrete under compression; this validates the hypothesized tensile failure criterion.

6.6 Local Buckling Effects (Instability)

Although the collapse of concrete specimens is initiated by cracking due to tensile strains, other factors contribute to the complex failure mechanism of concrete (Bazant, 1984; Bazant and Pfeiffer, 1987; Bazant and Yuyin, 1997;

Burtscher and Koilegger, 2003; van Mier and Man, 2009) as confirmed by the high-speed video analysis. Especially Figures 4.16(d/e) and 4.19(d/e) verify that the unstable cracking stage (Newman and Newman, 1971; Saitoa, 1987) is followed by a localized buckling mechanism as predicted in a previous study (Bazant and Yuyin, 1997). The resulting failure is highly dependent on the initial crack formation as it determines the width and height of the concrete shards. The more slender the elements that are formed throughout the cracking phase, the lower the critical buckling load and the lower the apparent ultimate strength of the concrete specimen (Bazant and Yuyin, 1997; Burtscher and Koilegger, 2003). Other researchers (Blanks and McNamara, 1935; Turkel and Ozkul, 2010) reported lower strength measurements for taller samples. Therefore, it can be assumed that, in general, the critical buckling strength decreases as the specimen size increases. Furthermore, buckling appears to be the main reason for the strength reduction due to lower confinement. Cracks have to form a 30° to 45° angle with the vertical direction (del Viso et al., 2008; Hughes and Bahramian, 1965) under conventional confinement conditions, forming stocky elements with higher end confinement and increased buckling resistance. If whereas cracks are formed vertically, as it is the case under reduced friction (Bazant and Yuyin, 1997; Buyukozturk et al., 1971; Föppl, 1899; Mills and Zimmerman, 1970; Roddenberry et al., 2011; Rosenthal and Glucklich, 1970), slender concrete fragments are generated, which allow easy activation of localized buckling, causing a premature failure.

6.7 Summary of Failure Mechanisms

Based on the documented test results, the conducted analysis, and the previous discussion, the failure mechanism can be defined. To initiate failure, cracking must occur, regardless of the specific specimen type or end confinement level. The offset of fracture as well as the crack propagation are highly dependent on the characteristics of the compression interface. Based on the different boundary conditions, the stress distribution throughout the test sample varies, but the major failure cracks appear to follow the principal compressive stress trajectories. In other words, cracks seem to develop perpendicularly to the principal tensile stresses as it would be expected, in general. However, the stress analysis in comparison to the observed test results revealed that such statement is misleading and cannot be made for the entire failure regime, as the tensile stress criterion shows a singularity for true uniaxial compression. After extending the failure analysis into the strain domain, the discrepancy vanished due to Poisson's ratio effects — validating a limiting tensile strain criterion that defines the formation of failure cracks. Nevertheless, the ultimate strength behavior of concrete is not exclusively determined by cracking. In fact, after major cracks are developed, the structural arrangement of the concrete specimen changes but still resists additional loading. The maximum load at collapse depends on the effective length of the formed columnar elements that finally fail through localized buckling mechanisms along the principal compression trajectories. Surface friction hinders the cracks from propagating freely and, therefore, increases the compressive strength of the concrete specimens.

The apparent strength of concrete is affected by (1) the evaluated geomet-

rics of the specimen and (2) the characteristics of the contact surfaces during compression testing. The former can be found in the referenced literature and is mostly referred to as the size or shape effect of concrete in compression (del Viso et al., 2008; Gonnerman, 1925; Lessard et al., 1993; Pistilli and Willems, 1993; van Mier and Man, 2009). Many researchers have studied this phenomenon and agree, that for cylinders with a length-to-diameter ratio of 2, smaller cylinders sustain higher loads (del Viso et al., 2008; Gonnerman, 1925; Lessard et al., 1993). It has been postulated that such effects are eliminated through the reduction of end confinement (Hughes and Bahramian, 1965; Tschegg et al., 1994). However, those hypotheses cannot be supported by this research. Instead, it is assumed that such phenomena originate from the post-cracking failure behavior of concrete — localized buckling. A maximum tensile strain capacity followed by buckling phenomena may explain the shape and size effect of concrete in compression.

6.7.1 Concrete Failure in Structural Elements

The ultimate strength of structural elements is mostly based on empirical equations for specific members or components; i.e., beam, girder, slab, wall, etc. The fracture behavior of those components usually depends on the design details (reinforcement volume, reinforcement location, prestressing volume, prestressing location, debonding pattern, etc.) of the non-homogeneous reinforced concrete structure — as the configuration of the entire structure determines the failure path throughout the different load stages. However, if structural failure is driven by sudden concrete collapse, as opposed to bonding release or system failure, then crack initiation, crack propagation, and final

failure are found to be in good agreement with the proposed failure mechanism on the material level. Figure 6.1 displays a Florida I-Beam (FIB) that was tested at the FDOT Structures Research Center as part of FDOT contract BDK75 977-05. This particular specimen was tested under high shear stresses

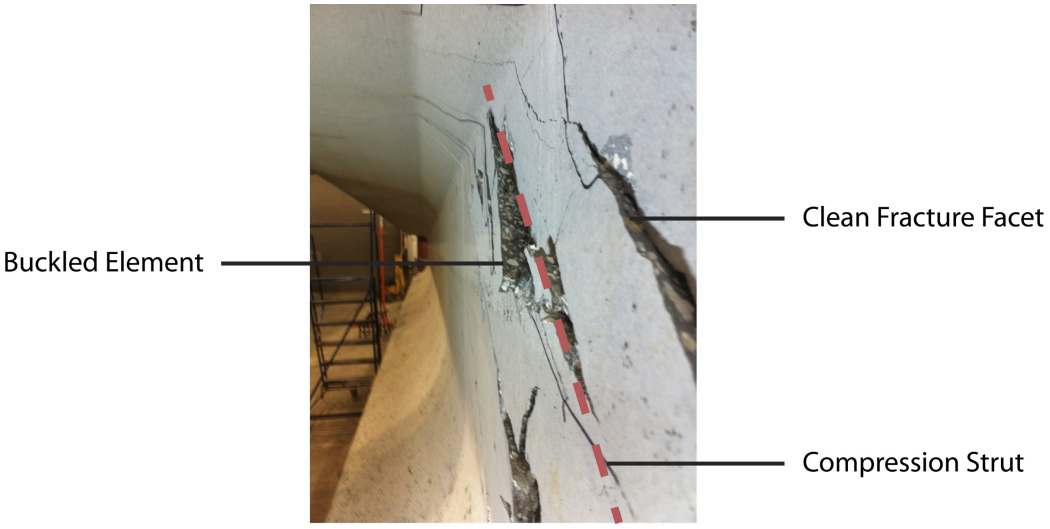

Figure 6.1: Compression strut failure due to local buckling (FDOT contract BDK75 977-05)

to study end region detailing; the specific arrangement of confinement reinforcement and other factors (see Hamilton and Ross (2012) for more details) forced this FIB to collapse along the compression strut. The fracture facets along the web were caused by principal tensile strains, and their surfaces appeared clean, shiny, and free of dust. Furthermore, the diagonal web cracks produced slender compression struts that evidently failed due to buckling. The global failure of the entire beam element was preceded by local buckling along the compression struts as seen in Figure 6.2. The picture, therefore, verifies that the concrete did not crush but buckled locally, and it can be stated that

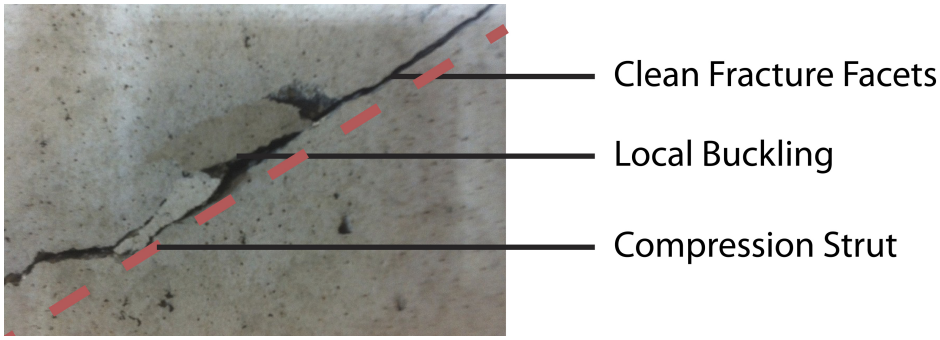

Figure 6.2: Local buckling along compression strut in structural element (FDOT contract BDK75 977-05)

structural failures, due to concrete collapse, obey the proposed (material level) failure mechanism. Cracks are formed along the principal compression trajectories, or more precisely, perpendicular to the principal tensile strains. While the compression strut changes its structural arrangement, it resists additional compression until localized buckling causes disintegration of the material along the load path, causing the structure to collapse.

It can be concluded that the regular compressive strength test according to ASTM C 39 (ASTM-International, 2004b) with conventional surface friction is not able to simulate structural failure as precisely as the evaluated test group specimens with reduced surface friction at the compression interface.

CHAPTER 7

CONCLUDING REMARKS

7.1 Conclusions

Four typical concrete specimen types were tested in uniaxial compression under two different boundary conditions. Performance (i.e., ultimate strength, fracture initiation, crack propagation, and failure mechanism) variations were measured and analyzed. Based on the presented evaluation and discussion, the following conclusions can be drawn:

- The difference in Poisson's ratio between the concrete specimen and the regular compression platens in a conventional uniaxial compression test produces end confinement.

- The measured modulus of elasticity according to ASTM-International (2002c) is not affected by the compression interface for the evaluated 6 in. × 12 in. (152 mm × 305 mm) standard cylinders.

- The conventional concrete compression test according to ASTM C 39 (ASTM-International, 2004b) cannot be considered a "true" materials test because the failure mechanism and the ultimate strength depend on

the boundary conditions of the test arrangement.

- Reduced surface friction at the compression interfaces causes lower "ultimate" strength measurements, regardless of sample shapes.

- Depending on the specimen shape, the amount of strength reduction due to reduced end confinement differs.

- A statistically significant difference in strength performance (shape effect) exists between all tested sample shapes, except between tall cylinders and cubes.

- Concrete cracks are due to tensile strains and cannot be explained by tensile stresses. Fracture results from indirect lateral tension (Buyukozturk et al., 1971; Tasuji et al., 1978; Taylor, 1971), or rather from principal tensile strains.

- Concrete is brittle, and the Poisson's effect is sufficient to develop rupture tensile strains. In a nearly "true" uniaxial compression test, lateral dilation causes the concrete sample to crack in line with the applied compressive force.

- The so-called "compression failure" of concrete appears to be a misnomer. Although the test arrangement produces compression and ultimate failure, unstable cracks — due to principal tensile strains — initiate the fracture mechanism.

- The onset of stable and unstable cracking within the central zone of standard 6 in. × 12 in. (152 mm × 305 mm) cylinders appears identical for

both evaluated surface treatments, although the ultimate strengths differ significantly.

- The intensity of surface friction at the compression interfaces impacts the unstable cracking phase and determines its release location (crack initiation).
- Final collapse appears more ductile for specimens tested with reduced end confinement.
- Ultimate collapse of concrete specimens, regardless of end confinement and specimen shape, is due to buckling of concrete fragments that are formed throughout the unstable cracking phase.
- The failure mechanism of concrete specimens seems more consonant with the failure behavior of structural concrete members, if surface friction at the compression interface is eliminated.

7.2 Future Research

Although this text concludes the presented research project, certain aspects can be further evaluated to gain further insight on the outlined failure characteristics. The following topics are proposed to enhance the knowledge and understanding of concrete failure:

- To further analyze the shape effect of concrete specimens, different sample types with different aspect ratios should be studied.
- The influence of the compression contact surface on the failure behavior of concrete can be evaluated through sample types with constant

length/height under varying width or diameters.

- Concrete specimens with constant cross-sectional dimensions and variable length/height offer further insight on the buckling mechanism and its effect on "ultimate" strength behavior.

- The spectrum of end confinement can be extended to include the influence of more diverse boundary conditions. The evaluation of different friction reduction/eliminating media might lead to an improvement of conventional compression plates.

- The buckling behavior of concrete on the material level should be analyzed for more complex stress and strain states.

BIBLIOGRAPHY

American Association of State Highway and Transportation Officials (2001). *Standard Method for Making and Curing Concrete Test Specimens in the Laboratory*, (T126). Washington, D.C.

American Association of State Highway and Transportation Officials (2006). *Standard Method of Test for Compressive Strength of Cylindrical Concrete Specimens*, (T22). Washington, D.C.

American Concrete Institute (2011a). *Building Code Requirements for Structural Concrete (ACI 318-11) and Commentary - An ACI Standard*, (ACI 318). Farmington Hills, MI 48331.

American Concrete Institute (2011b). *Guide to Evaluation of Strength Test Results of Concrete*, (ACI 214R-11). Farmington Hills, MI.

ASTM-International (1998). *Standard Practice for Capping Cylindrical Concrete Specimens*, (C 617). West Conshohocken, PA.

ASTM-International (2002a). *Standard Practice for Making and Curing Concrete Test Specimens in the Laboratory*, (C 192/C 192 M). West Conshohocken, PA.

ASTM-International (2002b). *Standard Specification for Portland Cement*, (C 150). West Conshohocken, PA.

ASTM-International (2002c). *Standard Test Method for Static Modulus of Elasticity and Poisson's Ratio of Concrete in Compression*, (C 469). West Conshohocken, PA.

ASTM-International (2003a). *Standard Specification for Concrete Aggregates*, (C 33). West Conshohocken, PA.

ASTM-International (2003b). *Standard Test Method for Slump of Hydraulic-Cement Concrete*, (C 143/C 143 M). West Conshohocken, PA.

ASTM-International (2004a). *Standard Specification for Chemical Admixtures for Concrete*, (C 494/C 494 M). West Conshohocken, PA.

ASTM-International (2004b). *Standard Test Method for Compressive Strength of Cylindrical Concrete Specimens*, (C 39/C 39 M). West Conshohocken, PA.

ASTM-International (2010). *Standard Specification for Air-Entraining Admixtures for Concrete*, (C260 / C260M). West Conshohocken, PA.

Atan, Y. and Slate, F. O. (1973). "Structural lightweight concrete under biaxial compression." *ACI Journal Proceedings*, *70*(3), 182–185.

Bazant, Z. P. (1984). "Size effect in blunt fracture: Concrete, rock, metal." *Journal of Engineering Mechanics*, *110*(4), 518–535.

Bazant, Z. P. (2000). "Size effect." *International Journal of Solids and Structures*, *37*(1-2), 69–80.

Bazant, Z. P. and Pfeiffer, P. A. (1987). "Fracture energy of concrete: Its definition and determination from size effect test." *ACI Journal Proceedings*, *100*, 89–110.

Bazant, Z. P. and Yuyin, X. (1997). "Size effect in compression fracture: Splitting crack band propagation." *Journal of Engineering Mechanics*, *123*(2), 162–172.

Bhushan, B. and Gupta, B. (1991). *Handbook of Tribology: Materials, Coatings, and Surface Treatments*, (1st Edition). McGraw-Hill, New York.

Blanks, R. F. and McNamara, C. C. (1935). "Mass concrete tests in large cylinders." *ACI Journal Proceedings*, *31*(1), 280–303.

Bresler, B. and Pister, K. S. (1958). "Strength of concrete under combined stresses." *ACI Journal Proceedings*, *55*(9), 321–244.

Burg, R. G., Caldarone, M. A., Detwiler, G., Jansen, D. C., and Willems, T. J. (1999). "Compression testing of HSC: Latest technology." *Concrete International*, *21*(8), 67–76.

Burtscher, S. L. and Koilegger, J. (2003). "Size-effect experiments on concrete in compression." *Structural Concrete*, *4*(4), 163–174.

Buyukozturk, O., Nilson, A. H., and Slate, F. O. (1971). "Stress-strain response and fracture of a concrete model in biaxial loading." *ACI Journal Proceedings*, *68*(8), 590–598.

Caldarone, M. A. and Burg, R. G. (2009). "Importance of end surface preparation when testing high strength concrete cylinders." *HPC Bridge Views*, *57*, 9–11.

Caner, F. C. and Bazant, Z. P. (2002). "Lateral confinement needed to suppress softening of concrete in compression." *Journal of Engineering Mechanics*, *128*(12), 1304–1313.

Carino, N. J., Guthrie, W. F., Lagergreen, E. S., and Mullings, G. M. (1994). "Effects of testing variables on the strength of high-strength (90 Mpa) concrete cylinders, proceedings of the international conference on high performance concrete." *ACI Symposium Publications*, *149*, 589–632.

Chin, M. S., Mansur, M. A., and Wee, T. H. (1997). "Effects of shape, size, and casting direction of specimens on stress-strain curves of high-strength concrete." *ACI Materials Journal*, *94*(3), 209–219.

da Silva, V. D. (2006). *Mechanics And Strength of Materials*, (1^{st} Edition). Springer, Berlin.

Day, R. L. and Haque, M. N. (1993). "Correlation between strength of small and standard concrete cylinders." *ACI Materials Journal*, *90*(5), 452–462.

del Viso, J., Carmona, J., and Ruiz, G. (2008). "Shape and size effects on the compressive strength of high-strength concrete." *Cement and Concrete Research*, *38*(8), 386–394.

Föppl, A. (1899). "Die Abhängigkeit der Bruchgefahr von der Art des Spannungszustandes (The fracture risk depending on the stress state)." *Mitteilungen aus dem Mechanisch Technischen Laboratorium der Technischen Hochschule München*, *27*, 1–30.

Gonnerman, H. F. (1925). "Effect of size and shape of test specimen on

compressive strength of concrete." *Proceedings of the American Society of Testing Materials*, *25*(2), 1–18.

Gyengo, T. (1938). "Effect of type of test specimen and gradation of aggregate on compressive strength of concrete." *ACI Journal Proceedings*, *34*(1), 269–284.

Hake, P. J. (2004). *"Comparison of compressive strengths using 4x8 vs. 6x12 cylinders for prestress concrete."* Technical Report RDT 04-005, Missouri Department of Transportation.

Hamilton, III, H. R., Llanos, G., and Ross, B. E. (2009). *"Shear performance of existing prestressed concrete bridge girders."* Technical Report BD 545-56, Florida Department of Transportation.

Hamilton, III, H. R. and Ross, B. E. (2012). *"End region detailing of pretensioned concrete bridge girders."* Technical Report BDK75 977-05, Florida Department of Transportation.

Hampel, T. (2006). *"Experimentelle Analyse des Tragverhaltens von Hochleistungsbeton unter mehraxialer Beanspruchung (Experimental analysis of the behaviour of high performance concrete under multiaxial states of stress)."* Dissertation, Technische Universität Dresden, Dresden.

Hosford, W. F. (2010). *Solid Mechanics*, (1^{st} Edition). Cambridge University Press, Cambridge, UK.

Hughes, B. P. and Bahramian, B. (1965). "Cube tests and the uniaxial compressive strength of concrete." *Magazine of Concrete Research*, *17*(53), 177–181.

Hussein, A. and Marzouk, H. (2000). "Behavior of high-strength concrete under biaxial stresses." *ACI Materials Journal*, *97*(1), 27–35.

Indelicato, F. and Paggi, M. (2008). "Specimen shape and the problem of contact in the assessment of concrete compressive strength." *Materials and Structures*, *41*(2), 431–441.

Kaplan, M. F. (1963). "Strains and stresses of concrete at initiation of cracking and near failure." *Journal of the American Concrete Institute*, *60*(7), 853–880.

Kotsovos, M. D. (1983). "Effect of testing techniques on the post-ultimate behavior of concrete in compression." *Materials and Structures*, *16*(1), 3–11.

Kotsovos, M. D. and Newman, J. B. (1977). "Behavior of concrete under multiaxial stress." *ACI Journal Proceedings*, *74*(9), 443–446.

Kupfer, H., Hilsdorf, H. K., and Rusch, H. (1969). "Behavior of concrete under biaxial stresses." *ACI Journal Proceedings*, *66*(8), 656–665.

Lee, S.-K., Song, Y.-C., and Han, S.-H. (2004). "Biaxial behavior of plain concrete of nuclear containment building." *Nuclear Engineering and Design*, *227*(2), 143–152.

Lessard, M., Challal, O., and Aticin, P.-C. (1993). "Testing high-strength concrete compressive strength." *ACI Materials Journal*, *90*(4), 303–307.

Loo, Y. H. (1992). "A new method for microcrack evaluation in concrete under compression." *Materials and Structures*, *25*(10), 573–577.

Malhotra, V. M. (1976). "Are 4 x 8 inch concrete cylinders as good as 6 x 12 inch cylinders for quality control of concrete?." *ACI Journal Proceedings*, *73*(1), 33–36.

McHenry, D. and Karni, J. (1958). "Strength of concrete under combined tensile and compressive stress." *ACI Journal Proceedings*, *54*(4), 829–838.

Mehta, P. K. and Monteiro, P. J. M. (2005). *Concrete: Microstructure, Properties, and Materials*, (3^{rd} Edition). McGraw-Hill Professional, New York.

Meyers, B. L., Slate, F. O., and Winter, G. (1969). "Relationship between time-dependent deformationand microcracking of plain concrete." *ACI Journal Proceedings*, *66*(1), 60–67.

Mills, L. L. and Zimmerman, R. M. (1970). "Compressive strength of plain concrete under multiaxial loading conditions." *ACI Journal Proceedings*, *67*(10), 802–806.

Neville, A. M. (1956). "The influence of size of concrete test cubes on mean strength and standard deviation," magazine of concrete research." *Magazine of Concrete Research*, *8*(23), 101–110.

Neville, A. M. (1966). "A general relation for strengths of concrete specimens of different shapes and sizes." *ACI Journal Proceedings*, *63*(10), 1095–1110.

Neville, A. M. (1996). *Properties of Concrete*, (4^{th} Edition). John Wiley & Sons, Inc., New York.

Newman, K. and Newman, J. B. (1971). "Failure theories and design criteria for plain concrete." *International Civil Engineering Material Conference on*

Structures, Solid Mechanics and Engineering Design. Wiley Interscience, 963–995.

Pistilli, M. F. and Willems, T. (1993). "Evaluation of cylinder size and capping method in compression strength testing of concrete." *Journal of Cement, Concrete and Aggregates (CCA)*, *15*(1), 59–69.

Popovics, S. (1998). *Strength and Related Properties of Concrete: A Quantitative Approach*, (1^{st} Edition). John Wiley & Sons, Inc., New York.

Prestressed Concrete Institute (2004). *PCI Design Handbook*. U.S.A.

Richart, F. E., Brandtzæg, A., and Brown, R. L. (1928). *"A study of the failure of concrete under combined compressive stresses*." Technical Report 12, University of Illinois at Urbana Champaign.

Roddenberry, M., Kampmann, R., Ansley, M. H., Bouchard, N., and Ping, W. V. (2011). "Failure behavior of concrete cylinders under different end conditions." *ACI Materials Journal*, *108*(1), 79–87.

Rosenthal, I. and Glucklich, J. (1970). "Strength of plain concrete under biaxial stress." *ACI Journal Proceedings*, *67*(11), 903–914.

Ross, B. E. and Hamilton, III, H. R. (2011). "Evaluation of strain gage lengths for testing limestone and granite aggregate concretes." *Construction and Building Materials*, *25*(1), 406–408.

Rüsch, H. (1960). "Researches toward a general flexural theory for structural concrete." *ACI Journal Proceedings*, *57*(7), 1–28.

Sadd, M. H. (2004). *Elasticity: Theory, Applications, and Numerics*, (1^{st} Edition). Elsevier Butterworth-Heinemann, Oxford, UK.

Saitoa, M. (1987). "Characteristics of microcracking in concrete under static and repeated tensile loading." *Cement and Concrete Research*, *17*(2), 211–218.

Shah, S. P. and Ouyang, C. (1994). "Fracture mechanics for failure of concrete." *Annual Review of Materials Science*, *24*, 293–219.

Smadi, M. M., Slate, F. O., and Nilson, A. H. (1985). "High-, medium-, and low-strength concretes subject to sustained overloads-strains, strengths, and failure mechanisms." *ACI Journal Proceedings*, *82*(5), 657–664.

Sturman, G. M., Shah, S. P., and Winter, G. (1965). "Microcracking and inelastic behavior of concrete." *ACI Symposium Publications*, *12*, 473–499.

Taghaddos, H., Soleymani, H. R., and Robson, J. D. D. (2010). "Precision of compressive strength testing of concrete with different cylinder specimen sizes." *ACI Materials Journal*, *107*(5), 461–468.

Tasuji, M. E., Slate, F. O., and Nilson, A. H. (1978). "Stress-strain response and fracture of concrete in biaxial loading." *ACI Journal Proceedings*, *75*(7), 306–311.

Tawfiq, K. and Robinson, B. (2008). *"Post-tensioned bridge girder anchorage zone enhancement with fiber reinforced concrete (FRC)."* Technical Report BDB14, The Florida Department of Transportation.

Taylor, M. A. (1971). "General behavior theory for cement pastes, mortars, and concretes." *ACI Journal Proceedings*, *68*(10), 756–761.

Torrenti, J.-M., Pijaudier-Cabot, G., and Reynouard, J.-M. (2010). *Mechanical Behavior of Concrete*, (1^{st} Edition). John Wiley & Sons, Inc., London.

Tschegg, E., Elser, M., and Stanzl-Tschegg, S. (1994). "Biaxial fracture tests on concrete - development and experience." *Cement and Concrete Composites*, *17*(1), 67–85.

Tucker, J. (1945). "Effect of dimensions of specimen upon the precision of strength data." *ASTM Proceedings*, *45*, 952–959.

Turkel, A. and Ozkul, M. H. (2010). "Size and wall effects on compressive strength of concrete." *ACI Materials Journal*, *107*(4), 372–379.

van Mier, J. G. M. (1984). *"Strain-softening of concrete under multiaxial loading conditions."* Dissertation, Technische Hogeschool Eindhoven, Eindhoven.

van Mier, J. G. M. and Man, H.-K. (2009). "Some notes on microcracking, softening, localization, and size effects." *International Journal of Damage Mechanics*, *18*(3), 283–311.

Xiao, J., Li, W., Sun, Z., and Shah, S. P. (2012). "Crack propagation in recycled aggregate concrete under uniaxial compressive loading." *ACI Materials Journal*, *109*(4), 451–462.

Yazici, Ş. and Sezera, G. İ. (2007). "The effect of cylindrical specimen size on the compressive strength of concrete." *Building and Environment*, *42*(6), 2417–2420.

Appendices

APPENDIX A

MATLAB SCRIPTS

A.1 Stress Analysis

```
%%%%%%%%%%%%%%%%%%%%%%%%%%%%%%%%%%%%%%%%%%%%%%%%%%%%%%%%%%%%%%%%%%%%%%%%
%%% 2012/02/01 Raphael Kampmann
%%%%%%%%%%%%%%%%%%%%%%%%%%%%%%%%%%%%%%%%%%%%%%%%%%%%%%%%%%%%%%%%%%%%%%%%
% This MatLab Script calculates the principal stress magnitude
% as a function of the shear stress and plots them
% accordingly. Additionally, it determines and plots the
% directional angles (alpha, beta, and gamma) for the principal
% compressive and tensile stresses.
%
% If required, the figures can be exported to Adobe IL files.
%%%%%%%%%%%%%%%%%%%%%%%%%%%%%%%%%%%%%%%%%%%%%%%%%%%%%%%%%%%%%%%%%%%%%%%%

% clear the workspace
close all, clear all, clc
%%%%%%%%%%%%%%%%%%%%%%%%%%%%%%%%%%%%%%%%%%%%%%%%%%%%%%%%%%%%%%%%%%%%%%%%
%% Imput variables
%%%%%%%%%%%%%%%%%%%%%%%%%%%%%%%%%%%%%%%%%%%%%%%%%%%%%%%%%%%%%%%%%%%%%%%%

% normal stresses (negative for compression, positive tension)
sigma_xx = -1; % normal stress along x-axis
sigma_yy = 0; % normal stress along y-axis
sigma_zz = 0; % normal stress along z-axis
```

```
% shear stresses
tau_xy = -1; % shear stress on x-surface in y direction
tau_xz = tau_xy; % shear stress on x-surface in z direction

% codeing help
resolution= 1000;
%FigureDimension = get(0, 'DefaultFigurePosition');
%set(0,'DefaultFigurePosition',...
                                [FigureDimension(1:2), 800, 600]);

%%%%%%%%%%%%%%%%%%%%%%%%%%%%%%%%%%%%%%%%%%%%%%%%%%%%%%%%%%%%%%%%%%%%%%%%%%%
%% writing the stress tensor
%%%%%%%%%%%%%%%%%%%%%%%%%%%%%%%%%%%%%%%%%%%%%%%%%%%%%%%%%%%%%%%%%%%%%%%%%%%

% Generate a three dimensional array for the stress tensor
% 3rd order tensor with different shear stresses for each layer
nrows=3; % every layer contains 3 rows
ncols=3; % every layer contains 3 columns
layers = resolution;
% Preallocate a stress matrix
sigma_ij = ones(nrows, ncols,layers);
for k=1:layers;
% Loop through the matrix
    for i = 1:nrows
       for j = 1:ncols
          if i == 1 && j == 1
             sigma_ij(i,j,k) = sigma_xx;
          elseif i == 2 && j == 2
             sigma_ij(i,j,k) = sigma_yy;
          elseif i == 3 && j == 3
             sigma_ij(i,j,k) = sigma_zz;
          elseif i == 1 && j == 2
             sigma_ij(i,j,k) = (k-1)*tau_xy/layers;
          elseif i == 1 && j == 3
             sigma_ij(i,j,k) = (k-1)*tau_xz/layers;
          elseif i == 2 && j == 1
             sigma_ij(i,j,k) = (k-1)*tau_xy/layers;
          elseif i == 3 && j == 1
             sigma_ij(i,j,k) = (k-1)*tau_xz/layers;
          else
             sigma_ij(i,j,k) = 0;
          end
```

```
       end
    end
 end

% sigma_ij

for i = 1:layers;
    tau_xy(i)=-(i-1)*tau_xz/layers; % negative normalizes graphs
end

%%%%%%%%%%%%%%%%%%%%%%%%%%%%%%%%%%%%%%%%%%%%%%%%%%%%%%%%%%%%%%%%%%%%%%%
%% principal strain magnitudes (lambda) and angles
%%%%%%%%%%%%%%%%%%%%%%%%%%%%%%%%%%%%%%%%%%%%%%%%%%%%%%%%%%%%%%%%%%%%%%%

for i=1:layers;
    [Principal_Directions,Principal_Stress]=...
                                              eig(sigma_ij(:,:,i));
    gamma=i/layers;

    % principal strain magnitudes (lambda)
    L_1(i) = Principal_Stress(1,1);
    L_2(i) = Principal_Stress(2,2);
    L_3(i) = Principal_Stress(3,3);

    % compressive strain angles
    alpha_c(i) =acosd(abs(Principal_Directions(1,1))/1);
    beta_c(i)  =acosd(abs(Principal_Directions(2,1))/1);
    gamma_c(i) =acosd(abs(Principal_Directions(3,1))/1);

    % tensile strain angles
    alpha_t(i) =acosd(abs(Principal_Directions(1,3))/1);
    beta_t(i)  =acosd(abs(Principal_Directions(2,3))/1);
    gamma_t(i) =acosd(abs(Principal_Directions(3,3))/1);

    % remaining strain angles
    alpha_r(i) =acosd(abs(Principal_Directions(1,2))/1);
    beta_r(i)  =acosd(abs(Principal_Directions(2,2))/1);
    gamma_r(i) =acosd(abs(Principal_Directions(3,2))/1);

    % Tensor Invariances
    I_1(i) = trace(sigma_ij(:,:,i));
    I_2(i) = sigma_ij(1,1,i)*sigma_ij(2,2,i)+...
```

```
            sigma_ij(1,1,i)*sigma_ij(3,3,i)+...
            sigma_ij(2,2,i)*sigma_ij(3,3,i);
    I_3(i) = det(sigma_ij(:,:,i));

    % Octahedral Stresses
    sigma_oct(i) = I_1(i)/3;
    tau_oct(i)   = sqrt(2)/3 * sqrt((I_1(i))^2-3*I_2(i));

end

%%%%%%%%%%%%%%%%%%%%%%%%%%%%%%%%%%%%%%%%%%%%%%%%%%%%%%%%%%%%%%%%%%%%%%%
%% plot principal stress magnitudes (lambda)
%%%%%%%%%%%%%%%%%%%%%%%%%%%%%%%%%%%%%%%%%%%%%%%%%%%%%%%%%%%%%%%%%%%%%%%
figure_1 = figure('Position',[600,10,800,600]);
%subplot(2,2,1)
plot(tau_xy,L_1,'k','DisplayName', 'lambda_{1}'); % c stress
hold on;
%plot(tau_xy,L_2,'g','DisplayName', 'lambda_{2}'); % r stress
plot(tau_xy,L_3,'r','MarkerSize',3,...
                'DisplayName', 'lambda_{3}'); % t stress
title('Shear Stress vs. Principal Stress Value',...
      'FontSize',16,'FontWeight', 'bold');
xlabel('Shear Strain','FontSize',14);
ylabel('Principal Stress Value [lambda]','FontSize',14);
grid on;
legend('show','Location','SouthEast');

% uncomment to save figure as Adobe IL file
%saveas(figure_1,'ShearStressVsPrincipalStressValue', 'ai');

%%%%%%%%%%%%%%%%%%%%%%%%%%%%%%%%%%%%%%%%%%%%%%%%%%%%%%%%%%%%%%%%%%%%%%%
%% plot principal direction angles for principal tensile stress
%%%%%%%%%%%%%%%%%%%%%%%%%%%%%%%%%%%%%%%%%%%%%%%%%%%%%%%%%%%%%%%%%%%%%%%
%subplot(2,2,2)
figure_2 = figure('Position',[600,10,800,600]);
plot(tau_xy(end,2:end),alpha_t(end,2:end),...
     'b','DisplayName', 'alpha');
hold on;
plot(tau_xy(end,2:end),beta_t(end,2:end),...
     'r','DisplayName', 'beta');
plot(tau_xy(end,2:end),gamma_t(end,2:end),...
     'g','MarkerSize',3,...
```

```
    'DisplayName', 'gamma');
title('Principal Tensile Stress Direction','FontSize',16,...
      'FontWeight', 'bold');
xlabel('Shear Stress','FontSize',14);
ylabel('Directional Angle []','FontSize',14);
grid on;
ylim([0 90]);
legend('show','Location','SouthEast');
% prove=(cosd(alpha))^2+(cosd(beta))^2+(cosd(gama))^2

% uncomment to save figure as Adobe IL file
%saveas(figure_2,...
%         'ShearStressVsPrincipalTensileStressDirection', 'ai');

%%%%%%%%%%%%%%%%%%%%%%%%%%%%%%%%%%%%%%%%%%%%%%%%%%%%%%%%%%%%%%%%%%%%%%%
%% plot principal direction angles for compressive stresses
%%%%%%%%%%%%%%%%%%%%%%%%%%%%%%%%%%%%%%%%%%%%%%%%%%%%%%%%%%%%%%%%%%%%%%%
%subplot(2,2,3)
figure_3 = figure('Position',[600,10,800,600]);

plot(tau_xy,alpha_c,'b','DisplayName', 'alpha');
hold on
plot(tau_xy,beta_c,'r','DisplayName', 'beta');
plot(tau_xy,gamma_c, 'g','MarkerSize',3,'DisplayName', 'gamma');
title('Principal Compressive Stress Direction',...
      'FontSize',16,'FontWeight', 'bold');
xlabel('Shear Stress','FontSize',14);
ylabel('Directional Angle []','FontSize',14);
grid on;
legend('show','Location','SouthEast');
% prove=(cosd(alpha))^2+(cosd(beta))^2+(cosd(gama))^2

% uncomment to save figure as Adobe IL file
saveas(figure_3,...
     'ShearStressVsPrincipalCompressiveStressDirection', 'ai');

%%%%%%%%%%%%%%%%%%%%%%%%%%%%%%%%%%%%%%%%%%%%%%%%%%%%%%%%%%%%%%%%%%%%%%%
%% plot principal direction angles for remaining stresses
%%%%%%%%%%%%%%%%%%%%%%%%%%%%%%%%%%%%%%%%%%%%%%%%%%%%%%%%%%%%%%%%%%%%%%%
figure_4 = figure;
plot(tau_xy(end,2:end),alpha_r(end,2:end),...
     'b','DisplayName', 'alpha');
```

```
hold on
plot(tau_xy(end,2:end),beta_r(end,2:end),...
     'ro','DisplayName', 'beta')
plot(tau_xy(end,2:end),gamma_r(end,2:end),...
     'g','MarkerSize',3,'DisplayName', 'gamma')
title('Principal Remaining Stress Direction',...
      'FontSize',16, 'FontWeight', 'bold');
xlabel('Shear Stress','FontSize',12)
ylabel('Directional Angle []','FontSize',12)
grid on
% note that beta = gamma
legend('show','Location','SouthEast');
% prove=(cosd(alpha))^2+(cosd(beta))^2+(cosd(gama))^2
hold off;
% %saveas(figure_4,'PrincipalRemainingStressDirection', 'ai');

%%%%%%%%%%%%%%%%%%%%%%%%%%%%%%%%%%%%%%%%%%%%%%%%%%%%%%%%%%%%%%%%%%%%%%%%%%%
%%%%%%%%%%%%%%%%%%%%%%%%%%%%%%%%%%%%%%%%%%%%%%%%%%%%%%%%%%%%%%%%%%%%%%%%%%%
%%%%%%%%%%%%%%%%%%%%%%%%%%%%%%%%%%%%%%%%%%%%%%%%%%%%%%%%%%%%%%%%%%%%%%%%%%%

%%%%%%%%%%%%%%%%%%%%%%%%%%%%%%%%%%%%%%%%%%%%%%%%%%%%%%%%%%%%%%%%%%%%%%%%%%%
%% octahedral stresses
%%%%%%%%%%%%%%%%%%%%%%%%%%%%%%%%%%%%%%%%%%%%%%%%%%%%%%%%%%%%%%%%%%%%%%%%%%%
%subplot(2,2,4)
figure_5 = figure;
plot(tau_xy,sigma_oct,'b','DisplayName', 'sigma_oct')
hold on
plot(tau_xy,tau_oct,'ro','DisplayName', 'tau_oct')
title('Octahedral stresses vs. shear stresses','FontSize',16,...
      'FontWeight', 'bold');
xlabel('Shear Stress','FontSize',12)
ylabel('Octahedral Stress ','FontSize',12)
ylim([-0.5 1]);
grid on
legend('show','Location','SouthEast')
% prove=(cosd(alpha))^2+(cosd(beta))^2+(cosd(gama))^2
hold off
%saveas(figure_5,'OctahedralStresses', 'ai')
%%%%%%%%%%%%%%%%%%%%%%%%%%%%%%%%%%%%%%%%%%%%%%%%%%%%%%%%%%%%%%%%%%%%%%%%%%%
%% End Program
%%%%%%%%%%%%%%%%%%%%%%%%%%%%%%%%%%%%%%%%%%%%%%%%%%%%%%%%%%%%%%%%%%%%%%%%%%%
```

A.2 Strain Analysis

```
%%%%%%%%%%%%%%%%%%%%%%%%%%%%%%%%%%%%%%%%%%%%%%%%%%%%%%%%%%%%%%%%%%%%%%%%%%%%
%%% 2012/02/01 Raphael Kampmann
%%%%%%%%%%%%%%%%%%%%%%%%%%%%%%%%%%%%%%%%%%%%%%%%%%%%%%%%%%%%%%%%%%%%%%%%%%%%
% This MatLab Script calculates the principal strain magnitude
% as a function of the shear strain and plots them  accordingly.
% Additionally, it determines and plots the directional
% angles (alpha, beta, and gamma) for the principal
% compressive and tensile strains.
%
% If required, the figures can be exported to Adobe IL files.
%%%%%%%%%%%%%%%%%%%%%%%%%%%%%%%%%%%%%%%%%%%%%%%%%%%%%%%%%%%%%%%%%%%%%%%%%%%%

% clear the workspace
close all, clear all, clc
%%%%%%%%%%%%%%%%%%%%%%%%%%%%%%%%%%%%%%%%%%%%%%%%%%%%%%%%%%%%%%%%%%%%%%%%%%%%
%% Imput variables
%%%%%%%%%%%%%%%%%%%%%%%%%%%%%%%%%%%%%%%%%%%%%%%%%%%%%%%%%%%%%%%%%%%%%%%%%%%%

% normal strains (negative for compression, positive tension)
poissons = -0.2; % material propertie (design value)
epsilon_xx= -1; % normal strain along x-axis
epsilon_yy = poissons*epsilon_xx; % normal strain along y-axis
epsilon_zz = poissons*epsilon_xx; % normal strain along z-axis

% shear strain
gamma_xy = -1; % shear strain on x-surface in y direction
gamma_xz = gamma_xy; % shear strain on x-surface in z direction

% codeing help
resolution=1000; % determines the analize mesh

%%%%%%%%%%%%%%%%%%%%%%%%%%%%%%%%%%%%%%%%%%%%%%%%%%%%%%%%%%%%%%%%%%%%%%%%%%%%
%% Start program
%%%%%%%%%%%%%%%%%%%%%%%%%%%%%%%%%%%%%%%%%%%%%%%%%%%%%%%%%%%%%%%%%%%%%%%%%%%%

%%%%%%%%%%%%%%%%%%%%%%%%%%%%%%%%%%%%%%%%%%%%%%%%%%%%%%%%%%%%%%%%%%%%%%%%%%%%
%% writing the strain tensor
%%%%%%%%%%%%%%%%%%%%%%%%%%%%%%%%%%%%%%%%%%%%%%%%%%%%%%%%%%%%%%%%%%%%%%%%%%%%
```

```
% Generate a three dimensional array for the strain tensor
% 3rd order tensor with different shear strain for each layer
nrows=3; % every layer contains 3 rows
ncols=3; % every layer contains 3 columns
layers = resolution;
% Preallocate a stress matrix
epsilon_ij = ones(nrows, ncols,layers);
for k=1:layers;
% Loop through the matrix
    for i = 1:nrows
       for j = 1:ncols
          if i == 1 && j == 1
             epsilon_ij(i,j,k) = epsilon_xx;
          elseif i == 2 && j == 2
             epsilon_ij(i,j,k) = epsilon_yy;
          elseif i == 3 && j == 3
             epsilon_ij(i,j,k) = epsilon_zz;
          elseif i == 1 && j == 2
             epsilon_ij(i,j,k) = (k-1)*gamma_xy/layers;
          elseif i == 1 && j == 3
             epsilon_ij(i,j,k) = (k-1)*gamma_xz/layers;
          elseif i == 2 && j == 1
             epsilon_ij(i,j,k) = (k-1)*gamma_xy/layers;
          elseif i == 3 && j == 1
             epsilon_ij(i,j,k) = (k-1)*gamma_xz/layers;
          else
             epsilon_ij(i,j,k) = 0;
          end
       end
    end
 end

% epsilon_ij

for i = 1:layers;
    epsilon_xy(i)=-(i-1)*gamma_xz/layers;
end

%%%%%%%%%%%%%%%%%%%%%%%%%%%%%%%%%%%%%%%%%%%%%%%%%%%%%%%%%%%%%%%%%%%%%%%%%%%
%% principal strain magnitudes (lambda) and angles
%%%%%%%%%%%%%%%%%%%%%%%%%%%%%%%%%%%%%%%%%%%%%%%%%%%%%%%%%%%%%%%%%%%%%%%%%%%
```

```
for i=1:layers % determine the iteration steps

    %calculating the eigenvalue and eigenvector
    [Principal_Directions,Principal_Strain]...
                                        = eig(epsilon_ij(:,:,i));
    gamma=i/layers; % breaking it down

    % principal strain magnitudes (lambda)
    L_1(i) = Principal_Strain(1,1);
    L_2(i) = Principal_Strain(2,2);
    L_3(i) = Principal_Strain(3,3);

    % compressive strain angles
    alpha_c(i) =acosd(abs(Principal_Directions(1,1))/1);
    beta_c(i)  =acosd(abs(Principal_Directions(2,1))/1);
    gamma_c(i) =acosd(abs(Principal_Directions(3,1))/1);

    % tensile strain angles
    alpha_t(i) =acosd(abs(Principal_Directions(1,3))/1);
    beta_t(i)  =acosd(abs(Principal_Directions(2,3))/1);
    gamma_t(i) =acosd(abs(Principal_Directions(3,3))/1);

    % remaining strain angles
    alpha_r(i) =acosd(abs(Principal_Directions(1,2))/1);
    beta_r(i)  =acosd(abs(Principal_Directions(2,2))/1);
    gamma_r(i) =acosd(abs(Principal_Directions(3,2))/1);
end

%%%%%%%%%%%%%%%%%%%%%%%%%%%%%%%%%%%%%%%%%%%%%%%%%%%%%%%%%%%%%%%%%%%%%%%
%% plot the principal strain magnitudes (lambda)
%%%%%%%%%%%%%%%%%%%%%%%%%%%%%%%%%%%%%%%%%%%%%%%%%%%%%%%%%%%%%%%%%%%%%%%
figure_1 = figure;
plot(epsilon_xy,L_1,'--k','DisplayName','lambda_{1}') % c strain
hold on
grid on
plot(epsilon_xy,L_2,'r','DisplayName', 'lambda_{2}')
plot(epsilon_xy,L_3,'g','MarkerSize',3,'DisplayName',...
                                    'lambda_{3}') % tensile stress
title('Shear Strain vs. Principal Strain Value','FontSize'...
                                       ,16, 'FontWeight', 'bold');
xlabel('Shear Strain','FontSize',12)
```

```
ylabel('Principal Strain Value [lambda]','FontSize',12)
legend('show','Location','East')
hold off

% uncomment the next line to save figure as Adobe IL file
%saveas(figure_1,'ShearStrainVsPrincipalStrainValue', 'ai')

%%%%%%%%%%%%%%%%%%%%%%%%%%%%%%%%%%%%%%%%%%%%%%%%%%%%%%%%%%%%%%%%%%%%%%%
%% plot the principal direction angles for tensile strain
%%%%%%%%%%%%%%%%%%%%%%%%%%%%%%%%%%%%%%%%%%%%%%%%%%%%%%%%%%%%%%%%%%%%%%%
figure_2 = figure;
plot(epsilon_xy(end,2:end),alpha_t(end,2:end),'--b',...
                                          'DisplayName', 'alpha')
hold on
grid on
plot(epsilon_xy(end,2:end),beta_t(end,2:end),'-k',...
                                           'DisplayName', 'beta')
plot(epsilon_xy(end,2:end),gamma_t(end,2:end), ':r',...
                          'MarkerSize',3,'DisplayName', 'gamma')
hold on
title('Principal Tensile Strain Direction','FontSize',16,...
                                           'FontWeight', 'bold');
xlabel('Shear Strain','FontSize',12)
ylabel('Directional Angle []','FontSize',12)
ylim([0 90]);
legend('show','Location','SouthEast')
hold off
%prove=(cosd(alpha))^2+(cosd(beta))^2+(cosd(gama))^2

% uncomment to save figure as Adobe IL file
%saveas(figure_2,...
%          'ShearStrainVsPrincipalTensileStrainDirection', 'ai')

%%%%%%%%%%%%%%%%%%%%%%%%%%%%%%%%%%%%%%%%%%%%%%%%%%%%%%%%%%%%%%%%%%%%%%%
%% plot the principal direction angles for compressive strain
%%%%%%%%%%%%%%%%%%%%%%%%%%%%%%%%%%%%%%%%%%%%%%%%%%%%%%%%%%%%%%%%%%%%%%%
figure_3 = figure;
plot(epsilon_xy,alpha_c,'k','DisplayName', 'alpha')
hold on
plot(epsilon_xy,beta_c,'r','DisplayName', 'beta')
plot(epsilon_xy,gamma_c, 'g','MarkerSize',3,...
                                          'DisplayName', 'gamma')
```

```
grid on
title('Principal Compressive Strain Direction','FontSize',16,...
                                              'FontWeight', 'bold');
xlabel('Shear Strain','FontSize',12)
ylabel('Directional Angle []','FontSize',12)
% note that beta = gamma
legend('show','Location','SouthEast')
hold off
% prove=(cosd(alpha))^2+(cosd(beta))^2+(cosd(gama))^2

% uncomment to save figure as Adobe IL file
%saveas(figure_3,...
%      'ShearStrainVsPrincipalCompressiveStrainDirection', 'ai')

%%%%%%%%%%%%%%%%%%%%%%%%%%%%%%%%%%%%%%%%%%%%%%%%%%%%%%%%%%%%%%%%%%%%%%%
%% plot direction angles for remaining  principal strain
%%%%%%%%%%%%%%%%%%%%%%%%%%%%%%%%%%%%%%%%%%%%%%%%%%%%%%%%%%%%%%%%%%%%%%%
figure_4 = figure;
plot(epsilon_xy,alpha_r,'b','DisplayName', 'alpha')
hold on
plot(epsilon_xy,beta_r,'r','DisplayName', 'beta')
plot(epsilon_xy,gamma_r, 'g','MarkerSize',3,...
                                          'DisplayName', 'gamma')
title('Principal Compressive Strain Direction',...
                         'FontSize',16, 'FontWeight', 'bold');
xlabel('Shear Strain','FontSize',12)
ylabel('Directional Angle []','FontSize',12)
grid on
legend('show','Location','SouthEast')
hold off
% prove=(cosd(alpha))^2+(cosd(beta))^2+(cosd(gama))^2

% uncomment to save figure as Adobe IL file
%saveas(figure_4,...
%        'ShearStrainVsPrincipalRemainingStrainDirection', 'ai')

%%%%%%%%%%%%%%%%%%%%%%%%%%%%%%%%%%%%%%%%%%%%%%%%%%%%%%%%%%%%%%%%%%%%%%%
%% End program
%%%%%%%%%%%%%%%%%%%%%%%%%%%%%%%%%%%%%%%%%%%%%%%%%%%%%%%%%%%%%%%%%%%%%%%
```

APPENDIX B

HIGH-SPEED VIDEO FOOTAGE

This appendix supplements the test results presented in Chapter 4. Specifically, the high-speed video frames outlined in Section 4.6 are taken from the videos presented on the following pages. The footage was captured according to the details and the equipment described in Section 3.10.

This appendix is particularly helpful in its electronic version because the captured motion pictures are presented and embedded inside the document. The following multimedia files can be viewed in Adobe Reader®, which is freely available at `http://get.adobe.com/reader/`. Other PDF-viewers may be compatible, but this document is guaranteed to work properly with Adobe Reader® Version 6 and above.

The footage was selected to exemplify each specimen type (tall cylinder, small cylinder, column, and cube) under both boundary conditions (conventional and reduced surface friction). Only one example video per test condition is included (and extremely compressed) to keep the file size of this document reasonable. Each video comprises up to 6,000 individual pictures that were captured at 2 kHz. The playback rates are highly reduced but all videos visualize a real-time failure behavior of less then 3 s.

B.1 Tall Cylinder Under Conventional Friction

(Load Video)

Video B.1: Series 1, control group specimen

B.2 Tall Cylinder Under Reduced Friction

(Load Video)

Video B.2: Series 1, test group specimen

B.3 Small Cylinder Under Conventional Friction

(Load Video)

Video B.3: Series 2, control group specimen

B.4 Small Cylinder Under Reduced Friction

(Load Video)

Video B.4: Series 2, test group specimen

B.5 Column Under Conventional Friction

(Load Video)

Video B.5: Series 3, control group specimen

B.6 Column Under Reduced Friction

(Load Video)

Video B.6: Series 3, test group specimen

B.7 Cube Under Conventional Friction

(Load Video)

Video B.7: Series 4, control group specimen

B.8 Cube Under Reduced Friction

(Load Video)

Video B.8: Series 4, test group specimen

INDEX